

AD-A193 895

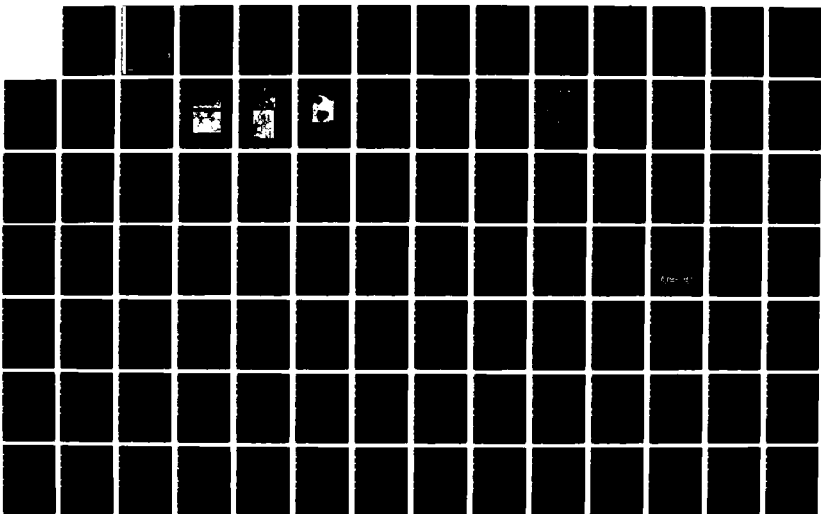
FURTHER STUDY OF THE DYNAMIC TENSILE FAILURE OF
CONCRETE(U) SRI INTERNATIONAL MENLO PARK CA
J K GRAN ET AL APR 88 AFOSR-TR-88-0642 F49628-87-K-0010

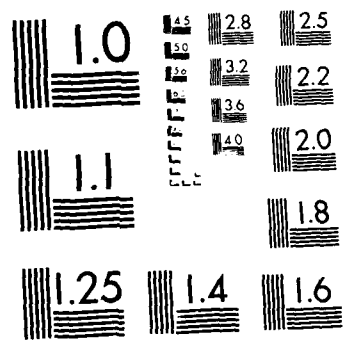
172

UNCLASSIFIED

F/G 11/2

NL





AD-A195 695

AFOSR-TR- 88 - 0642

FURTHER STUDY OF THE DYNAMIC TENSILE FAILURE OF CONCRETE

April 1988

DTIC FILE COPY

Final Report

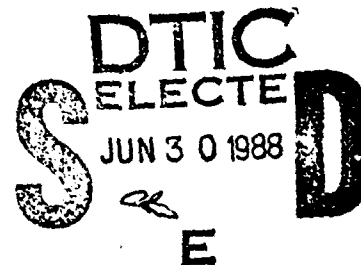
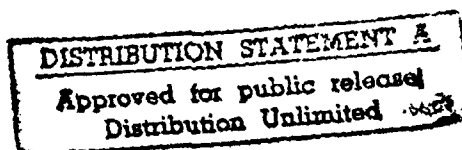
Covering the period 15 June 1987 through 14 February 1988

By: James K. Gran and Lynn Seaman

Prepared for:

AIR FORCE OFFICE OF SCIENTIFIC RESEARCH
Bolling Air Force Base
Washington, DC 20332-6448

Contract No. F49620-87-K-0010
SRI Project PYU-3717



SRI International
333 Ravenswood Avenue
Menlo Park, California 94025-3493
(415) 326-6200
TWX: 910-373-2046
Telex: 334486



88 6 29 133

UNCLASSIFIED

SECURITY CLASSIFICATION OF THIS PAGE

REPORT DOCUMENTATION PAGE

1a. REPORT SECURITY CLASSIFICATION Unclassified			1b. RESTRICTIVE MARKINGS		
2a. SECURITY CLASSIFICATION AUTHORITY			3. DISTRIBUTION/AVAILABILITY OF REPORT Approved for public release; distribution unlimited.		
2b. DECLASSIFICATION/DOWNGRADING SCHEDULE			5. MONITORING ORGANIZATION REPORT NUMBER(S) AFOSR-TR- 88-0642		
4. PERFORMING ORGANIZATION REPORT NUMBER(S) PYU-3717					
5a. NAME OF PERFORMING ORGANIZATION SRI International		5b. OFFICE SYMBOL (if applicable)		7a. NAME OF MONITORING ORGANIZATION Air Force Office of Scientific Research	
5c. ADDRESS (City, State, and ZIP Code) 333 Ravenswood Avenue Menlo Park, California 94025		7b. ADDRESS (City, State, and ZIP Code) Bolling Air Force Base Washington, DC 20332			
8a. NAME OF FUNDING/SPONSORING ORGANIZATION AFOSR/NA Bolling AFB, DC 20332		8b. OFFICE SYMBOL (if applicable) NA		9. PROCUREMENT INSTRUMENT IDENTIFICATION NUMBER F49620-87-K-0010	
8c. ADDRESS (City, State, and ZIP Code) AFOSR/NA Bolling AFB, DC 20332		10. SOURCE OF FUNDING NUMBERS			
		PROGRAM ELEMENT NO. 61102F		PROJECT NO. 2302	TASK NO. C2
		WORK UNIT ACCESSION NO.			
11. TITLE (Include Security Classification) FURTHER STUDY OF THE DYNAMIC TENSILE FAILURE OF CONCRETE					
12. PERSONAL AUTHOR(S) Gran, James K., Seaman, Lynn					
13a. TYPE OF REPORT Final		13b. TIME COVERED FROM 870615 TO 880214		14. DATE OF REPORT (Year, Month, Day) 8804	
15. PAGE COUNT 129					
16. SUPPLEMENTARY NOTATION					
17. COSATI CODES			18. SUBJECT TERMS (Continue on reverse if necessary and identify by block number)		
FIELD	GROUP	SUB-GROUP			
20	11		Concrete Experiments Material Moduli		
13	02		Cracks Fracture Microcracks Strain-Rate		
			Dynamic Geologic Microscopic Strain-Softening		
19. ABSTRACT (Continue on reverse if necessary and identify by block number) This report describes a small follow-up effort to a previous study of dynamic tensile failure of concrete in which our long-range objective is to understand and quantify the micromechanics of dynamic tensile failure of concrete. In the previous study, we developed an experimental technique to apply dynamic tension to 5-cm-diameter x 76-cm-long concrete rods at a strain rate of about 10/s, and we performed posttest computations with a simple one-dimensional strain-softening model to interpret an initial set of experiments. In the current effort, our primary task was to scrutinize the technique for observing microcracks in damaged specimens and to quantify the microcracks in some of the specimens already tested. A second task was to computationally interpret more of the experimental results. Third, we made a preliminary step toward computing the strength and modulus of a material cell containing several interacting cracks.					
20. DISTRIBUTION/AVAILABILITY OF ABSTRACT <input checked="" type="checkbox"/> UNCLASSIFIED/UNLIMITED <input type="checkbox"/> SAME AS RPT <input type="checkbox"/> DTIC USERS			21. ABSTRACT SECURITY CLASSIFICATION UNCLASSIFIED		
22a. NAME OF RESPONSIBLE INDIVIDUAL Dr. Spencer Wu			22b. TELEPHONE (Include Area Code) 202-767-6962		22c. OFFICE SYMBOL AFOSR/NA

19 ABSTRACT (Continued)

Three methods for inspecting the concrete specimens for microcracking were evaluated. The first method was to use a scanning electron microscope (SEM) to view the concrete surface. We found this method to be unsatisfactory because of extensive cracking caused by evacuating the specimen. The second method was to replicate the specimen surface with acetylcellulose replicating film and to view the film with the SEM. This method introduces uncertainties in identifying cracks. The third method was to view a polished concrete surface with an optical microscope at a magnification of 100x. This is the preferred method for observing microcrack damage produced in the dynamic tension tests. Microcracks as small as 2 μm wide and 100 μm long can be seen. Better resolution could probably be attained with more highly polished specimens. In the three 5-cm-long specimens inspected, we saw that microcracks pass through aggregates and around aggregates, some appear to be blunted by aggregates, and some terminate in the mortar. Nearly all of the damage was found within a distance of 3 cm from the primary fracture. Inspection of additional specimens that were tested in dynamic tension is recommended.

We used the simple strain-softening model to computationally interpret two additional experiments. Our approach was to match the strain histories and tensile damage. The experiments were performed on two concretes whose static tensile strengths are about 3.5 MPa. One concrete has about twice the apparent dynamic strength of the other concrete. Several more of the experiments performed previously should be interpreted with the strain-softening model to extend our knowledge of how the concrete behaved in these experiments.

A computer program was developed to evaluate Kachanov's solution for stress intensity factors, crack face displacements, and effective moduli for an elastic material containing a two-dimensional array of cracks. An improvement to account for the presence of cell boundaries is recommended.

CONTENTS

LIST OF ILLUSTRATIONS	v
SUMMARY	1
Background	1
Previous Work	1
Microscopic Inspection of Damaged Specimens	3
Strain-Softening Computations	3
Properties of a Multiply Cracked Material Cell	4
MICROSCOPIC INSPECTION OF DAMAGED SPECIMENS	7
Specimen Preparation	7
Inspection Methods	7
Results	13
Conclusions and Recommendations	15
COMPUTATIONAL INTERPRETATION OF EXPERIMENTS	19
Test 41	19
Test 103	21
Conclusions and Recommendations	26
COMPUTATION OF EFFECTIVE MODULI FOR A CRACKED MATERIAL	29
Solution for Stress Intensity Factors and Crack Openings	29
Computation of Effective Moduli	30
Conclusions and Recommendations	35

REFERENCES 39

APPENDICES A-1

A. An Experimental Method to Study the Dynamic Tensile Failure
of Brittle Geologic Materials A-1

B. Strain-Softening Calculations for Concrete in Dynamic Uniaxial
Tension B-1

C. A Subroutine for Determining Stress Intensity Values, Crack Openings,
and Effective Moduli for Multiple Cracks in an Elastic Material C-1



Accession For	
NTIS GRA&I	<input checked="checked" type="checkbox"/>
DTIC TAB	<input type="checkbox"/>
Unannounced	<input type="checkbox"/>
Justification	
By	
Distribution/	
Availability Codes	
and/or	
Dist	Special
A-1	

LIST OF ILLUSTRATIONS

1. Preparation of concrete specimen for microscopic inspection.	8
2. SEM photographs of concrete specimen showing damage caused by vacuum.	10
3. Photographs of replica film and concrete specimen showing evidence of false cracklike features in replica film.	11
4. Optical microscope photograph of polished concrete specimen 41-B1 showing a microcrack in mortar and aggregate.	12
5. Microcrack map of concrete specimen 41-B1 obtained with 100x optical microscope.	14
6. Optical microscope photographs of polished concrete specimens 103-T1 and 103-B1.	16
7. Microcrack map of concrete specimen 103-T1 obtained with 100x optical microscope.	17
8. Microcrack map of concrete specimen 103-B1 obtained with 100x optical microscope.	18
9. Strain-softening model used to numerically simulate Test 41.	20
10. Comparison of computed and observed damage in specimen 41-B1. ...	22
11. Strain-softening model used to numerically simulate Test 103.	23
12. Comparison of computed and measured axial strains in Test 103	24
13. Comparison of computed and observed damage in specimen 103-B1. ..	27
14. Comparison of computed and observed damage in specimen 103-T1. .	28

15. Variation of compliance and normalized stress intensity with crack separation for two cracks in line.	34
16. Variation of compliance and normalized stress intensity with vertical spacing between two horizontal cracks.	36
17. Variation of compliance and normalized stress intensity with crack spacing for four orthogonal cracks.	37

SUMMARY

Background

This report describes a small follow-up effort to a previous study of dynamic tensile failure of concrete [1,2]. Our long range objective is to understand and quantify the micromechanics of dynamic tensile failure of concrete. In the previous study, we developed an experimental technique to apply dynamic tension to 5-cm-diameter x 76-cm-long concrete rods at a strain rate of about 10/s [3]¹ and performed posttest computations with a simple one-dimensional strain-softening model to interpret an initial set of experiments [4]¹. The strain-softening computations and a preliminary posttest microscopic inspection of one of the specimens indicated that this experiment produces distributed tensile cracking damage that can be quantified and related to the load history. We then performed a larger set of dynamic tension experiments intended to provide a range of damage levels [2]. The results of these experiments and the damaged specimens are available for further analysis.

In the current effort, our objective was to validate the experimental and analytical approach used in the previous study. Our primary task was to scrutinize the technique for observing microcracks in damaged specimens and to quantify the microcracks in some of the specimens already tested. A second task was to use a strain-softening model to computationally interpret some of the previous experiments. Finally, we made a preliminary step toward computing the strength and modulus of a computational cell containing several interacting cracks. The results and conclusions of these tasks are summarized below.

Previous Work

An experimental method was developed to study the tensile failure of brittle geologic materials at strain rates of approximately 10 to 20/s [3]. In these experi-

¹Copies of these articles are attached as Appendices A and B.

ments, a cylindrical rod specimen is first loaded in static triaxial compression, then the axial pressure is released from each end simultaneously and very rapidly. The resulting rarefaction waves interact in the center of the rod to produce a dynamic tensile stress equal in magnitude to the original static compression. The pressure acting on the radial surface is approximately constant during the experiment. As an application of this method, several experiments were performed on concrete. Transient measurements were made of the axial load at each end, the confining pressure, and the axial and circumferential surface strains at several locations along the length of the rod.

Usually a single fracture occurred near the midpoint of the rod. In some experiments multiple fractures occurred. If we assume the peak observed strains in these experiments to be elastic, we estimate the unconfined tensile strength of the concrete at a strain rate of 10 to 20/s to be, on average, approximately 40% higher than the static splitting tensile strength. At the same strain rate, the tensile strength with 10 MPa confining pressure averaged approximately 100% higher than the static splitting tensile strength and 40% higher than the unconfined tensile strength at 10 to 20/s. Nonlinear analyses indicate that these estimates are reasonable but that, in general, the assumption of elastic response is not valid. Matching the measured strain histories with calculations requires that the rod be modeled inelastically.

A one-dimensional strain-softening model was used in wave-propagation calculations to interpret the results of the dynamic tension experiments on concrete rods [4]. The model is based on the assumption that the stress-strain relation is not a property of a material point (as in continuum theory) but an average property of a finite volume of material containing a developing crack or failure plane. The stress-strain relation thus has associated with it a finite dimension, namely the average crack separation distance. We used this model to simulate two dynamic unconfined tension experiments and, by trial-and-error, obtained good agreement with the measured axial strain histories in both cases.

In addition to providing an estimate of the dynamic tensile properties of the concrete, these calculations suggest that tensile damage in the concrete was distributed over several centimeters. Finally, the calculations suggest that the strain history measured a few centimeters from the location of fracture is primarily a function of inelastic wave propagation from the fracture location to the strain gage (through a region of distributed tensile damage) and is less dependent on the behavior of the material right at the fracture.

Microscopic Inspection of Damaged Specimens

Three methods for inspecting the concrete specimens for microcracking were evaluated. The first method was to use a scanning electron microscope (SEM) to view the concrete surface. We found this method to be unsatisfactory because of extensive cracking caused by evacuating the specimen. The second method was to replicate the specimen surface with acetylcellulose replicating film and view the film with the SEM. This method introduces uncertainties in identifying cracks. The third method was to view a polished concrete surface with an optical microscope at a magnification of 100x. This is the preferred method for observing microcrack damage produced in the dynamic tension tests. Microcracks as small as 2 μm wide and 100 μm long can be seen. Better resolution could probably be attained with more highly polished specimens.

In the three 5-cm-long specimens inspected, we saw that microcracks pass through aggregates and around aggregates, some appear to be blunted by aggregates, and some terminate in the mortar. Nearly all of the damage was found within a distance of 3 cm from the primary fracture. We recommend inspection of additional specimens that were tested in dynamic tension.

Strain-Softening Computations

The strain-softening model we use to interpret the dynamic tension experiments on concrete is based on the concept that a material cell contains a single

site of localization (fracture) and that the fundamental property of the material is the relation between stress and fracture volume per unit area (average crack opening). Within this framework, the material cell dimension represents the spatial frequency of localization sites in an inhomogeneous material. In the previous study, a 0.635-cm material cell size was found to give the best agreement with measured strains and observed fractures in the four experiments simulated.

We used the simple strain-softening model to match the strain histories and tensile damage in dynamic tension tests on two concretes whose static tensile strengths are about 3.5 MPa. The same 0.635-cm material cell size was chosen, and the relation between stress and fracture volume per unit area was adjusted to match the experimental results. The apparent dynamic strength of the concrete used in Tests 101 to 106 is about twice as high as the dynamic strength of the concrete used in Tests 41 to 46.

Several more of the experiments performed previously should be interpreted with the strain-softening model to extend our knowledge of how the concrete behaved in these experiments. We also recommend additional study of the apparent natural material cell size for a better understanding of its source and meaning.

Properties of a Multiply Cracked Material Cell

We developed a computer program to evaluate a solution derived by Kachanov [7] for determining stress intensity factors, crack face displacements, and effective moduli for elastic material containing a two-dimensional array of cracks. The actual locations of the cracks in the body, and their interactions with each other are treated. The Kachanov solution provides stress intensity factors that are within 10% of exact analytical solutions for cases with crack tip separations greater than 1% of the crack length. Hence, this analysis is useful for studying crack interactions when the cracks are fairly near each other; that is, when the cracks are approaching coalescence and fragmentation.

The limitation of the Kachanov approach is in the determination of the effective moduli for a finite cell of material, because this approach does not consider boundary conditions except those at infinity. A possible improvement to account for the presence of cell boundaries would be to lay out a repeating set of crack arrays so that the computational cell being considered is bounded by the symmetry planes between the arrays of cracks. We could then construct the compliance matrix for the central cell.

MICROSCOPIC INSPECTION OF DAMAGED SPECIMENS

Specimen Preparation

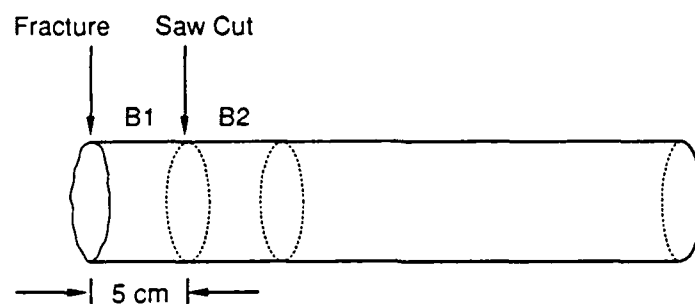
Segments from some of the specimens tested in the previous project were prepared as illustrated schematically in Figure 1. The 5-cm-long segments are cut from the rod with a diamond-impregnated saw blade. Then they are potted in a cylinder of cement paste and sectioned along a diametric plane. The face of the sectioned segment is then polished with 600-grit sandpaper.

Because most of the microcracking is expected to have occurred within a few centimeters of the primary fracture, we prepared specimens taken from this region in the rods used in Tests 41 and 103. Segments taken from the top side of the primary fracture are labeled 'T1' and 'T2' and those from the bottom side of the fracture are labeled 'B1' and 'B2', with the numbers indicating the order of the segments from the primary fracture. The top and bottom directions refer to the orientation of the rod during fabrication and testing. The coordinate system used for strain gage placement is centered at the midpoint of the rod, with the positive axis directed toward the bottom end of the rod.

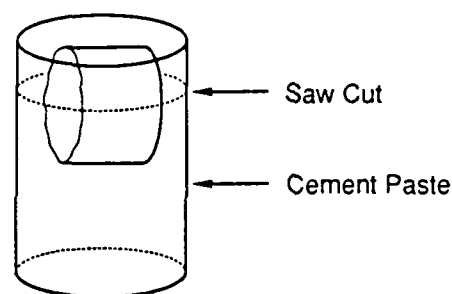
Inspection Methods

Three methods for inspecting the concrete specimens for microcracking were evaluated. The first method, using a scanning electron microscope (SEM) to view the concrete surface, was found to be unsatisfactory because of extensive cracking caused by evacuating the specimen. The second method, replicating the specimen surface with acetylcellulose replicating film and viewing the film with the SEM, introduces uncertainties in identifying cracks. The third method, viewing the concrete surface with an optical microscope, is the most straightforward and the most reliable of the three, but it is limited to a lower level of magnification than methods using the SEM.

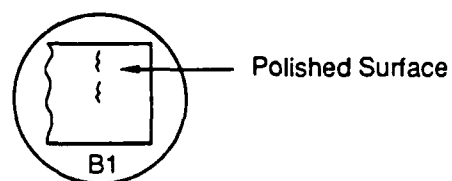
We first attempted to inspect the concrete for microcracking damage by view-



(a) Segment cut from concrete rod.



(b) Potted in cement paste and sectioned.



(c) Polished for microscopic inspection.

RA-M-3717-1

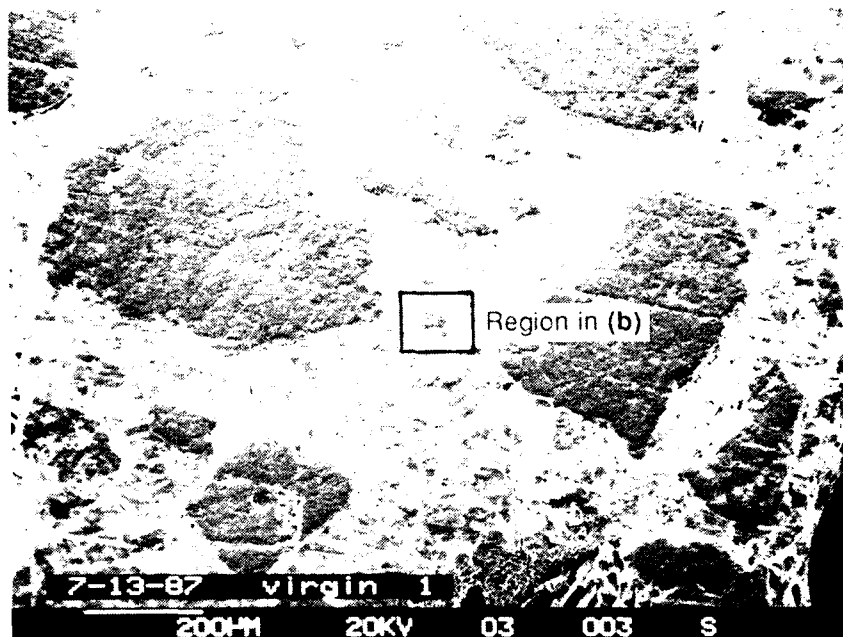
Figure 1. Preparation of concrete specimen for microscopic inspection.

ing the polished concrete surface with the SEM. Unfortunately, this method introduces extensive damage to the concrete. Figure 2 shows a pair of SEM photographs of a virgin concrete specimen. The network of microcracks results from evacuating the specimen in preparation for coating it with a conductive layer (a vacuum is also necessary for viewing with the SEM). We proved that the cracks are caused by the vacuum by inspecting replicas of a specimen before and after evacuation (not shown). Thus, even though other researchers have utilized this or a similar method for microscopic inspections of concrete [5,6], we found it unsatisfactory for our purposes.

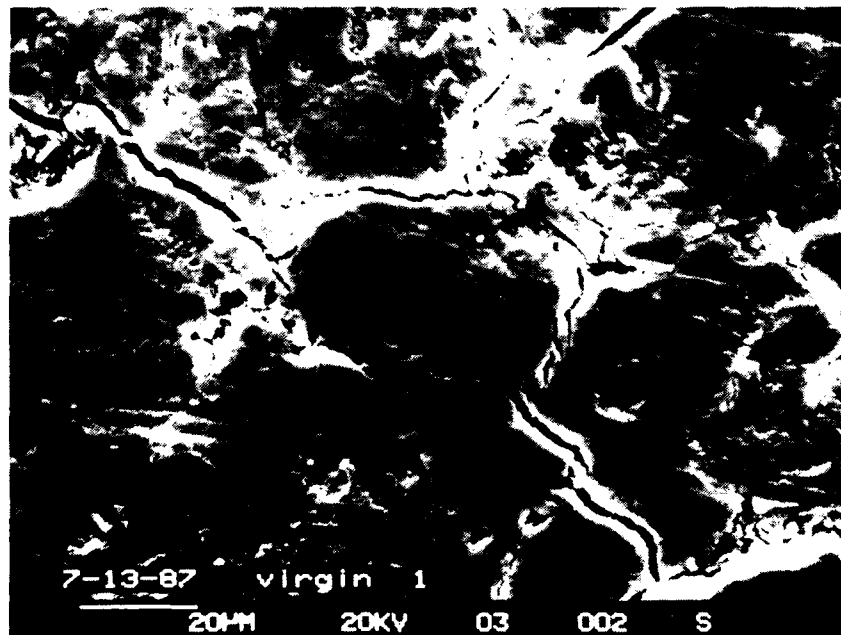
The second method was to use acetylcellulose replicating film. When applied with a solvent to the polished surface of the specimen, this film replicates the surface by flowing into the cracks and voids. The film is then dried, coated with a thin layer of gold, and viewed with an SEM. In the previous project, this method was used to chart the microcracks in one specimen and produced seemingly good results. However, upon further scrutiny in the current study, we concluded that there is significant uncertainty in identifying microcracks with the replicating film.

Figure 3 compares an SEM photograph of an acetylcellulose replica with an optical photograph of the concrete specimen. Note that because the replica is made face down, the photographs are reversed images of each other. The fine white lines on the replica were identified previously as microcracks from their cracklike appearance. The concrete specimen does not appear to have cracks at these locations. At a magnification of 500x, a roughness indicative of surface flaking can be seen with the optical microscope at the locations of the apparent cracks, but a true crack is not visible. Thus, it appears that the replica accentuates these surface features so that they resemble cracks. This can give misleading information, and we conclude that this method of inspection is too unreliable for the present purpose.

The preferred method is simply to view the concrete surface directly through an optical microscope. Figure 4 shows a photograph of a microcrack at a different



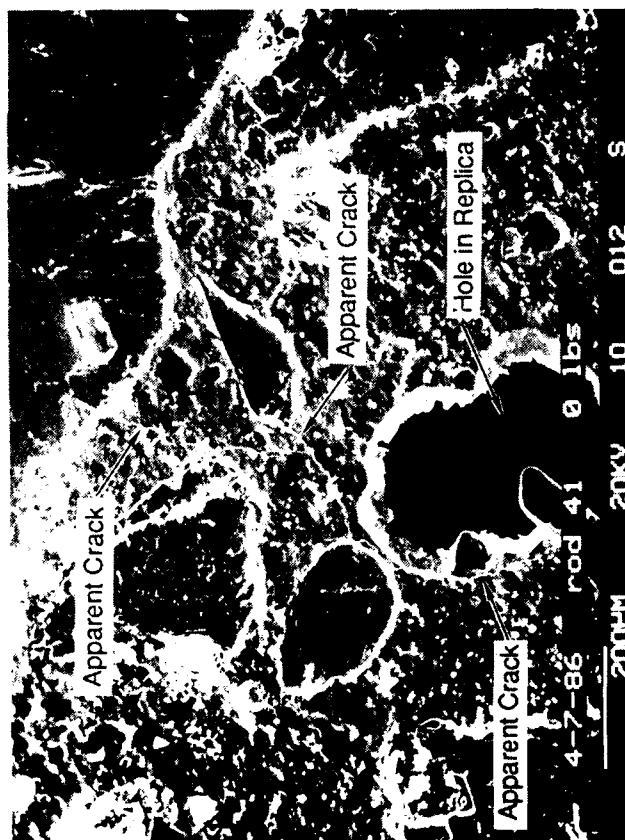
(a) Microcrack network



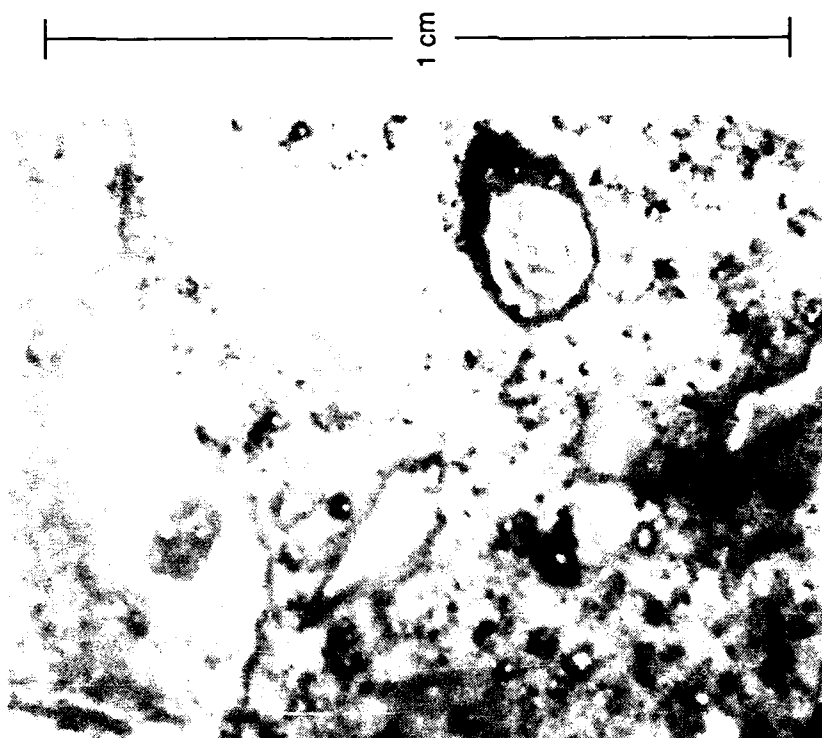
(b) Debonding of aggregate

RP-m-3717-2

Figure 2. SEM photographs of concrete specimen showing damage caused by vacuum.



(a) SEM photograph of replica



(b) Optical microscope photograph of concrete (100 x)

RP-m-3717-3

Figure 3. Photographs of replica film and concrete specimen showing evidence of false crack-like features in replica film.

Photographs are mirror images of each other.



RP-m-3717-4

Figure 4. Optical microscope photograph of polished concrete specimen 41-B1 showing a microcrack in mortar and aggregate.

location in the specimen shown in Figure 3. This crack is about 4 mm in length; only a portion of its total length is shown in the photograph. Admittedly, the optical photographs of the concrete are not as sharp as the SEM photographs of replicas, but when viewed through the microscope at 100x, the concrete surface can be seen with sufficient detail to identify without doubt cracks as small as 2 μm wide and 100 μm long. Larger cracks can be photographed clearly at 100x. When the concrete surface is viewed at a magnification of 500x the surface roughness is greater than the depth of field, but by adjusting the focus while scanning a small area the viewer can garner additional detail. This method could be improved if the surface of the specimen could be more highly polished and if the optics could provide a greater depth of field.

Results

Specimens from two rods tested in the previous study and a specimen from a virgin rod were prepared and inspected for microcracks. The previously tested rods were made of different concretes and were preloaded to different levels. A range of microcrack damage was observed in these specimens. No microcracks were found in the virgin specimen.

The first specimen inspected was 41-B1. The static splitting strength of this concrete was about 3.4 MPa. In Test 41 the static preload was a uniaxial stress of 10.8 MPa, and the rod fractured at -5.0 cm from the midpoint. This is the same rod that we inspected previously by the replica method. However, in this investigation we inspected the other half of the same segment. Figure 4 shows a photograph of this specimen, and Figure 5 shows a map of the full set of microcracks found. The map shows that there is a concentration of damage about 2.5 cm from the primary fracture. This is consistent with the predictions of strain-softening calculations, as will be shown below. The long crack running in the axial direction lies along the boundary between mortar and a long, slender aggregate.

The next rod inspected was from Test 103. The static splitting strength of

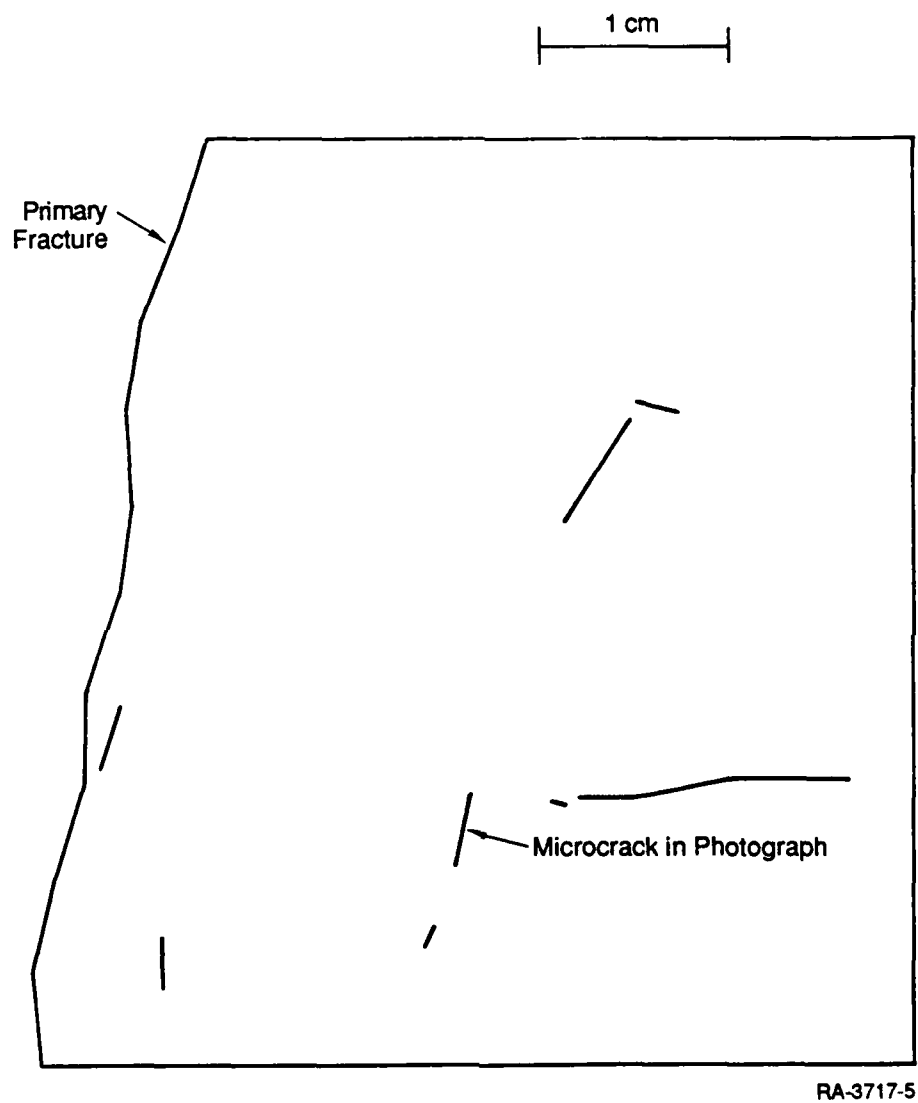


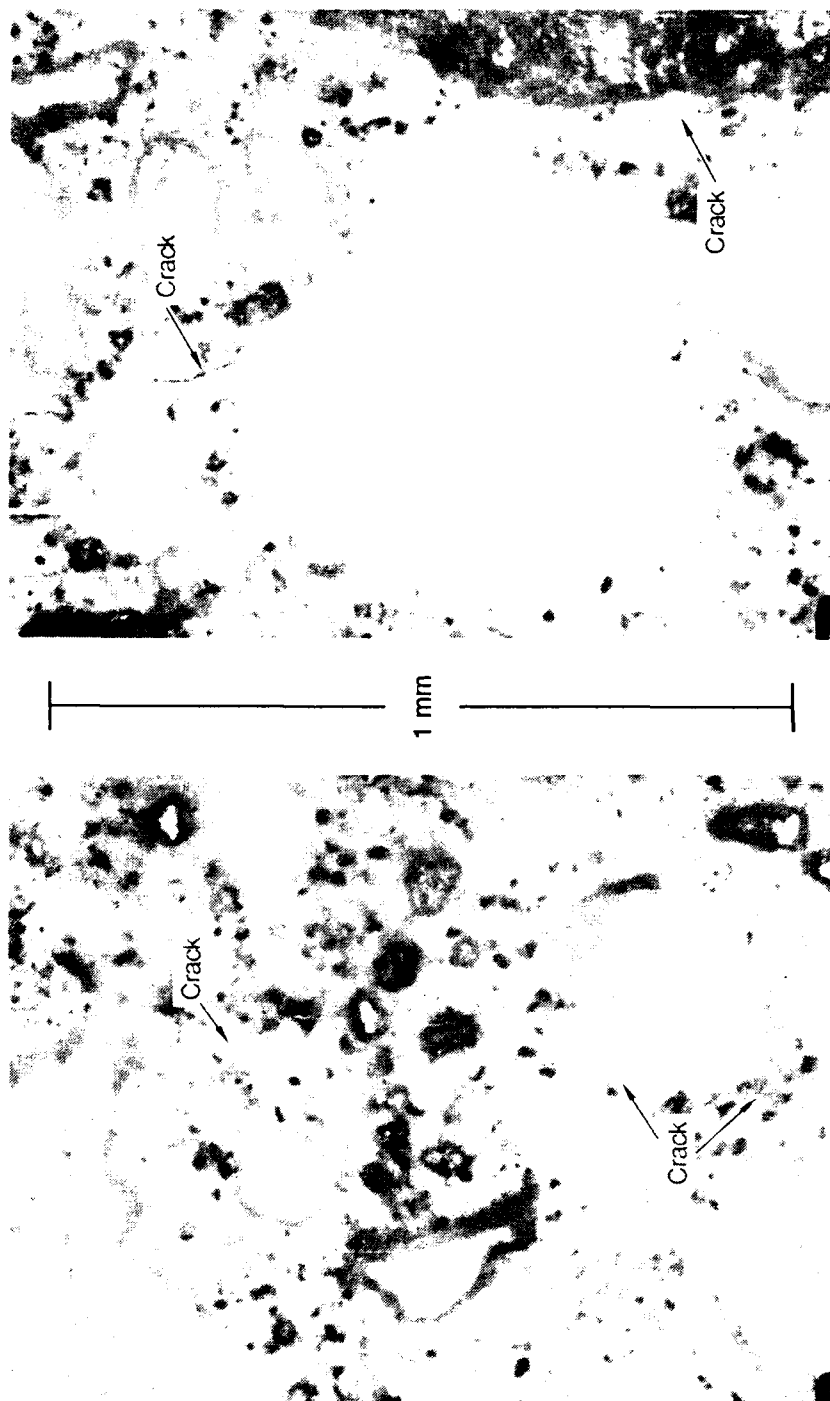
Figure 5. Microcrack map of concrete specimen 41-B1 obtained with 100x optical microscope.

this concrete was about 3.6 MPa. In Test 103 the static preload was 17.3 MPa; the primary fracture occurred at +2.9 cm from the midpoint. Figure 6 shows photographs taken of specimens 103-T1 and 103-B1, and the microcrack maps of these specimens are shown in Figures 7 and 8. In 103-T1 the damage is concentrated about 2 cm from the primary fracture; in 103-B1 there is a large crack about 3 cm from the primary fracture. Again, strain-softening calculations predicted a concentration of damage a few centimeters from the primary fracture.

Conclusions and Recommendations

Viewing a polished concrete surface with an optical microscope at a magnification of 100x is a suitable method for observing microcrack damage produced in the dynamic tension tests. Microcracks as small as 2 μm wide and 100 μm long can be seen. Better resolution could probably be obtained with more highly polished specimens.

In the three 5-cm-long specimens inspected we saw that *microcracks pass through aggregates and around aggregates; some appear to be blunted by aggregates; and some terminate in the mortar.* Nearly all of the damage was found within 3 cm of the primary fracture. We recommend inspection of additional specimens that were tested in dynamic tension so that we can relate quantified observations of damage to known loading conditions for a range of loads.

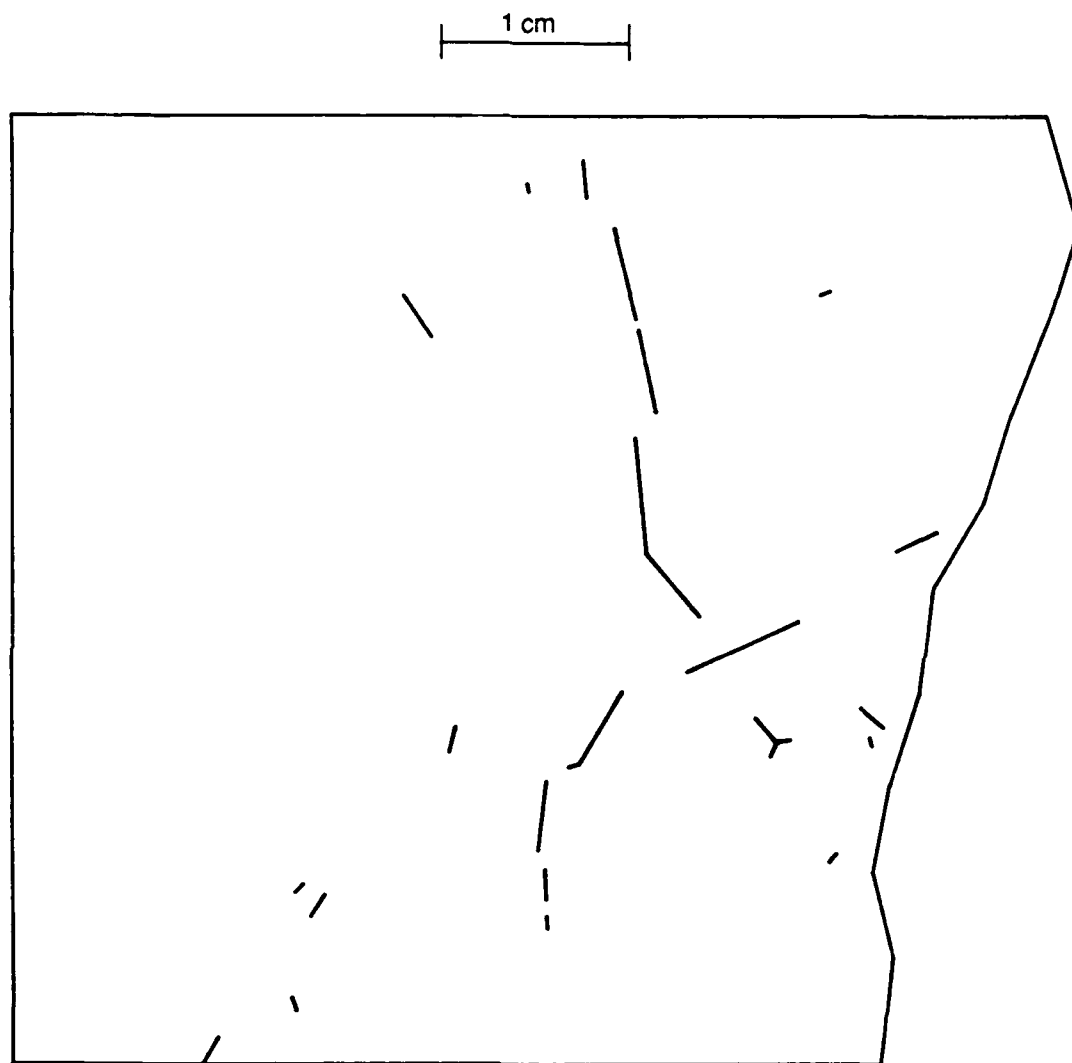


(a) 103-T1

(b) 103-B1

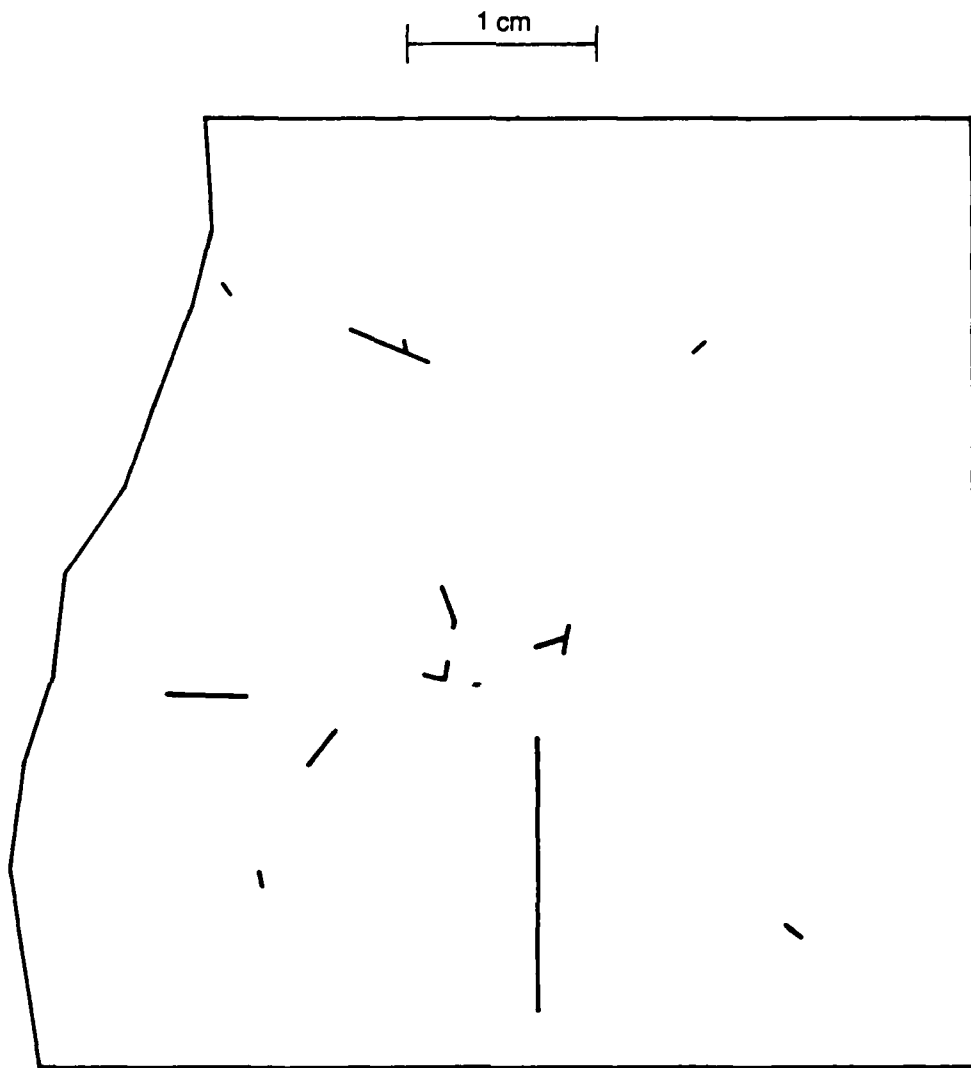
RP-m-3717-6

Figure 6. Optical microscope photographs of polished concrete specimens 103-T1 and 103-B1.



RA-3717-7

Figure 7. Microcrack map of concrete specimen 103-T1 obtained with 100x optical microscope.



RA-3717-8

Figure 8. Microcrack map of concrete specimen 103-B1 obtained with 100x optical microscope.

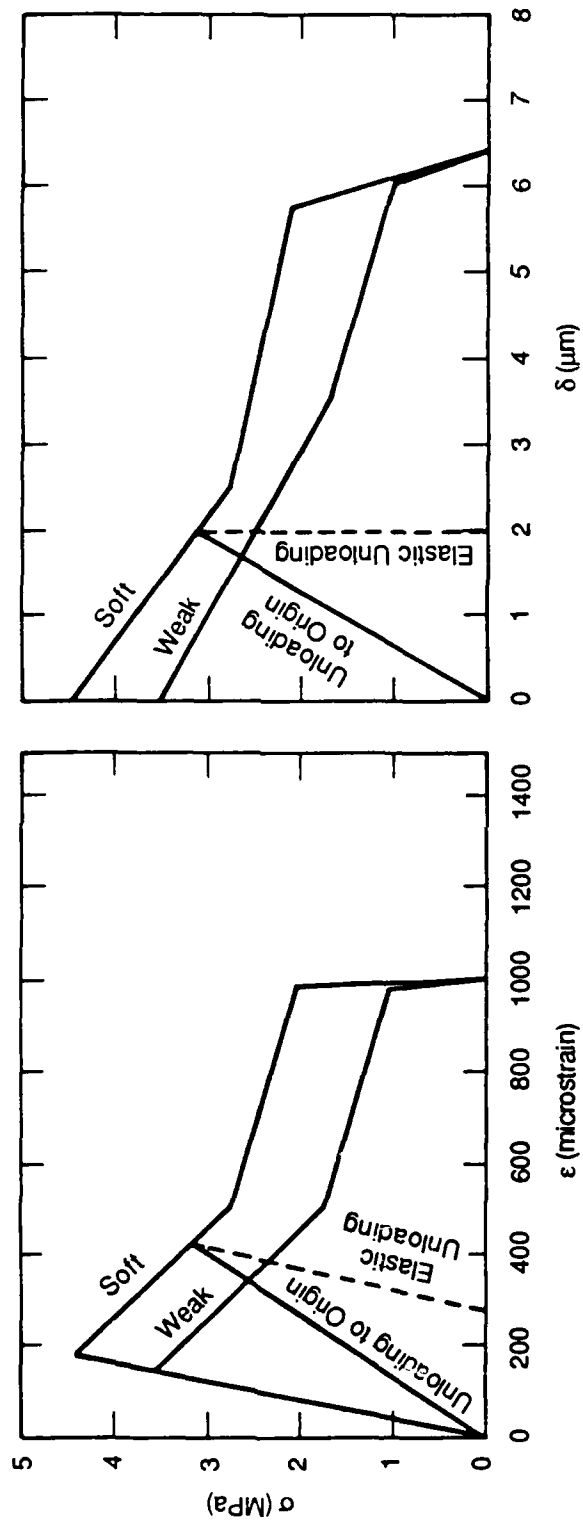
COMPUTATIONAL INTERPRETATION OF EXPERIMENTS

The purpose of the calculations performed in this effort is to interpret the results of the experiments. In addition to the initial conditions and the boundary conditions, the data available from an experiment include the location of fracture and the strain histories at a few locations on both sides of the fracture. These data do not, in themselves, provide a direct measure of a material property. Our approach to interpreting the results is to make an estimate of the material behavior, namely the stress-strain path followed in the experiment, and to computationally simulate the experiment. By adjusting the estimate of the stress-strain path, we can satisfactorily match the data from the experiment. Then the assumed stress-strain path is a reasonable estimate of the actual material response in that experiment. Four experiments were interpreted in this manner previously. Two more experiments were interpreted in the present effort.

Test 41

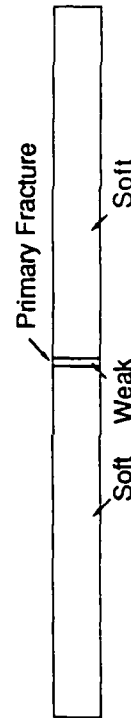
Tests 41, 42, and 43 were performed with a static uniaxial preload of about 10.5 MPa on rods made of the same concrete. In all three tests the primary fracture was within 1 cm of the midpoint of the rod. Tests 42 and 43 were instrumented with strain gages, and the results were matched previously with computations with a strain-softening material description [4] (Appendix B). Because posttest static splitting tests were performed on the rods from Tests 42 and 43, specimens from these rods are not available for inspection for microcracks. Test 41 was performed with no instrumentation, and it was not previously simulated. In the current effort, one 5-cm-long segment from this rod (41-B1) was inspected for microcracks (Figures 4 and 5). We also computed the response of Test 41 using the same strain-softening parameters used to simulate Tests 42 and 43. We then compared the distribution of peak fracture volume per unit area (δ) with the map of the microcracks observed in specimen 41-B1.

Figure 9 shows the material description used to computationally simulate Test



(a) Stress versus strain (0.635-cm cell).

(b) Stress versus fracture volume per unit area.



(c) Strength distribution.

Figure 9. Strain-softening model used to numerically simulate Test 41.

RA-3717-18

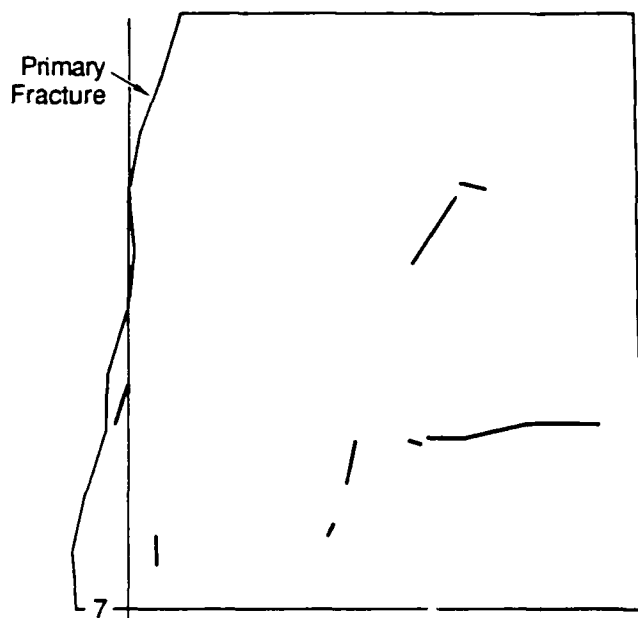
41. The $\sigma - \delta$ relation, the 0.635-cm cell size, and the $\sigma - \epsilon$ relation are the same as used for Tests 42 and 43. The location of the weak cell corresponds to the observed location of the primary fracture in the rod (+0.7 cm). In the computation, the weak cell failed completely and several cells on both sides of the weak cell softened without breaking. The computed peaks of the fracture volume per unit area in each cell corresponding to specimen 41-B1 are compared with the microcrack map of that specimen in Figure 10. The location of the computed maximum tensile damage agrees with the location of the observed concentration of microcracks to within about 1 cell width.

Test 103

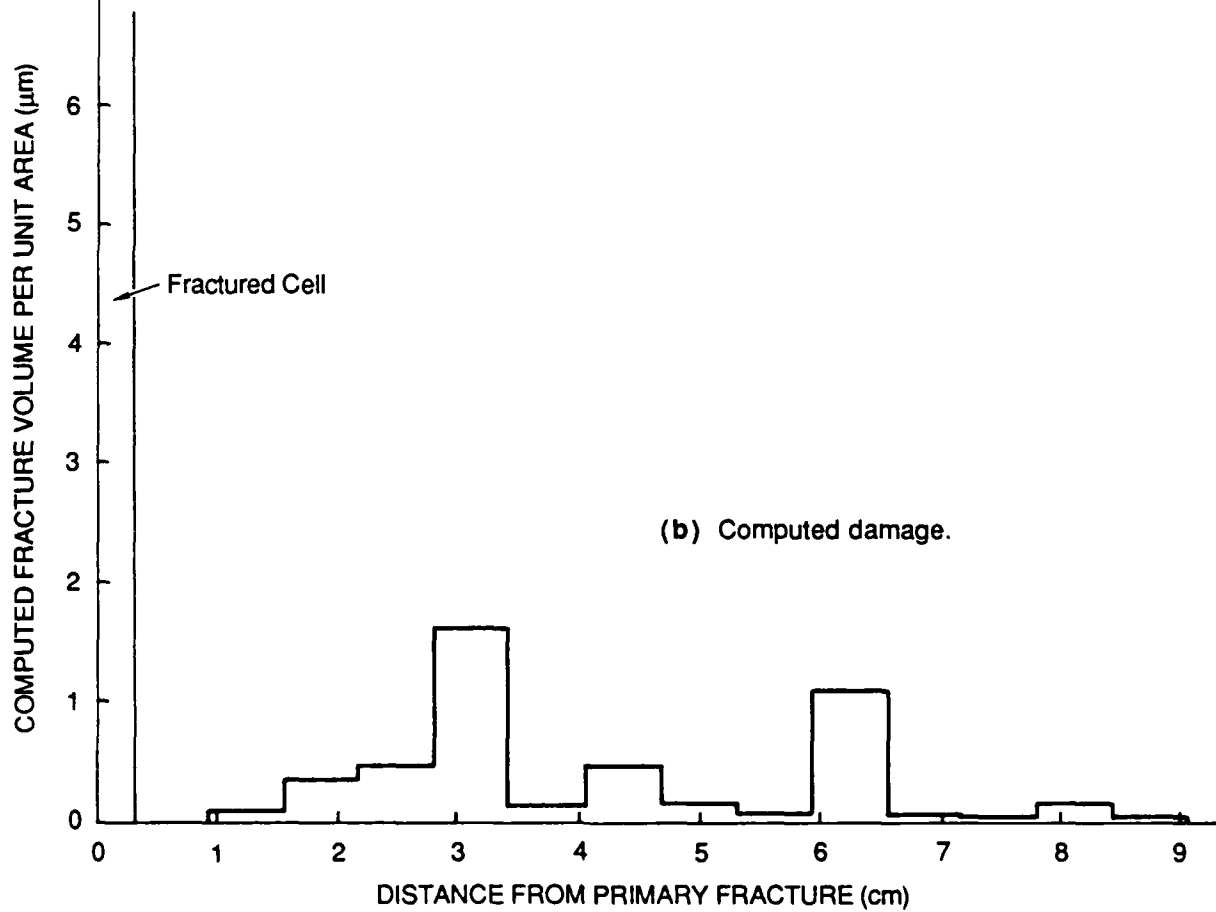
Tests 101 to 106 were all performed on rods made of a concrete similar to but not the same as that used in the earlier tests [2]. The static uniaxial preload in Test 103 was 17.3 MPa. Strain gages were used at ± 2.54 cm, ± 7.62 cm, and ± 15.2 cm from the midpoint of the rod. Fracture occurred at +2.86 cm.

The strain histories from this test were simulated computationally using the assumed material description shown in Figure 11. The strength is much higher than that used in the simulations of Tests 41, 42, and 43, but the material cell size and the critical fracture volume per unit area are about the same. Two types of unloading were used. The one with stress and strain returning to zero implies that all cracks close completely during unloading; the one with the unloading slope equal to the elastic loading slope implies that the cracks remain open during unloading.

Figure 12 shows the comparisons between the measured axial strains and those computed with the assumed material properties. Some of the strain records were matched better with unloading to the origin; others were matched better with elastic unloading. This apparent inhomogeneity was also present in earlier results [1,4].

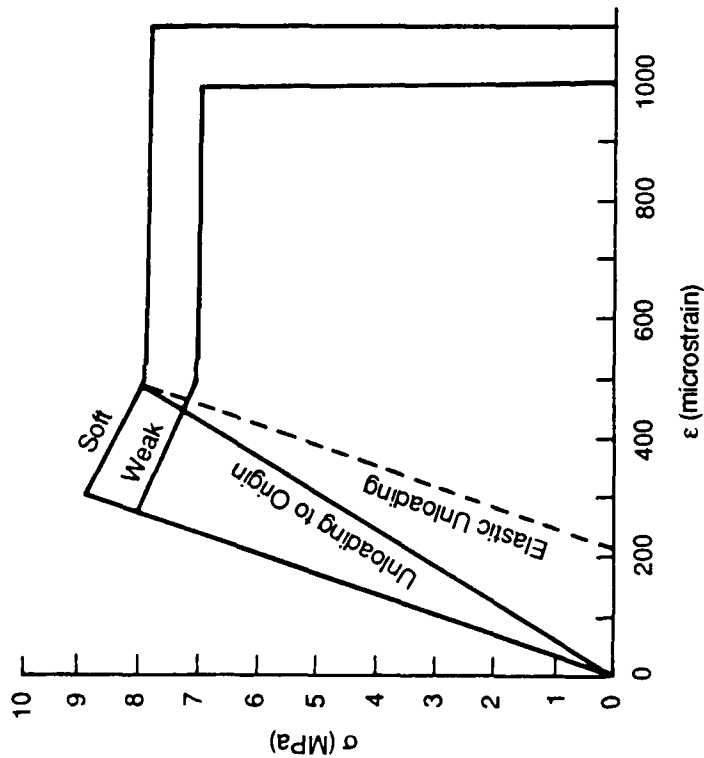


(a) Microcrack map.

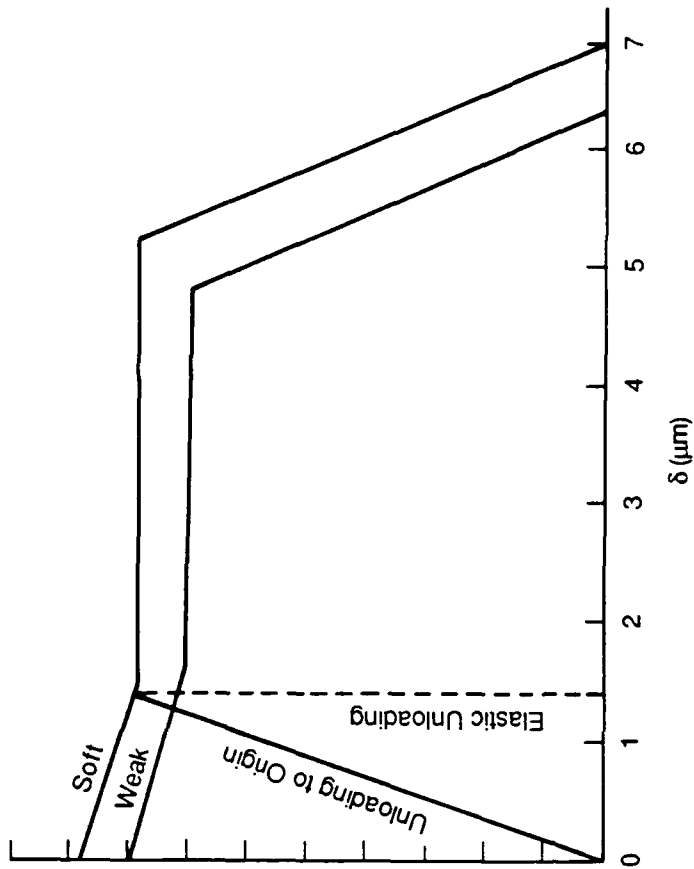


RA-3717-19

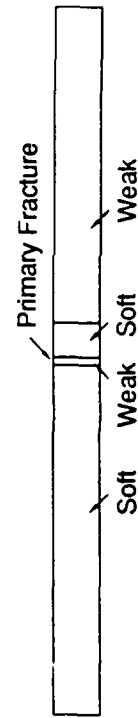
Figure 10. Comparison of computed and observed damage in specimen 41-B1.



(a) Stress versus strain (0.635-cm cell).



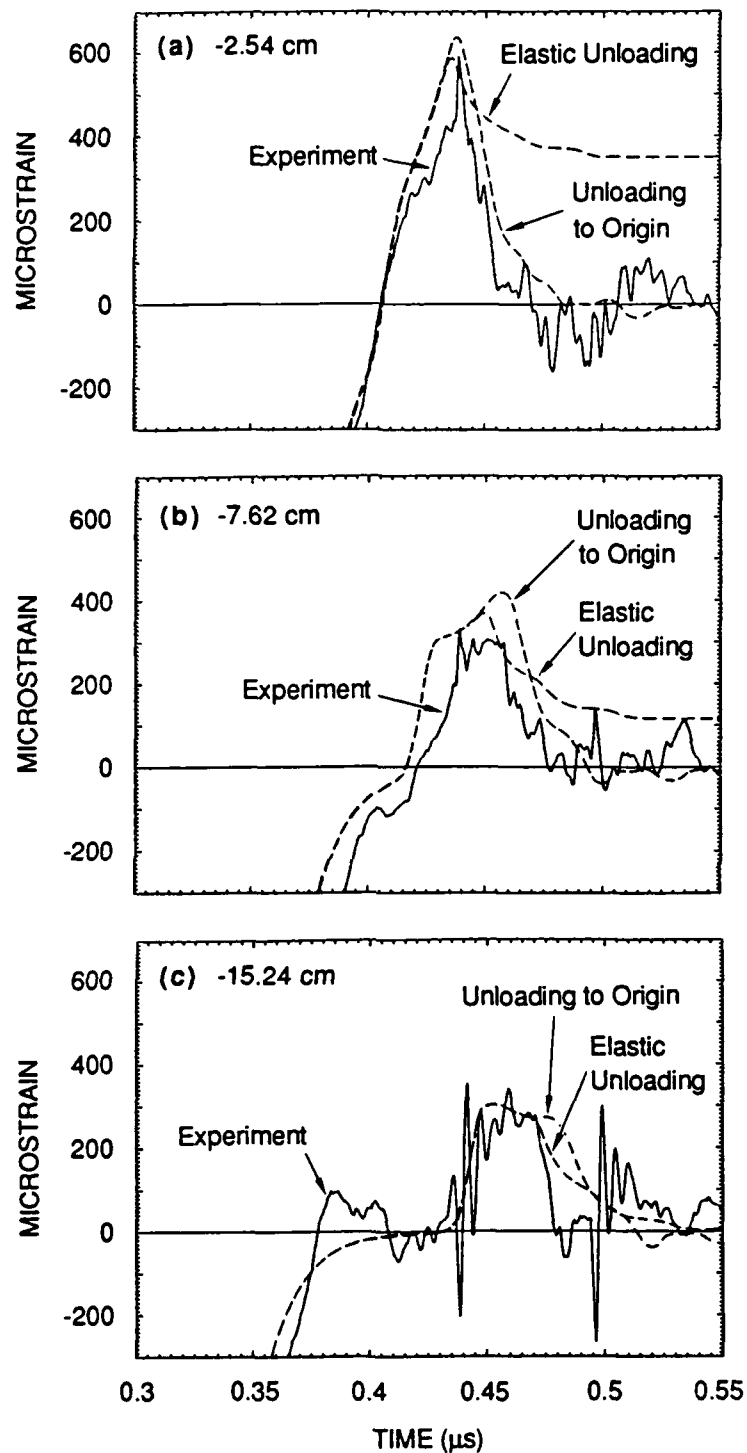
(b) Stress versus fracture volume per unit area.



(c) Test 103 strength distribution.

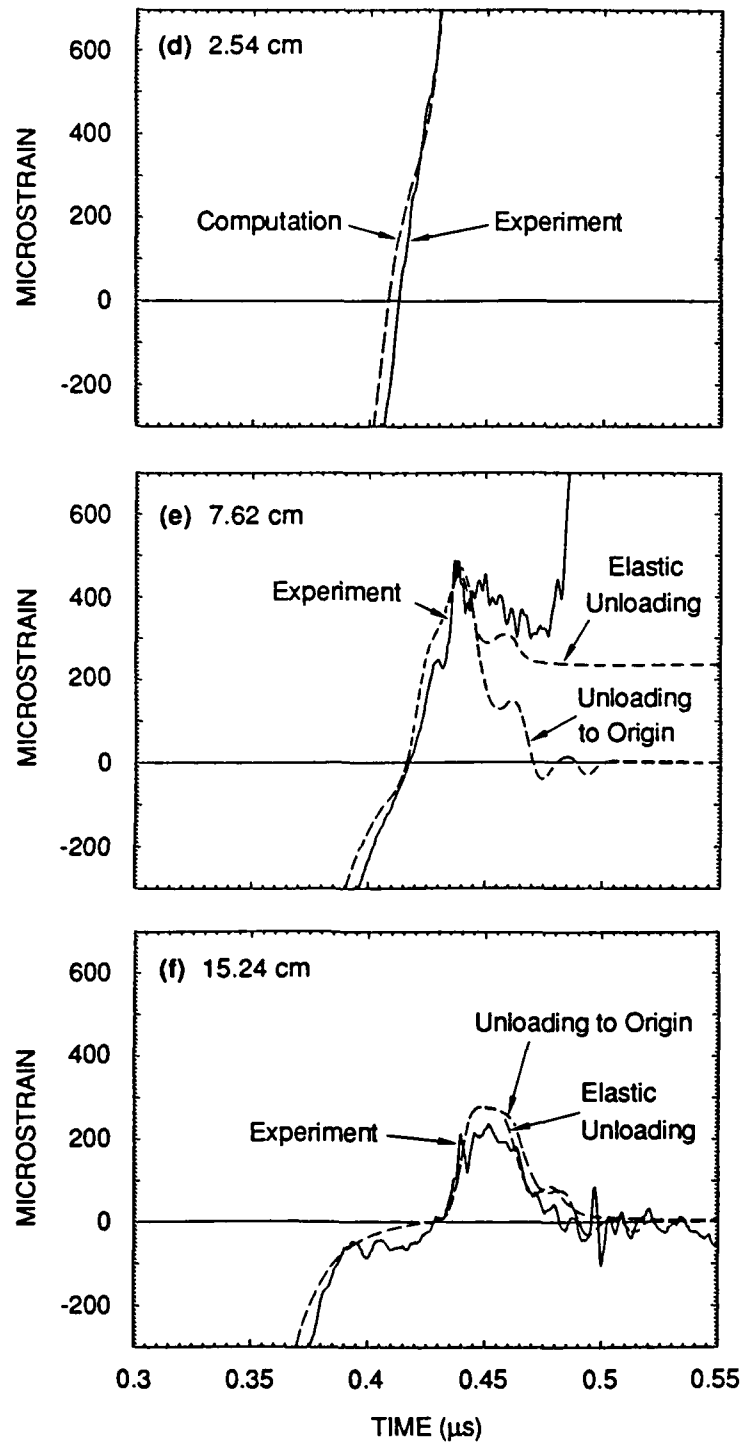
RA-3717-20

Figure 11. Strain-softening model used to numerically simulate Test 103.



RA-3717-21

Figure 12. Comparison of computed and measured axial strains in Test 103 (Continued).
17.3 MPa prestress; primary fracture at +2.86 cm.



RA-3717-22

Figure 12. Comparison of computed and measured axial strains in Test 103 (Concluded).
17.3 MPa prestress; primary fracture at +2.86 cm.

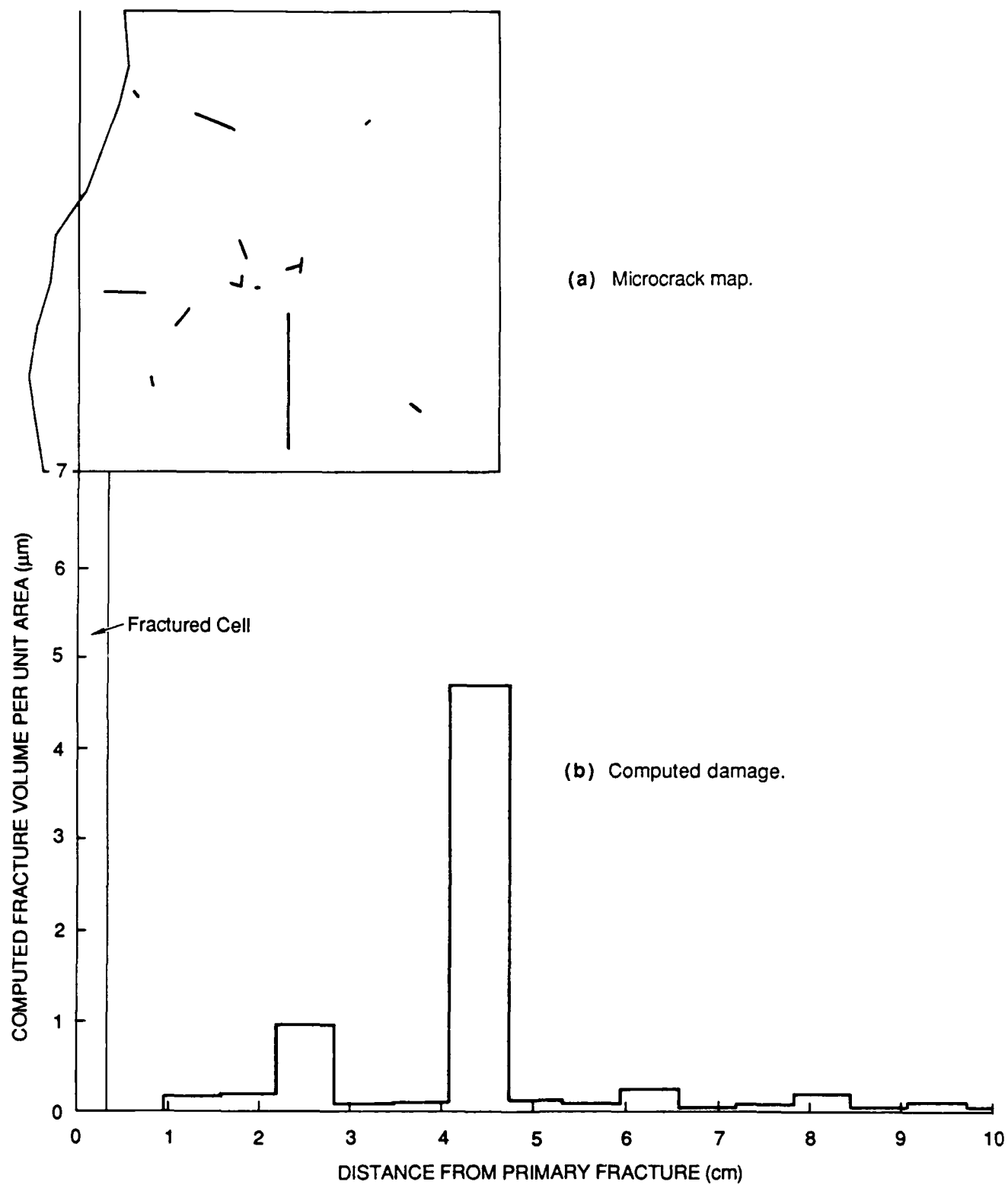
Figures 13 and 14 compare the computed peaks of fracture volume per unit area computed in each cell corresponding to specimens 103-B1 and 103-T1 with the microcrack maps of these two specimens. The computed concentrations of damage at about ± 2.5 cm from the primary fracture are consistent with the observations. However, the predicted damage at about ± 4.5 cm from the primary fracture was not seen in the microscopic inspection. Perhaps we will find damage in the adjacent specimens (103-B2 and 103-T2).

Conclusions and Recommendations

The strain-softening model we use to interpret the dynamic tension experiments on concrete is based on the concept that a material cell contains a single site of localization (fracture) and that the fundamental property of the material is the relation between stress and fracture volume per unit area (average crack opening). Within this framework, the material cell dimension represents the spatial frequency of localization sites in an inhomogeneous material. In the previous study, a 0.635-cm material cell size was found to give the best agreement with measured strains and observed fractures in the four experiments simulated.

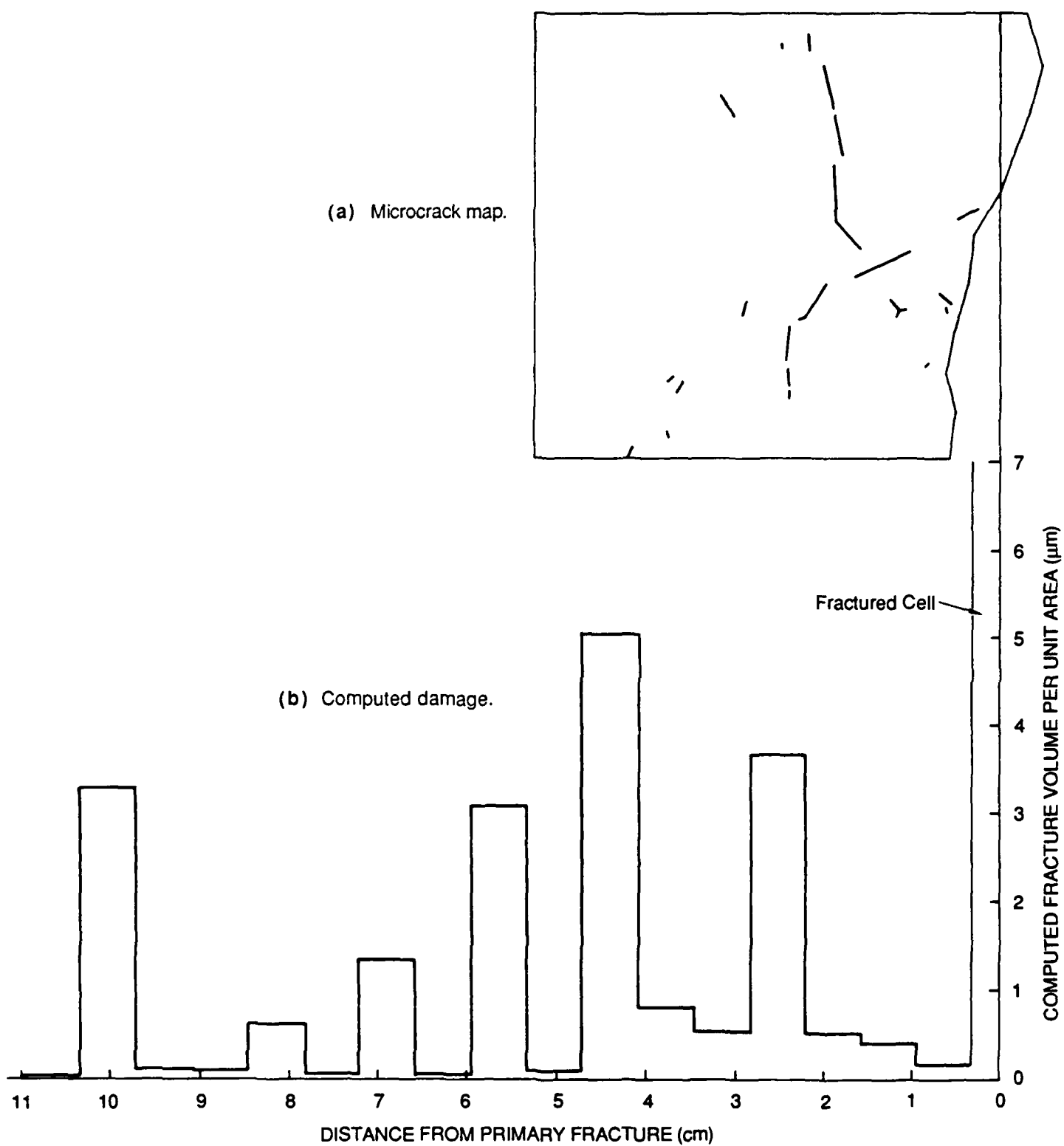
We used the simple strain-softening model to match the strain histories and tensile damage in dynamic tension tests on two concretes with static tensile strengths of about 3.5 MPa. We chose the same material cell size used previously (0.635-cm) and adjusted the relation between stress and fracture volume per unit area to match the experimental results. The apparent dynamic strength of the concrete used in Tests 101 to 106 is about twice as high as the dynamic strength of the concrete used in Tests 41 to 46.

Several more of the experiments performed previously should be interpreted with the strain-softening model to extend our knowledge of how the concrete behaved in these experiments. We also recommend additional study of the apparent natural material cell size for a better understanding of its source and meaning.



RA-3717-23

Figure 13. Comparison of computed and observed damage in specimen 103-B1.



RA-3717-24

Figure 14. Comparison of computed and observed damage in specimen 103-T1.

COMPUTATION OF EFFECTIVE MODULI FOR A CRACKED MATERIAL

A computational model for representing the fracturing processes in concrete and the mechanical response of concrete to loading must contain descriptions for the initiation, growth, and coalescence processes for cracks. In addition, it is necessary to know the effective stiffness of the partially cracked material at all stages of damage. The current study of effective moduli is an effort toward evaluating these stiffnesses.

Solution for Stress Intensity Factors and Crack Openings

Kachanov [7] has constructed an approximate analysis for computing stress intensity values for arrays of cracks of arbitrary locations, lengths, and orientations in an elastic solid. The method is based on classical solutions for the stress states around a two-dimensional flat crack in an infinite elastic body under external tractions. The procedure provides for a simultaneous solution for the stress intensity values (K_I and K_{II}) at each end of each crack in the array. With these K values, the crack opening shape is determined. From the crack shape, the average crack opening strain in the body can be found.

Kachanov considers an array of two-dimensional cracks embedded in an elastic material under a remote loading ($\bar{\sigma}^\infty$). The crack lengths are given by L_i and the orientations by the unit normals \bar{n}_i .

The stress acting along each crack is a superposition of the external stress field on the stress field caused by the opening of each of the other cracks. To proceed, Kachanov considers just two cracks and their interactions. He evaluates first the interaction stresses $\sigma_{ij}^n(\xi)$ and $\sigma_{ij}^r(\xi)$: the stresses at position ξ along the j th crack generated by uniform normal and shear tractions of unit intensity along the i th crack. These stress quantities are obtained from a standard elastic analysis of the stresses in an infinite body resulting from normal and shearing stresses applied

to the faces of an embedded crack (here the i th crack). To obtain the actual stresses along the j th crack, we multiply $\sigma_{ij}^n(\xi)$ and $\sigma_{ij}^t(\xi)$ by the average of the normal or shear stresses on the i th crack: $\langle P_i \rangle$ and $\langle \tau_i \rangle$. This use of the average stresses on the cracks (instead of the actual strongly varying stresses) is the essential ingredient of Kachanov's method that simplifies the solution enough to make it practical.

After the interaction stresses are determined, the stress state along each crack is computed. From this stress state, the K_I and K_{II} stress intensity factors are evaluated for each crack.

Next, these stress solutions are used to evaluate the normal opening of the crack and its shearing displacement. These procedures are given in more detail in Appendix C. A computer program, KCRACK, was written for routine evaluation of stress intensity factors and crack opening. The solution procedure is also described in Appendix C and the program is listed there.

Results are given in Appendix C for stress intensity factors for pairs of identical cracks along the x -axis. The K values are determined as a function of the separation of the cracks and compared with exact solutions. The error in the K values increases as the separation distance between the cracks decreases. The error is less than 1% until the crack tip separation is less than 10% of the crack lengths [7]. At this point the K value is 45% larger than the K value computed for an isolated crack. Therefore, it appears that Kachanov's procedure is essential for evaluating the cracked state of a body if the crack tips are near each other.

Computation of Effective Moduli

When the crack stress intensity factors and the crack openings have been computed, it is possible to determine the effective moduli for a cracked body. Such moduli are termed "effective" because they provide an average of the response of the intact elastic material around the cracks plus the response of the cracks

themselves.

Before exploring the two-dimensional problem of computing moduli using Kachanov's method, we introduce the determination of the longitudinal modulus of a rod of elastic material with transverse cracks. This rod problem will serve to indicate the essence of the method and assumptions behind the more complex derivation of Kachanov. Let us examine the longitudinal stiffness of a rod with radius R and length L with N cracks all located such that the normals to their planes are along the axis of the rod. The cracks have radii R_i . Under a longitudinal stress (σ), their tensile opening is given by

$$\delta_i = \frac{4(1 - \nu^2)}{\pi E} R_i \sigma$$

where δ_i is one-half the maximum separation of the crack faces and E and ν are Young's modulus and Poisson's ratio. The crack faces form an ellipsoid with three semiaxes, δ_i , R_i , and R_i . Therefore, the volume of the opening of the crack is

$$V_c = \frac{4\pi R_i^2 \delta_i}{3} = \frac{16(1 - \nu^2) R_i^3 \sigma}{3E}$$

To determine an effective elongation (δ_{ei}) for the crack, we average this crack volume over the area (πR^2) of the rod.

$$\delta_{ei} = \frac{4}{3} \left(\frac{R_i}{R} \right)^2 \delta_i = \frac{16(1 - \nu^2) R_i^3 \sigma}{3\pi E R^2}$$

Now consider the elongation that occurs to the rod when a stress (σ) is applied. We assume that the intact elastic material is all under the same tensile stress (σ) as it would be for an uncracked rod, so the elongation is

$$\Delta L_m = \frac{\sigma}{E} L$$

In addition to this elongation, we have the elongation given by all the cracks:

$$\Delta L_c = \sum \delta_{ei} = \frac{16(1 - \nu^2)\sigma}{3\pi E R^2} \sum_{i=1}^N R_i^3$$

The effective modulus (M_e) simply relates the applied stress (σ) to the average strain induced in the rod.

$$M_e = \frac{\sigma}{(\Delta L_m + \Delta L_c)/L} = \frac{E}{1 + \frac{16(1 - \nu^2) \sum R_i^3}{3V_r}}$$

where V_r is the volume of the rod: $\pi R^2 L$. From the equation for M_e , we see that the stiffness of the cracked rod is reduced by the factor in the denominator that is a function of the cube of the crack radii.

In deriving the effective moduli for a cracked body, Kachanov [7,8] uses his solution for the stress intensity factor and crack opening for an array of cracks. He computes, one at a time, the compliance factors (C_{ijkl}), where

$$\epsilon_{ij} = C_{ijkl} \sigma_{kl}$$

and ϵ_{ij} and σ_{kl} are the average strain and stress on the cracked body. The compliance term C_{ijkl} is obtained by applying the stress σ_{kl} to the body, computing all the strain and distortion quantities for the body and cracks, and summing those which contribute to ϵ_{ij} . C_{ijkl} is then computed by inverting the preceding

equation. The corresponding effective stiffness matrix is computed by inverting the compliance matrix. Details of this derivation are given in Appendix C.

With a procedure available for computing the moduli for a cracked body, we can undertake a number of computations:

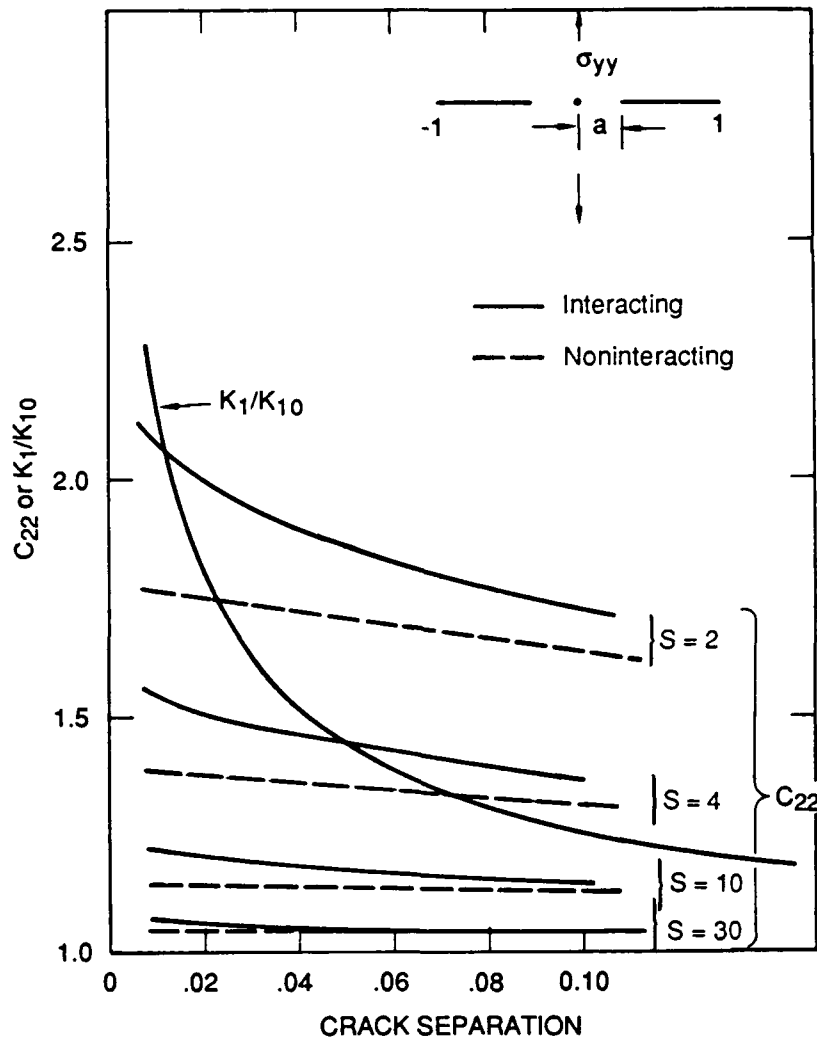
- Evaluate moduli for some cases for which there are analytical solutions.
- Compute the moduli for simple parallel arrays of cracks and compare these results with the results of simpler procedures.
- Evaluate the moduli for arrays of cracks and determine the sensitivity of the moduli to closeness of the cracks.

No analytical solutions were found that matched the cases possible with the Kachanov method, so the first type of computation was not performed. The other types of studies were undertaken, and the results are given below.

Parallel Cracks in Line. The first analysis concerns a pair of horizontal cracks of length $1 - a$ with a spacing of $2a$ between their nearer tips. A stress (σ_{yy}) was applied to a block containing these cracks. The results in Figure 15 show the stress intensity factors and compliance (C_{22}) for a range of a values and cross-sectional areas (S). The relative stress intensities, K_I/K_{I0} (stress intensity at the near tip normalized by the stress intensity for an isolated crack), increase markedly during this interval of a values. The compliance factors increase more moderately over the same range of a . These compliances are normalized such that the compliance for a crack-free body is 1. Here the results for C_{22} are grouped according to the area (S). The effect of the area can be easily accounted for as follows:

$$C_{S=30} = \frac{2}{30}(C_{S=2} - 1) + 1$$

Therefore, the area was held constant ($S = 2$) in the rest of the study.



RA-3717-26

Figure 15. Variation of compliance and normalized stress intensity with crack separation for two cracks in line.

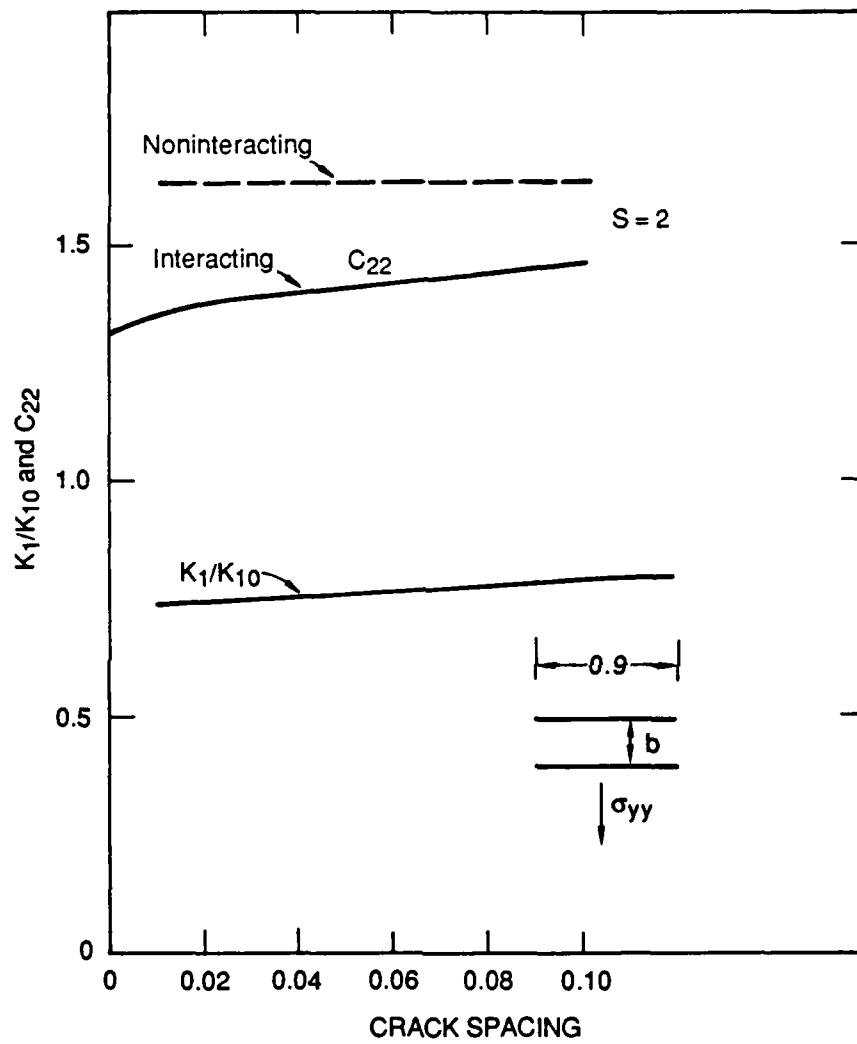
S = area.

Pairs of Cracks, One Above the Other. The next series of calculations was made for pairs of parallel cracks, one above the other, with a spacing (b). The results shown in Figure 16 indicate that neither the stress intensity factor nor the compliance factor (C_{22}) is very sensitive to the crack spacing (b). For large spacings, the K_I value would certainly approach K_{I0} , the value for an individual crack. Hence, the presence of a parallel crack tends to reduce the stress intensity factor. Similarly, the compliance is reduced when the cracks are near each other, although the effect is not large. The compliance for the pair of cracks approaches that for a single crack (1.318 for the present geometry), as expected.

Four Crack Sets. The third case concerns a set of four cracks, two horizontal and two vertical, extending directly out from the origin (as shown in Figure 17). For large distances (a) between the crack tips, the response of this array is much like that shown in Figure 15 for two horizontal cracks; but as the spacing decreases, the vertical pair of cracks begins to influence the interaction. Although the stress is applied in the σ_{yy} direction only, horizontal stresses act on the vertical cracks, causing a large stress intensity, K_2 (for this configuration K_{20} , the stress intensity for a noninteracting crack, is zero). As the spacing decreases, this stress intensity of the vertical cracks increases faster than the stress intensity of the horizontal cracks. The compliance (C_{22}) for the noninteracting case is the same as that shown in Figure 15. From the symmetry of the problem, here $C_{11} = C_{22}$, with or without crack interaction. Because of the importance of the vertical cracks in the effects on the stress field, the compliance for interacting cracks increases faster with decreasing spacing in this case than in Figure 15.

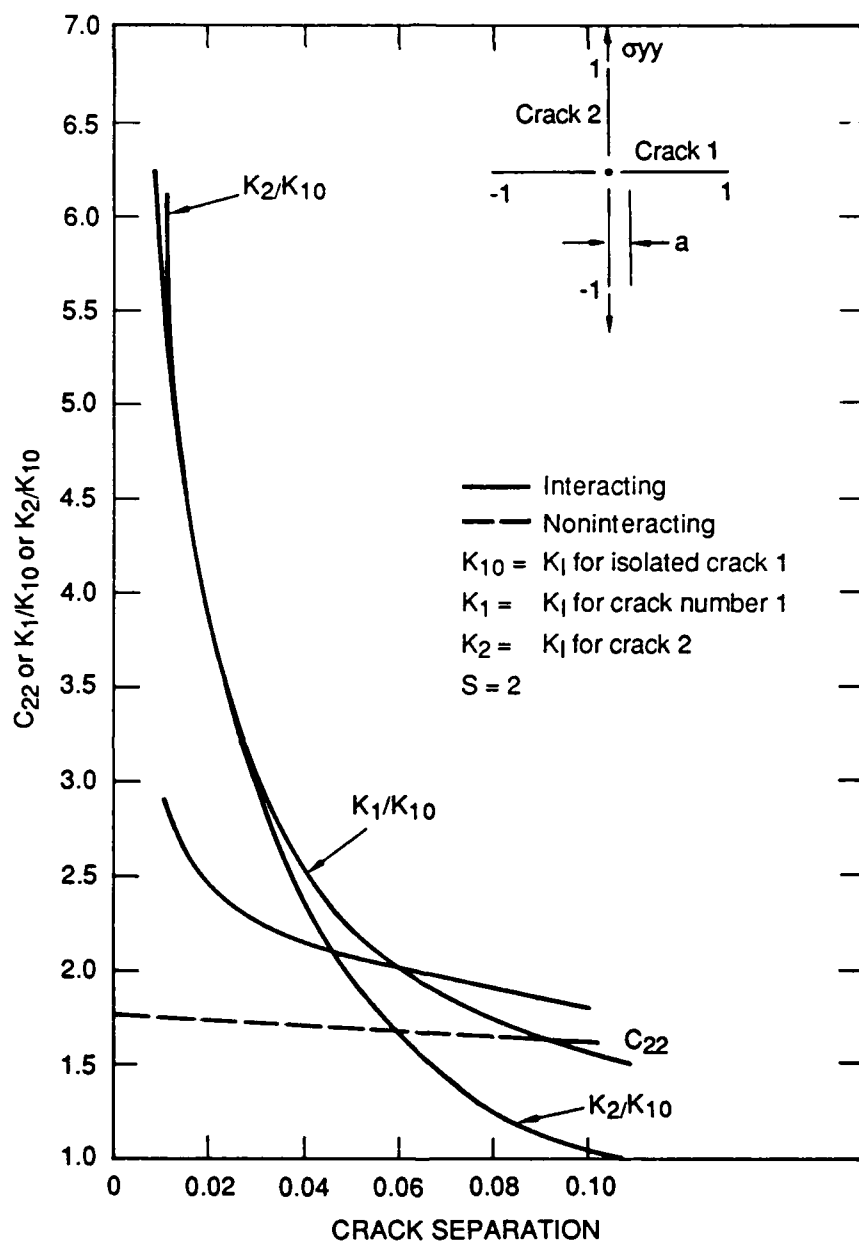
Conclusions and Recommendations

From the simulations and the attempts to examine cases with known results, some of the limitations of the Kachanov approach became clear. These limitations are important in the determination of the effective stiffness, but not in the determination of stress intensity factors or crack face displacements. The anal-



RA-3717-27

Figure 16. Variation of compliance and normalized stress intensity with vertical spacing between two horizontal cracks.
 $S = \text{area}$.



RA-3717-28

Figure 17. Variation of compliance and normalized stress intensity with crack spacing for four orthogonal cracks.
 $S = \text{area.}$

ysis treats in detail the interaction between two or more cracks, but it does not consider boundary conditions except those at infinity. Hence, one cannot readily take a finite region such as a computational cell, lay out an array of cracks, and determine the effective moduli of this assemblage. The size of the computational cell only enters the analysis with the factor S , not with an explicit location of cell boundaries.

A possible improvement to account for the presence of cell boundaries would include the following steps:

- Lay out a set of crack arrays such that they repeat. For example, the set in Figure 17 could be arranged with identical sets above, below, and on both sides of the set of interest. Then the computational cell being considered is bounded by the symmetry planes between the sets of cracks.
- Perform the analysis as above to determine the stress intensity factors and crack openings for all cracks.
- Construct the compliance matrix for only the central cell, using only the cracks present in that cell.

The foregoing procedure would provide a closer approximation to the compliance of a bounded region. Yet this procedure also suffers from the assumption that the compliance of the matrix material around the crack is under a uniform stress state.

REFERENCES

1. J. K. Gran and L. Seaman, "Observations and Analyses of Microcracks Produced in Dynamic Tension Tests of Concrete," SRI International Final Report to AFOSR, Contract No. F49620-82-K-0021 (1986).
2. J. K. Gran, "Development of an Experimental Technique and Related Analyses to Study the Dynamic Tensile Failure of Concrete," SRI International Annual Report to AFOSR, Contract No. F49620-82-K-0021 (1985).
3. J. K. Gran, Y. M. Gupta, and A. L. Florence, "An Experimental Method to Study the Dynamic Tensile Failure of Brittle Geologic Materials," *Mechanics of Materials*, Vol. 6, pp 113-125 (1987).
4. J. K. Gran and L. Seaman, "Strain-Softening Calculations for Concrete in Dynamic Uniaxial Tension," *ASCE Journal of Engineering Mechanics* (in press).
5. L. Struble, "Characterizing the Microstructure of Cement Paste and Mortar by Backscattered Scanning Electron Microscopy," National Bureau of Standards, presented at the Workshop on the Performance of Concrete and Cement Materials, Wright-Patterson AFB, OH (October 1986).
6. E. K. Attiogbe and D. Darwin, "Submicroscopic Cracking of Cement Paste and Mortar in Compression," University of Kansas Center for Research, SM Report No. 16, (November 1985).
7. M. Kachanov, "A Simple Technique of Stress Analysis in Elastic Solids with Many Cracks," *International Journal of Fracture*, Volume 28, pp. R11-R19 (1985).
8. E. Montagut and M. Kachanov, "On Crack-Microcrack Interactions and Elastic Moduli of the Damage Zone," ASME Winter Annual Meeting, Boston, MA (1987).

APPENDIX A

Reference:

J. K. Gran, Y. M. Gupta, and A. L. Florence, "An Experimental Method to Study the Dynamic Tensile Failure of Brittle Geologic Materials," *Mechanics of Materials*, Vol. 6, pp 113-125 (1987).

AN EXPERIMENTAL METHOD TO STUDY THE DYNAMIC TENSILE FAILURE OF BRITTLE GEOLOGIC MATERIALS

J.K. GRAN, Y.M. GUPTA * and A.L. FLORENCE

Poulter Laboratory, SRI International, Menlo Park, CA 94025, U.S.A.

Received 5 September 1986; revised version received 9 December 1986

An experimental method was developed to study the tensile failure of brittle geologic materials at strain rates of approximately 10 to 20/s. In these experiments, a cylindrical rod specimen is first loaded in static triaxial compression, then the axial pressure is released from each end simultaneously and very rapidly. The resulting rarefaction waves interact in the center of the rod to produce a dynamic tensile stress equal in magnitude to the original static compression. The pressure acting on the radial surface is approximately constant during the experiment. As an application of this method, several experiments were performed on concrete. Transient measurements were made of the axial load at each end, the confining pressure, and axial and circumferential surface strains at several locations along the length of the rod. Usually a single fracture occurred near the midpoint of the rod. In some experiments multiple fractures occurred. Assuming the peak observed strains in these experiments to be elastic, the unconfined tensile strength of the concrete at a strain rate of 10 to 20/s was, on average, approximately 40% higher than the static splitting tensile strength. At the same strain rate, the tensile strength with 10 MPa confining pressure averaged approximately 100% higher than the static splitting tensile strength and 40% higher than the unconfined tensile strength at 10 to 20/s. Nonlinear analyses indicate that these estimates are reasonable, but that in general the assumption of elastic response is not valid. To match the measured strain histories with calculations requires that the rod be modeled inelastically.

1. Introduction

The study of dynamic tensile failure in geologic materials and concrete is important to many engineering applications, such as rapid excavation, in-situ fracture, and impulsive loading. It is also of fundamental interest in the field of mechanics of materials. Tensile failure in these materials is produced by the nucleation, growth, and coalescence of microcracks, and the tensile strength is the stress at which this process of accumulating damage becomes locally unstable. Most geologic materials and concrete are brittle, that is, the damage growth and strength reduction occur in a very short, but finite time. Details of these processes are important in applications in which the load duration is comparable to the time required for tensile failure. In such problems, there

is a strong interaction between the applied load and the growth of damage. Hence, an important need in the study of dynamic tensile failure in brittle geologic materials is to characterize the failure process for a wide range of strain rates.

Tensile failure at strain rates greater than $10^3/s$ has been observed in concrete (Gupta and Seaman, 1979) and rock (Grady and Kipp, 1979) in uniaxial strain plate impact experiments. Kipp, Grady, and Chen (1980) have shown that, at these very high strain rates, the tensile strength increases with strain rate to the power of $\frac{1}{3}$. Tensile failure at strain rates between 10/s and 100/s has been produced by reflecting a compressive stress pulse from the free end of a long rod specimen. Birkimer (1968) and Goldsmith, Kenner, and Richetts (1968) used this method in experiments on concrete, in which the compressive pulse was produced by an impact of a spherical pellet. Abbott and Cornish (1965) and Felix (1977) studied ceramics and oil shale, respectively, using explo-

* Present address: Department of Physics, Washington State University, Pullman, WA 99164, U.S.A.

sive charges to produce the compressive pulse. At these intermediate strain rates the tensile strength dependence on strain rate is not understood, although various empirical models have been described (Reinhardt, 1985). Part of the difficulty is that rod impact experiments are difficult to analyze because the loading conditions are not well defined. An accurate specification of the loading conditions is needed for a quantitative analysis of the data.

The effects of loading path, including confining stresses, are also important in studies of dynamic tensile failure of geologic materials. These effects have received minimal study, however, because loading rates and loading paths cannot be varied independently with most experimental methods. In each of the studies mentioned above, only uniaxial strain loading or uniaxial stress loading was considered.

In this paper we describe the development of an experimental method that addresses the issues indicated above for brittle geologic materials. The experiment is based on the concept of the interaction of two rarefaction waves to produce tensile failure in a rod-shaped specimen. This experiment meets the following objectives:

- (1) to measure the tensile response at strain rates between 10/s and 100/s, including the strength reduction with the growth of tensile damage,
- (2) to examine the effect of confining pressure on tensile failure at these strain rates, and
- (3) to accurately characterize the loading conditions.

As an application of the method, we have chosen to study concrete because of the current interest in its dynamic properties, and because of its similarities with geologic solids. The method is also applicable to hard geologic solids that are weak in tension. Several experiments were performed on concrete and selected results are presented here. Complete details of the experiments and accompanying analyses are presented elsewhere (Gran, 1985).

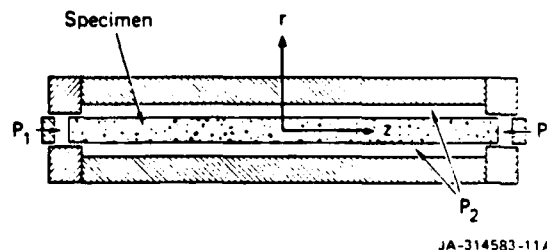
2. Experimental concept

Approach

The concept underlying the experiments is to use the interaction of rarefaction waves to produce dynamic tensile stresses in a rod-shaped specimen. A schematic view of the experimental technique is shown in Fig. 1. A cylindrical rod is initially held in static compression, in both the axial and radial directions. The axial (P_1) and radial (P_2) pressures are controlled separately. The radial pressure is approximately constant during the experiment. The axial pressures at each end of the rod are released simultaneously, sending axial rarefaction waves toward the center. Individually, these waves bring the rod only to zero axial stress, but when they superpose at the midpoint, they bring the rod to a tensile stress equal in magnitude to the original axial compression. Tensile failure occurs near the center of the rod if the resultant tensile stress exceeds the tensile strength for these conditions.

Transient measurements are made of the axial load at each end, as well as the confining pressure and axial and circumferential surface strains at several locations along the length of the rod. The pressure measurements define the boundary conditions. The strain measurements record the effects of the tensile failure process on the stress waves propagating in the rod.

Because the specimen is initially loaded in static axial compression, this method is applicable to materials for which the dynamic tensile strength is lower than the static compressive strength.



JA-314583-11A

Fig. 1. Dynamic tensile loading technique with confinement. End pressures (P_1) are released rapidly and simultaneously, radial pressure (P_2) is held.

Wave propagation preliminaries

The rarefaction waves propagating from the ends of the rod are not step waves because the applied pressure decays to zero in a finite time. This fact makes it more difficult to visualize the stress distributions in the region of wave interaction. To illustrate and understand the complexities introduced by the finite decay time, two idealized examples of rod response are considered. The first example is an elastic rod with no failure. The second example is a rod that fractures at a single point but remains elastic everywhere else. This example can also be visualized as two elastic half-rods connected together by a weak bond.

For one-dimensional linear elastic response, the axial stress or strain distribution along the length of the rod at any time is the solution of an initial value problem for the one-dimensional wave equation. The well-known solution of this problem is the sum of two waves traveling in opposite directions at the same speed (Berg and McGregor, 1966). The solutions for the following examples were obtained using the principle of superposition.

Plots of the axial stress and strain distributions for several times are shown in Fig. 2 for an elastic rod. For simplicity in this example, a linear decay in applied pressure is assumed. Tensile stress is taken to be positive. The dashed lines represent the two rarefaction waves and the static compression. The solid line is the total stress produced by the superposition of the two rarefaction waves and the preload. The distance the wave travels during the time required for the pressure to drop to zero is denoted by λ . For the assumption of one-dimensional response to be appropriate, λ should be greater than a few rod diameters. In the limiting case of instantaneous pressure drop, the rarefaction waves would be step waves and λ would be zero. The other terms in the figure are defined as follows: σ_0 is the magnitude of the peak axial stress, ϵ_0 is the corresponding peak axial strain, and X is the position along the length of the rod, with the origin at the midpoint.

The sequence of stress distributions illustrates that tension first occurs in a central region of width λ , at the time when the rarefaction waves have overlapped by $\frac{1}{2}\lambda$. As the waves overlap

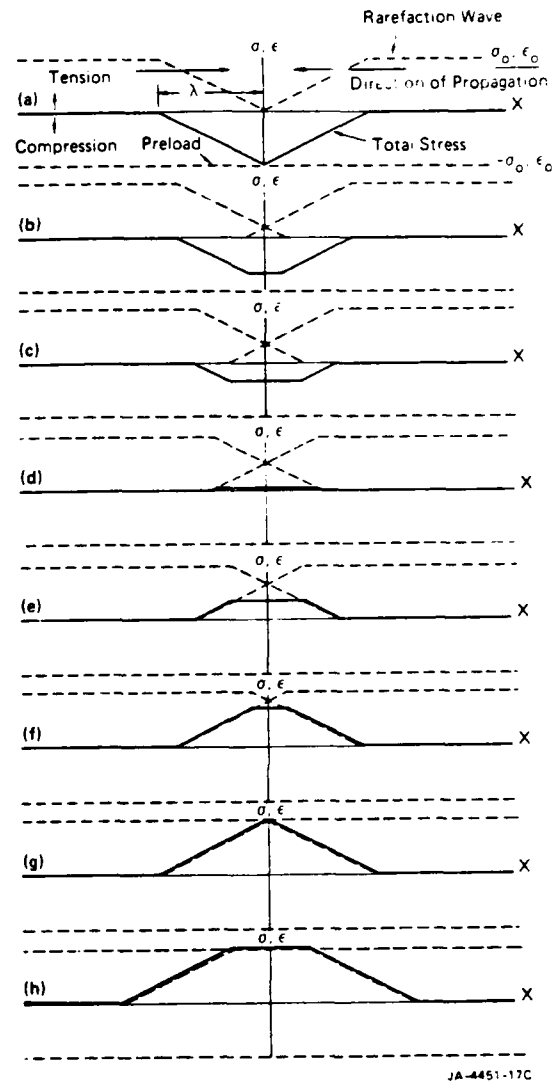


Fig. 2. Axial stress and strain distributions in a one-dimensional elastic rod with ramp unloading. Time increases from (a) to (h).

further, the region of tension broadens. The midpoint is the first point to attain the maximum tensile stress, σ_0 . However, intermediate values of tension are attained simultaneously in a finite region. As the tension increases to σ_0 , the region of uniform tension becomes narrower. When the wavefronts overlap by λ , the maximum tension is σ_0 and exists only at the midpoint. Thereafter, the

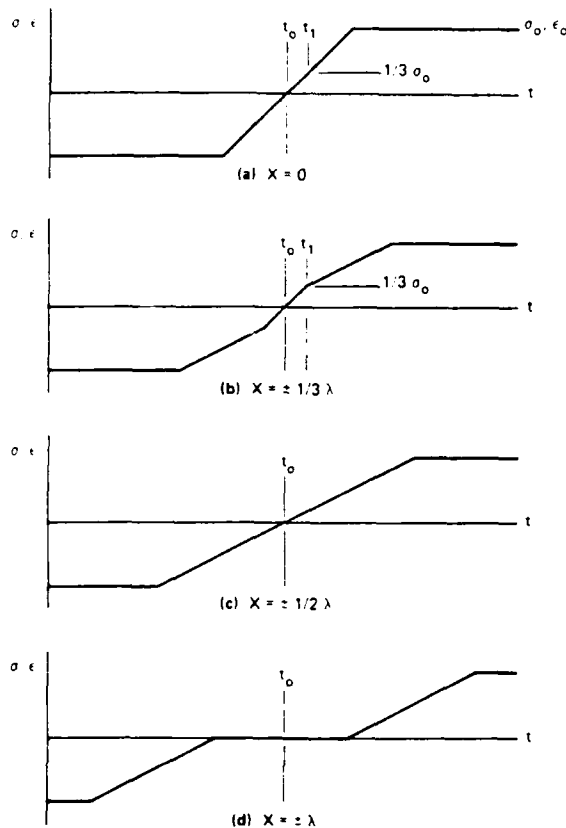


Fig. 3. Stress and strain histories in a one-dimensional elastic rod with ramp unloading.

region of maximum tension expands.

For this example, stress and strain histories at several points are plotted in Fig. 3. This figure shows that the stress history is different at every point (except pairs of points symmetrically located with respect to the origin). However, points that simultaneously reach intermediate values of tension also experience the same tensile stress history (and tensile strain rate) up to that time. For example, all points between $\pm \frac{1}{2}\lambda$ reach a tension of $\frac{1}{2}\sigma_0$ simultaneously. They also have the same stress history from the time they reach zero stress until the time they reach $\frac{1}{2}\sigma_0$.

The average tensile strain rate—the peak tensile strain divided by the rise time from zero strain—varies with position. The average tensile strain rate for $X \geq \frac{1}{2}\lambda$ is that produced by a single rarefac-

tion wave because the wavefronts do not overlap in this region. For $0 < X < \frac{1}{2}\lambda$ the wavefronts overlap, but the average tensile strain rate varies with distance from the origin because the times of arrival of the two wavefronts are staggered by different amounts. The average tensile strain rate at the midpoint is produced by the simultaneous arrival of both rarefaction waves, and is twice the strain rate at the more remote locations. Thus, the midpoint is the first point to reach the maximum stress and it experiences the highest average tensile strain rate.

This example shows that even without tensile failure, the stress profiles and stress histories are not simple. If σ_0 exceeds the dynamic tensile strength, the rod will fracture somewhere within

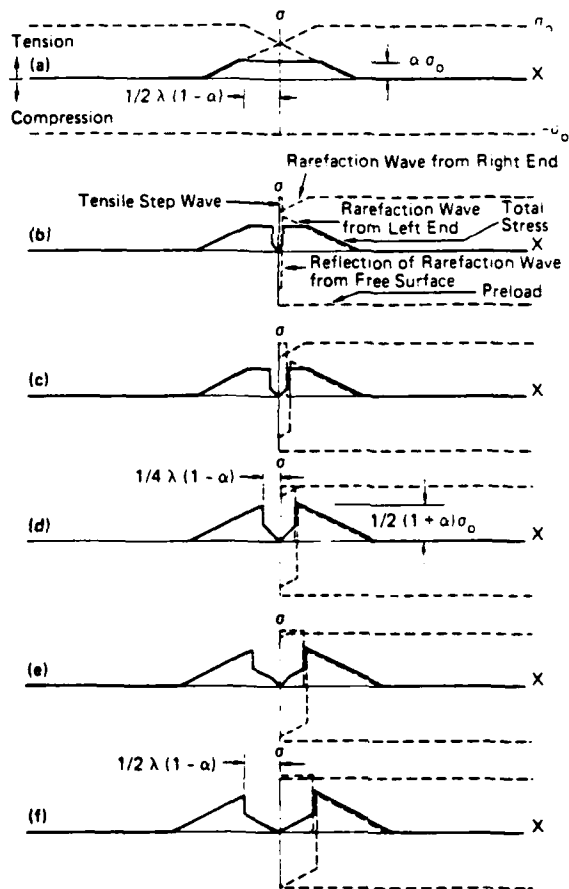


Fig. 4. Stress distributions in an ideally brittle rod with ramp unloading. Time increases from (a) to (f).

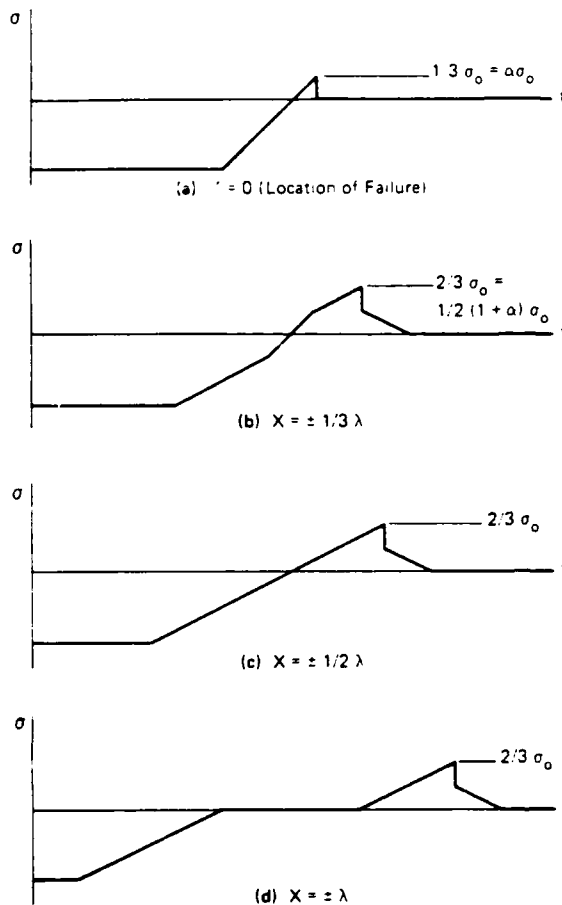


Fig. 5. Stress histories in an ideally brittle rod with ramp unloading.

the finite region that reaches the critical stress simultaneously, making subsequent stress profiles and stress histories even more complicated.

To illustrate the effect of fracture, an example with fracture occurring at the midpoint is illustrated in Figs. 4 and 5. In this example, the fracture is assumed to be ideally brittle and to occur instantaneously when a critical stress is reached. It is also assumed that the rod remains elastic at every point except the midpoint. The critical stress for fracture is assumed to be $\alpha\sigma_0$, where $0 < \alpha < 1$. The plots are drawn for $\alpha = \frac{1}{3}$. The dashed lines are the static preload, the rarefaction waves, the reflection of one rarefaction

wave from the new free surface, and the step wave required to satisfy the new stress-free boundary condition. The solid line is the total stress obtained by summation.

Figure 4(a) shows the stress distribution just before fracture. Figures 4(b) through 4(f) show the stress distributions after fracture. Although fracture is assumed to occur at the origin in this example, the figure illustrates that, at the time of fracture, the critical stress exists throughout the central region of width $\lambda(1 - \alpha)$. When fracture occurs, the stress at the midpoint immediately drops to zero, but the stress at the other points in the central region continues to increase. This is because the stress wave emanating from the fracture propagates at the same velocity as all the other waves. Until the effect of the fracture propagates to a given point, the stress at that point continues to increase as if fracture has not occurred. The portion of the rarefaction wave that has already propagated past the midpoint by the time fracture occurs has a peak of $\frac{1}{2}(1 + \alpha)\sigma_0$, which exceeds $\alpha\sigma_0$ for $\alpha < 1$. That is, if no other fracture occurs, the stress at every point except the midpoint will exceed the critical stress.

The stress histories at several points in this example are plotted in Fig. 5. The peak stress at the midpoint is less than the peak stress at every other point. The average tensile strain rate at the midpoint is equal to or greater than the average tensile strain rate at every other point. The maximum tensile stress $\frac{1}{2}(1 + \alpha)\sigma_0$ occurs first at $\frac{1}{2}\lambda$. The average tensile strain rate at this point is half that at the midpoint. The tensile stress history is different at every point between the origin and $\frac{1}{2}\lambda$. The tensile stress history at all other points is the same as at $\frac{1}{2}\lambda$.

The preceding examples are oversimplifications of the response of real materials in this type of experiment, but they provide an insight into more complex situations. The stress histories and stress distributions in these examples indicate that there are a variety of possible load histories leading to failure and suggest that multiple fracture is likely to occur in some cases. Experiments in which only one fracture occurs are desirable because interpretations of them are much more straightforward. The type of load to failure and the likelihood of

multiple fracture depends on the magnitude of the preload in relation to the tensile strength and the rate dependence of the tensile properties of the rod. In experiments with a preload that is only slightly higher than that required to produce dynamic failure during the rise of the tensile stress, the width of the region that first reaches the critical stress is minimized and so is the likelihood of multiple fracture.

3. Experimental method

Apparatus

Figure 6 shows a photograph of the apparatus developed to perform experiments of the type just discussed. This apparatus tests 5.1 cm-diameter, 76.2 cm-long rods at stresses up to 20 MPa. The static end pressure is removed in about 30 μ s, producing unloading strain rates in concrete of about 10/s.

The essential component of the tensile testing apparatus is the unloading device at each end of the rod. Its design is shown in Fig. 7. It consists of a bored aluminum block into which the end of a rod specimen and a plastic piston fit to form a chamber for oil. The oil is pressurized by means of a small orifice through the wall of the bore block. The rod and piston seal the pressurized oil in the chamber with rubber O-rings. The piston is held in place by a thin-walled steel support tube, which presses against a reaction plate bolted to the block.

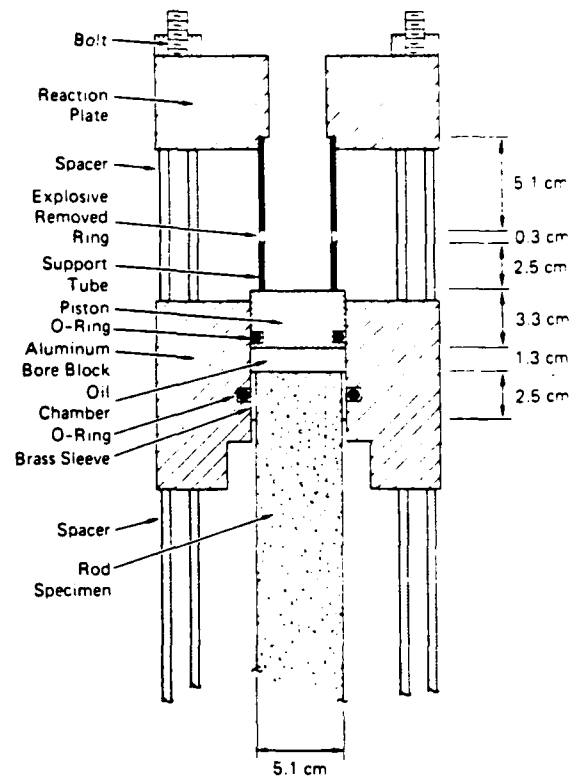


Fig. 7. Unloading device.

The support tube comprises three sections, one of which is a segmented ring that is explosively driven inward to free the piston and initiate decompression of the oil. The rod is held in place by an identical unit at the other end, with the two blocks bolted together.

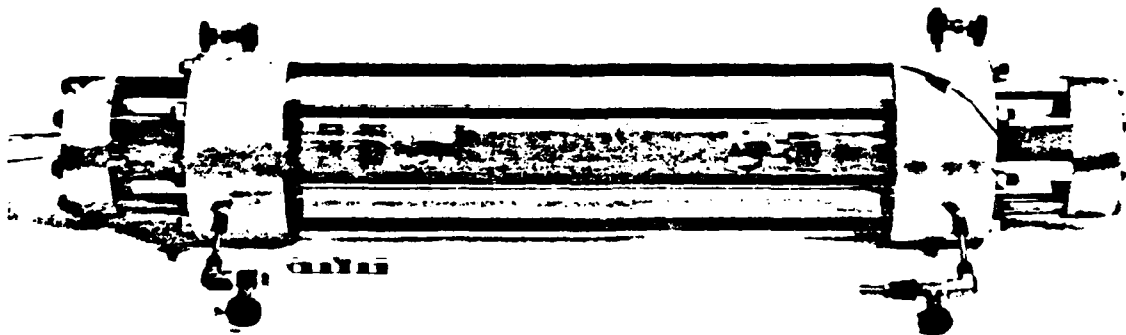


Fig. 6. Dynamic tension testing apparatus with an unconfined concrete rod.

The rings in the support tubes are removed with an estimated simultaneity of less than $5\ \mu\text{s}$ using strands of sheet explosive. The explosive produces no damage to the apparatus except to the rings, and allows a smooth decay of pressure in the oil chamber. Occasionally a small compressive precursor is produced by the explosive pressure.

In experiments without confinement, a Plexiglas tube is used to space the two unloading devices, as shown in Fig. 6. In experiments with confinement, a 7.6 cm-ID aluminum tube is used to hold the confining pressure and to space the unloading devices. The confining pressure remains approximately constant during an experiment, but it is perturbed slightly by the radial motion of the rod produced by the stress waves.

Measurements

The pressure in the chamber at each end of the rod and in the confining pressure chamber surrounding the rod were measured as a function of time. The measurements were made with commercially available diaphragm-type pressure gages (Kulite HKS-375).

Examples of typical transient pressure histories are shown in Fig. 8. Figures 8(a) and 8(b) show that in this experiment the axial unloading occurred in about $25\ \mu\text{s}$ and was simultaneous at the two ends. The radial pressure, shown in Fig. 8(c), was constant until the stress waves in the rod reached the gage location (midpoint of the rod), and remained within 1 MPa of the initial value. The variation in radial pressure appears to follow the circumferential strain (not shown), suggesting that the pressure variation is caused by volume changes in the specimen, produced by the Poisson effect as the axial stress wave propagates along the rod. This result shows that a one-dimensional wave analysis is not rigorously correct for these experiments because the radial stress is coupled to the axial stress.

Axial and circumferential strains were measured at several axial locations on the surface of the rod, using commercially available 2.5 cm-long foil-type strain gages (Micromeritics MM-EA-06-10CBE-120). This length of strain gage re-

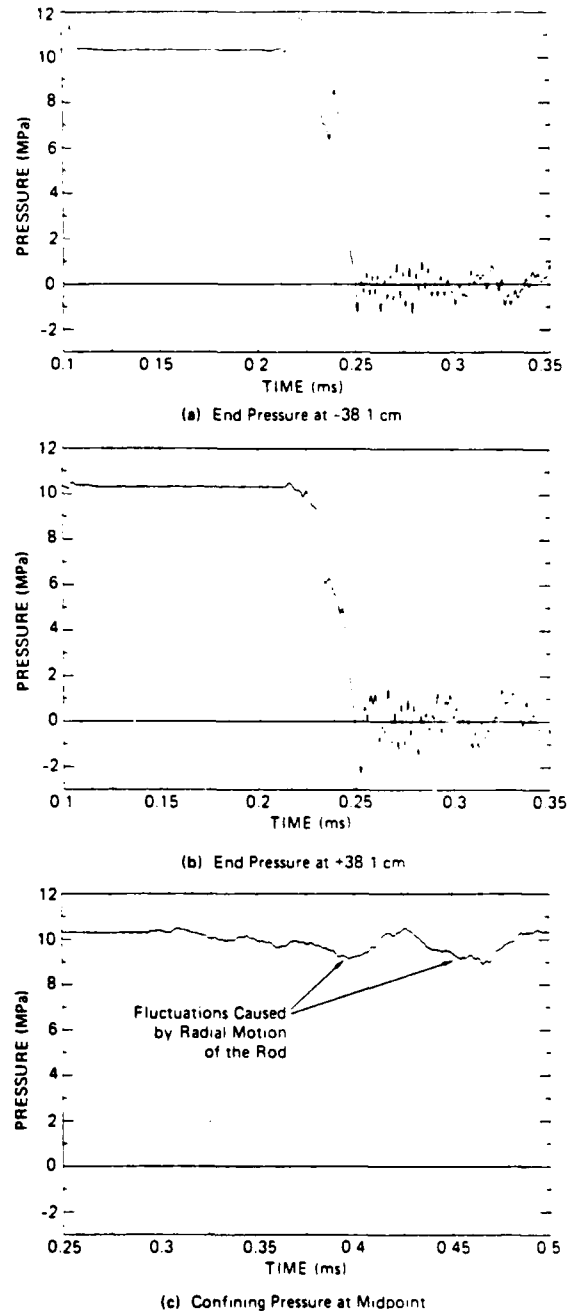


Fig. 8. Pressure measurements in experiment 3 (10.31 hydrostatic preload).

sults in considerable averaging of strain but, for an inhomogeneous material such as concrete, the averaging is necessary. Each measurement was

made by averaging the outputs from three gages mounted on 120 degree intervals at the same axial position. Averaging these three measurements eliminates bending contributions to the strain caused by small curvature in the rods. Axial strain was measured at four locations: 10 cm from each end of the rod and 7.6 cm from the midpoint on both halves of the rod. Circumferential strain was measured at only the symmetric points 7.6 cm from the midpoint.

Concrete rod specimens

The concrete tested in the current work was made from graded aggregate, Portland cement, and water. The aggregate was local river rock with rounded shapes, meeting the ASTM C33 specification for size distribution. It was sieved to remove all aggregates not passing a 0.635 cm ($\frac{1}{4}$ inch) opening. The average static compressive strength was about 60 MPa, and the average splitting tensile strength was about 3.4 MPa. The average elastic modulus was 25 MPa, and Poisson's ratio was 0.2.

The rods were cast about 90 cm long, and then trimmed to 76.2 cm. Brass sleeves, measuring 2.5 cm long and 0.04 cm in thickness, were epoxied on to the rods at each end. These sleeves were the sealing surfaces for the O-rings in the testing apparatus.

4. Results

The four experiments described in this paper are listed in Table 1. In all of the experiments the strain rate in the front of the rarefaction waves was about 10/s, so the strain rate in the region of superposition of the waves was about 20/s. Usually a single fracture occurred near the midpoint of the rod. In some experiments multiple fractures occurred. Based on measurements of axial strains on the concrete rods, the observed strength enhancement at this strain rate was considerable.

Experiments on unconfined rods

Experiments 1 and 2 were performed on concrete rods with no confinement and a static axial

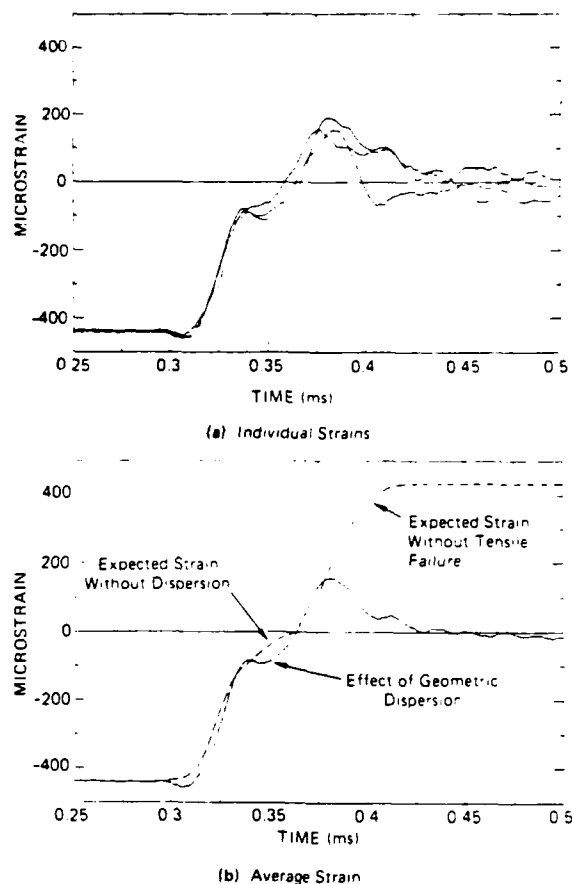


Fig. 9. Axial strain records at ± 7.6 cm (7.1 cm from fracture location) in experiment 1 (10.55 MPa uniaxial preload).

preload of 10.55 MPa. Both rods failed in dynamic tension at a single location within 0.5 cm from the midpoint, and no secondary damage was visible.

The axial strain histories from Experiment 1 measured at the ± 7.6 cm locations (referenced from the midpoint of the rod) are shown in Figs. 9 and 10. Some of the effects of inhomogeneity in the specimen were eliminated by scaling the recorded strain signals to make the initial strains (from the static preload) at each location equal to the average of all the initial strains. On the time scale of these plots, the explosive charge was initiated at $t = 0.100$ ms. Geometric dispersion in the rarefaction waves as they propagate from the ends of the rod to these locations causes the oscillation

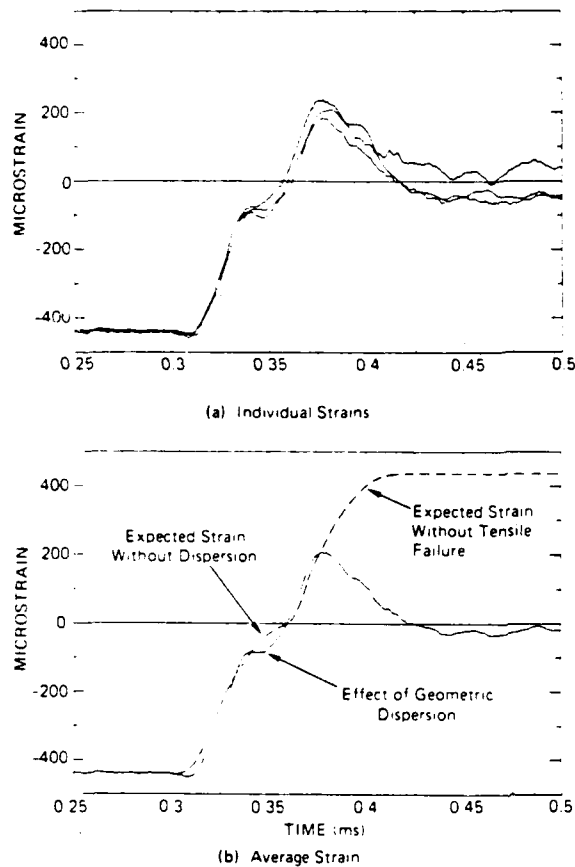


Fig. 10. Axial strain records at 7.6 cm (8.1 cm from fracture location) in experiment 1 (10.55 MPa uniaxial preload).

in the strain records just before the arrival of the second wave. The strain rate at the front of the rarefaction waves was about 10/s, so the strain rate at the failure location was about 20/s.

The axial strains show the effect of tensile failure at about $t = 0.380$ ms, when the tensile strains reach a peak and no longer follow the history expected for elastic response. The three individual strains at both locations are fairly uniform even after the effects of tensile failure arrive. After fracture, the stress waves propagate and reflect in the two separated half-rods with stress-free ends. However, reflections do not return to these locations during the time period shown in these figures.

The peak average strain at -7.6 cm (7.1 cm from the failure location) was 160 microstrain.

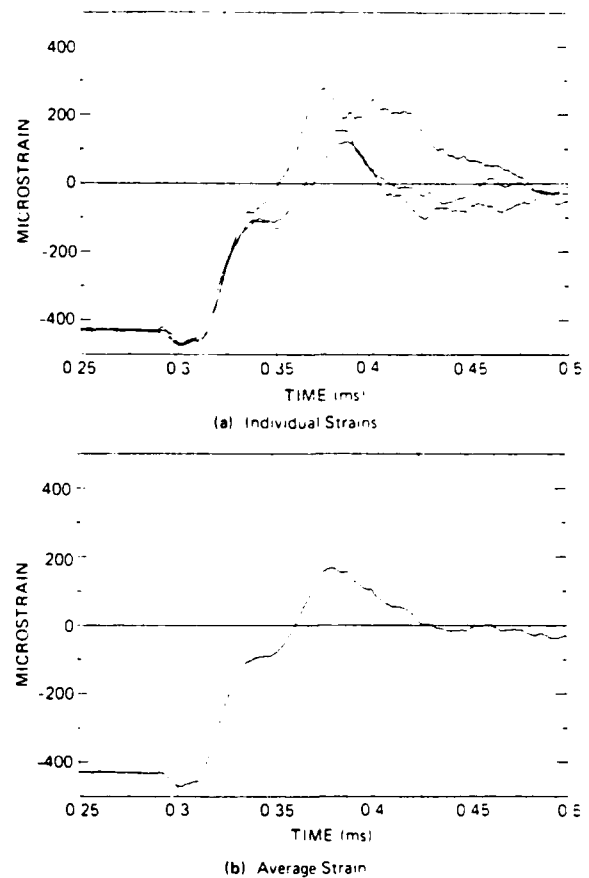


Fig. 11. Axial strain records at -7.6 cm (7.5 cm from fracture location) in experiment 2 (10.55 MPa uniaxial preload.)

The peak average strain at $+7.6$ cm (8.1 cm from the failure location) was 210 microstrain. Assuming linear elastic response at the gage locations and using the static elastic constants for the concrete, the higher of these measurements corresponds to an axial stress of about 5 MPa, nearly 50% higher than the average static splitting tensile strength for this family of rods.

The axial strains measured in Experiment 2 at ± 7.6 cm are shown in Figs. 11 and 12. The individual strains show wider variations than those in Experiment 1, especially after the effects of tensile failure arrive. However the average strains are very nearly the same as those in the previous experiment. The peak average strain at -7.6 cm (7.5 cm from the failure location) was 170 microstrain, and at $+7.6$ cm (7.7 cm from the failure

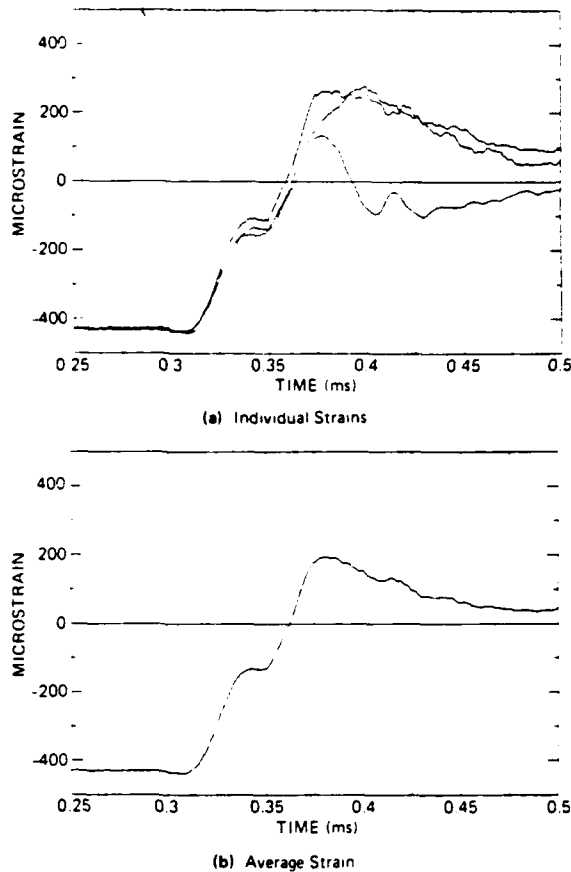


Fig. 12. Axial strain records at 7.6 cm (7.7 cm from fracture location) in experiment 2 (10.55 MPa uniaxial preload.)

location) it was 190 microstrain. The elastic axial stress corresponding to the highest measured strain is about 4.7 MPa, about 40% higher than the average static splitting tensile strength for this family of rods.

For a material like concrete, the waveforms and peak strains measured in Experiments 1 and 2 demonstrate very good reproducibility of the results. It is recognized, however, that the 40–50% estimated strength enhancement is much less than the 400% enhancement reported by Birkimer (1968) for these strain rates. This contrast may simply reflect the differences between the materials tested. It may also be associated with the assumption of elastic strains. (If the measured strains were inelastic, the estimates of strength

would be high in both cases but not necessarily by the same amount.)

Experiments on confined rods

Experiments 3 and 4 were performed on concrete rods with hydrostatic preloads of 10.31 MPa and 10.20 MPa, respectively. The rod in Experiment 3 failed in dynamic tension at two locations, +2.2 cm and -15.2 cm. No large voids existed at either section. The rod in Experiment 4 failed only at -3.8 cm. One fairly large void (0.8 cm diameter) was evident at the failed section.

Plots of the average axial strains at ± 7.6 cm in Experiment 3 are shown in Fig. 13. The axial

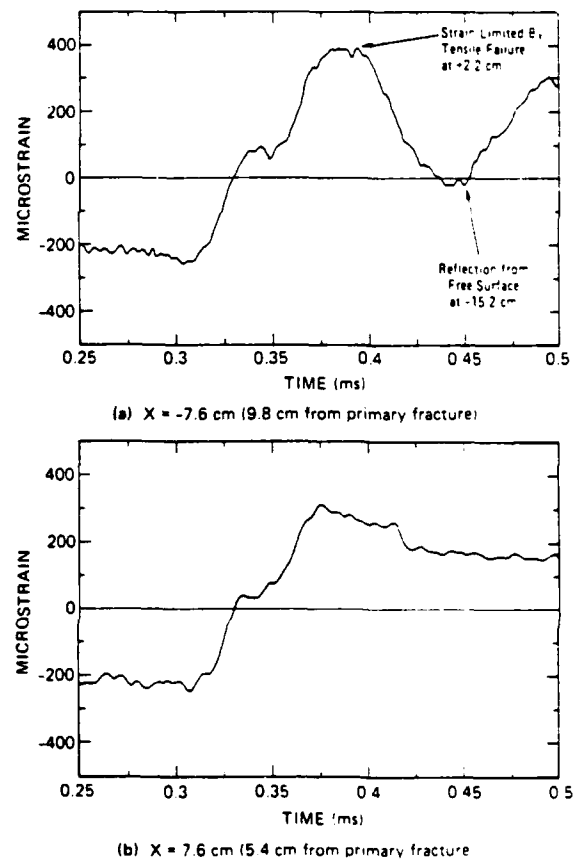


Fig. 13. Average axial strains at ± 7.6 cm in experiment 3 (10.31 MPa hydrostatic preload).

Table 1
Dynamic tension experiments on concrete rods

Experiment number ¹	Axial preload (MPa)	Radial preload (MPa)	Elastic modulus ² (GPa)	Dynamic tensile strength ³ (MPa)	Fracture locations (cm from midpoint)
1	10.55	0.0	24.1	5.0	+0.46
2	10.55	0.0	24.7	4.7	+0.10
3	10.31	10.31	28.4	6.9	-15.2, +2.2
4	10.20	10.20	23.0	6.7	-3.8

¹ These experiments were originally titled Test 42, 43, 44, and 46, respectively (Gran, 1985).

² The elastic constants were determined from the static preload and the average initial strains.

³ These are estimates corresponding to the elastic stresses computed from the peak measured tensile strains.

strain corresponding to zero axial stress is 145 microstrain. The failure at +2.2 cm produced the drop in axial strains at ± 7.6 cm at about $t = 0.380$ ms. The fracture at -15.2 cm produced a new free surface there, and the rarefaction wave reflected from this section and returned to the strain gages at -7.6 cm. The other half of the rod remained intact, so no reflections from the end of the rod returned during this period.

The peak average strain at -7.6 cm was 390 microstrain. At +7.6 cm it was 315 microstrain. Again assuming linear elastic response at the gage locations, using the elastic modulus given in Table 1, and accounting for the nominal radial stress of 10.20 MPa, these axial strains correspond to axial stresses of about 6.9 MPa and 5.6 MPa, respectively. The higher of these stresses is about 100% greater than the average static splitting tensile strength for this family of rods. It is also about

40% higher than the unconfined tensile strength at the same strain rate, observed in Experiments 1 and 2.

In Experiment 4, the unloading device at one end did not perform properly. The pressure dropped smoothly in about 30 μ s, but it remained at zero for only about 50 μ s before recompression occurred. Posttest inspection of the unloading device at this end showed that the segmented ring was only partially removed by the explosive and was trapped between the support tube and the spacer. Apparently, this limited the travel of the piston so that the extension of the rod recompressed the oil. In addition to this problem, the strain gages at +7.6 cm did not function.

The axial strain measured at -7.6 cm in Experiment 4 is shown in Fig. 14. The wavefront of the first rarefaction shows a longer rise time than was typical of the waves in previous experiments, possibly because of the malfunction of the unloading device. However, after the arrival of the second rarefaction wave (beginning at about $t = 0.365$ ms), the tensile strain rate is about the same as in Experiment 3. The peak axial strain is 470 microstrain, corresponding to an elastic axial stress of 6.7 MPa. This is about the same as that computed from the strains in Experiment 3 (the elastic moduli were significantly different).

Thus, although there were difficulties with multiple fracture, malfunctions of the unloading device, and loss of some strain records, Experiments 3 and 4 demonstrated the capability of the experimental technique to produce tensile failure at a strain rate of 10 to 20/s with independently controlled confining pressure. The surprising result that the apparent dynamic tensile strength is

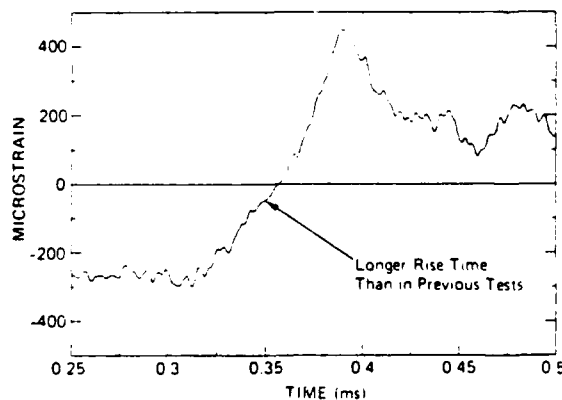


Fig. 14. Average axial strain at -7.6 cm (3.8 cm from fracture) in experiment 4 (10.31 MPa hydrostatic preload.)

enhanced by the confinement is in contrast to static data, e.g. (Saucier, 1974), but no other dynamic data are available for comparison.

5. Interpretation of the results

Assuming the peak observed strains in these experiments to be elastic, the unconfined tensile strength of the concrete at a strain rate of 10 to 20/s averaged over 40% higher than the static splitting tensile strength. At the same strain rate, the tensile strength with 10 MPa confining pressure was, on average, about 100% higher than the static splitting tensile strength, and about 40% higher than the unconfined tensile strength at 10 to 20/s.

These strength estimates are based on the assumption that the measured strains are elastic, but this assumption may not be justified. Thus, to further interpret the experimental results wave-propagation calculations were performed using a one-dimensional strain-softening model (Gran, 1985). The model is based on the assumption that the stress-strain relation is not a property of a material point, but is an average property of a finite volume of material containing a developing crack or failure plane. The stress-strain relation thus has associated with it a finite dimension, namely the average crack separation distance. Using this model, the two dynamic unconfined tension experiments were simulated, and by trial-and-error good agreement with the measured strains was obtained in both cases.

Whereas the dynamic experiments produced a single fracture plane with no visible secondary damage, the calculations predicted some inelastic strain to occur virtually throughout the specimen, with concentrations of inelastic strain within a few centimeters of the locations of complete fracture. In addition, the calculations suggest that the strain history measured a few centimeters from the location of fracture is primarily a function of inelastic wave propagation from the fracture location to the strain gage (through the sites of concentrated inelastic strain), and is less dependent on the behavior of the material right at the fracture. However, they also showed that the strains were measured at

locations where the inelasticity was slight, so that in this case the estimates of strength are reasonable. The nonlinear analyses performed by Gran (1985) will be described in a subsequent paper.

Even without nonlinear analyses, however, these experiments show that the assumption of elastic response everywhere except at the failure location is not valid, even when only one section was visibly damaged. According to that assumption, as depicted in Fig. 4, the observed peak strain should be $\frac{1}{2}(1 + \alpha)$ times the prestrain, where α is the ratio of the strength to the preload. That is, the observed peak strain should never be less than half the prestrain, even when the strength-to-preload ratio is zero. (The measurements need to be made at distances greater than $\frac{1}{4}\lambda(1 - \alpha)$ from the failure location in order to not be limited by residual pre-compression.) The observed peak strains in the unconfined experiment were all less than half the prestrain, and the measurement locations were well outside the region where the strain would be limited by residual precompression.

Similarly, in the confined experiments the peak observed strains at ± 7.6 cm would correspond to stresses equal to $\frac{1}{2}(1 + \alpha)\sigma_0$. For peak stresses of, say, 6.8 MPa (computed from the peak measured strains) and an initial preload of 10 MPa, α would be 0.36. The strength at the failure location, given by $\alpha\sigma_0$, would only be 3.6 MPa, or about half the peak stress occurring remote from the failure location as estimated from measured strains.

Thus, estimates of tensile strength based on elastic wave analyses are, in general, not valid for this type of experiment.

6. Summary and conclusions

An experimental technique to measure the tensile response of brittle geologic solids at strain rates of approximately 10 to 20/s was developed and applied to concrete rod specimens. In all of the experiments the primary failure location occurred within a few centimeters of the midpoint of the rod. In some of the experiments a second failure occurred near one quarter-point. Successful measurements were made of the applied pressures

and the surface strains. The effects of tensile failure on the stress waves in the specimen were observed in the surface strain measurements.

The initial results appear to be sufficiently reproducible to warrant a fairly detailed interpretation. The input waveforms, measured at ± 7.6 cm from the midpoint of the rod, are nearly identical from test to test. For similar initial conditions, the average axial strain measurements after fracture are also very similar in form and magnitude.

In general, the experimental results require a nonlinear analysis for proper interpretation. However, for the particular experiments described here, a simple elastic interpretation of peak strains gives reasonable estimates for tensile strength because the inelastic strains at the measurement locations are not large. This simple interpretation indicates that there is about a 40% increase in the tensile strength of this particular concrete at a strain rate of 10 to 20/s, compared to the static splitting strength. The data also indicate that there is an additional 40% increase of the dynamic tensile strength with a static confining pressure of 10 MPa. However, these estimates are only approximate because inelastic response in the specimen is not included in this interpretation.

Clearly, more experiments and interpretive analyses are needed to even empirically characterize the tensile failure of concrete at these strain rates. In addition, the application of the experimental method to brittle geologic materials, particularly fine-grained rocks, is an obvious future direction. Coupled with nonlinear wave propagation analyses, this experimental method should provide unique and valuable data for the development of rate-dependent tensile failure models for these materials.

Acknowledgments

This work was sponsored by the U.S. Air Force Office of Scientific Research under Contract

F49620-82-K-0021, and was submitted by the first author as partial fulfillment of the requirements for the degree of Doctor of Philosophy. The technical assistance of T. Lovelace, F. Galimba, G. Cartwright, W. Heckman, and B. Bain is gratefully acknowledged.

References

- Abbott, B.W. and R.H. Cornish (1965), "A stress-wave technique for determining tensile strength of brittle materials", *Experimental Mechanics*.
- Berg, P.W. and J.L. McGregor (1966), *Elementary Partial Differential Equations*, Holden-Day, San Francisco.
- Birkimer, D.L. (1968), "Critical normal fracture strain of portland cement concrete", Doctoral Thesis, Department of Civil Engineering, University of Cincinnati, Cincinnati.
- Felix, M.P. (1977), "Determination of stress levels for dynamic fracture of oil shale", *Experimental Mechanics*.
- Goldsmith, W., V.H. Kenner, and T.E. Richetts (1968), "Dynamic loading of several concrete-like mixtures", *ASCE J. Struct. Div.* 94 (7).
- Grady, D.E. and M.E. Kipp (1979), "The micromechanics of impact fracture of rock", *Internat. J. Rock Mech., Min. Sci. Geomech.* 16.
- Gran, J.K. (1985), "Development of an experimental technique and related analyses to study the dynamic tensile failure of concrete", Doctoral Thesis, Division of Applied Mechanics, Stanford University, Stanford, CA.
- Gupta, Y.M. and L. Seaman (1979), "Local response of reinforced concrete to missile impact", Final Report NP-1217, Electric Power Research Institute, Palo Alto, CA.
- Kipp, M.E., D.E. Grady and E.P. Chen (1980), "Strain-rate dependent fracture initiation", *Internat. J. Fracture* 16 (5) 471-478.
- Reinhardt, H.W. (1985), "Tensile fracture of concrete at high rates of loading", in: S.P. Shah, ed., *Application of Fracture Mechanics to Cementitious Composites*, Martinus Nijhoff, Dordrecht.
- Saucier, K.L. (1974), "Equipment and test procedures for determining multiaxial tensile and combined tensile-compressive strength of concrete", Technical Report C-74-1, U.S. Army Corps of Engineers Waterways Experiment Station, Vicksburg, MS.

APPENDIX B

Reference:

J. K. Gran and L. Seaman, "Strain-Softening Calculations for Concrete in Dynamic Uniaxial Tension," ASCE Journal of Engineering Mechanics (in press).

STRAIN-SOFTENING CALCULATIONS FOR CONCRETE IN DYNAMIC UNIAXIAL TENSION

By James K. Gran¹ and Lynn Seaman², M.ASCE

ABSTRACT: A one-dimensional strain-softening model was used in wave-propagation calculations to interpret dynamic unconfined tension experiments on concrete rods. The model is based on the assumption that the stress-strain relation is not a property of a material point, but is an average property of a finite volume of material containing a developing crack or failure plane. The stress-strain relation has associated with it a finite dimension, namely an effective crack separation distance. Two experiments were simulated, and with suitable choice of the material parameters good agreement with the measured axial strain histories was obtained in both cases. In addition to providing an estimate of the dynamic tensile properties of the concrete, these calculations suggest that tensile damage in the concrete was distributed over several centimeters surrounding the location of fracture. The strain history measured a few centimeters from the fracture appears to be primarily a function of inelastic wave propagation from the fracture to the strain gage, and is only weakly dependent on the behavior of the material at the location of complete fracture.

SUMMARY: A one-dimensional strain-softening model was used in wave-propagation calculations to interpret results of dynamic tension experiments on concrete rods. Two dynamic unconfined tension experiments were simulated, and good agreement with the measured axial strain histories was obtained in both cases.

KEY WORDS: strain-softening, calculations, concrete, dynamic, tension, fracture, cracking, damage

¹Research Engineer, Poulter Laboratory, SRI International, Menlo Park, CA 94025, (415)859-4472

²Senior Research Engineer, Poulter Laboratory, SRI International, Menlo Park, CA 94025, (415)859-3587

INTRODUCTION

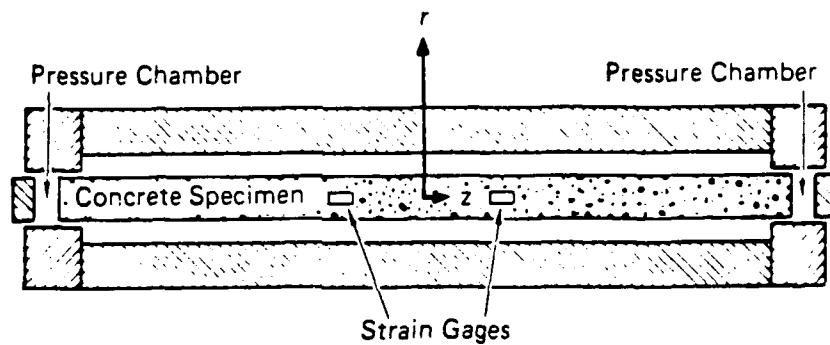
Tensile failure in concrete and brittle geologic materials results from the growth and coalescence of tensile microcracks with a corresponding loss of tensile strength. The understanding and quantification of this failure process are currently not sufficient to provide a detailed micromechanical model. This situation prompts the use of so-called continuum strain-softening models in numerical simulations of tensile failure. These models allow decreasing stress with increasing strain by averaging over a finite region the deformation associated with cracking.

Some notable examples of continuum strain-softening models that have been utilized successfully to describe quasi-static experimental behavior are the line crack model introduced by Hillerborg, et al (1976), the crack band model of Bazant and Oh (1983), and the composite fracture model developed by Willam, et al (1984). As pointed out by Ottosen (1986), each of these models has the necessary feature that a fundamental relationship between stress and displacement across a softening zone is preserved as the size of the numerical cell containing the softening zone is varied. Bazant (1976) concluded that the proper size of the softening cell must be determined experimentally.

Recently, the proper construction and use of strain-softening models for dynamic problems has been a topic of considerable interest. Sandler and Wright (1984) demonstrated with numerical and analytical examples that any attempt to model uniform deformation in a rate-independent strain-softening continuum will always result in an unbounded strain concentration. Belytschko and Bazant (1984) also used numerical and analytical examples to show that for a given stress-strain relation with softening, the calculated work done to fail the material is cell-size dependent. Furthermore, as the cell size tends to zero, the work also tends to zero, which is certainly not a physically plausible result. Both of these studies considered only softening continua, that is, rather than preserving a stress-displacement relationship across a softening zone, these models preserve a stress-strain relationship as the size of the cell is varied. A conclusion of both studies is that such a model is physically implausible.

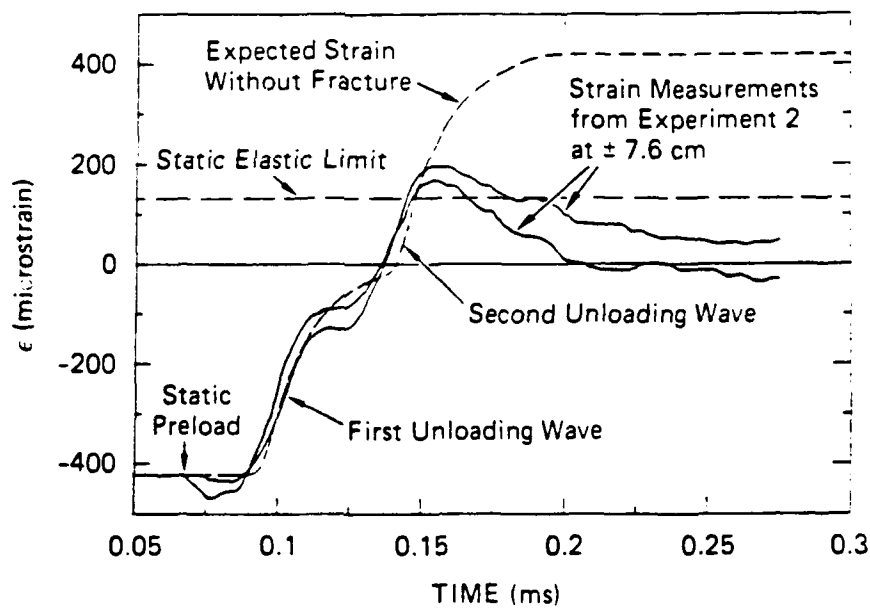
This paper describes an attempt to apply a one-dimensional model of the Hillerborg-Bazant-Willam type to a dynamic problem, and to assess the ability of the model to reproduce dynamic experimental observations. We assume that the physical source of strain softening is tensile cracking, that the deformation is naturally concentrated at the cracks, and that the stress versus crack-opening relation is a fundamental property of the material. In addition, we assume that the softening stress-strain relation is not a property of a material point, but is an average property of a finite volume of material containing a developing crack or failure plane. The stress-strain relation thus has associated with it a characteristic finite dimension, namely the effective crack separation distance.

The strain-softening calculations described here were guided by experiments performed by Gran et al (1987), whose experimental technique is illustrated in Figure 1. With



JA-314583-11B

Figure 1. Dynamic tensile loading technique.



JA-4451-71B

Figure 2. Typical axial strain records from a dynamic tension experiment.

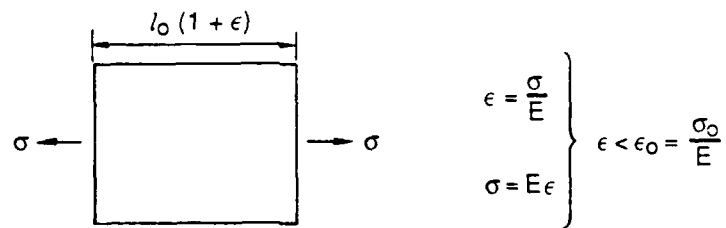
this technique a cylindrical concrete rod specimen is first loaded in static uniaxial compression, then the axial load is released from each end simultaneously and very rapidly. The resulting relief waves interact in the center of the rod to produce a dynamic tensile stress equal in magnitude to the original static compression at a strain rate of 10/s to 20/s. Typically in these experiments, a single complete fracture across the rod occurs near the midpoint of the rod. Transient measurements are made of the axial load at each end of the rod and of axial and circumferential surface strains at several locations along the length of the rod. An example of axial strain measurements from a typical experiment is shown in Figure 2. The static compressive preload in this experiment was 10 MPa; the nominal static tensile strength of the concrete was 3.4 MPa. The strains shown in Figure 2 were measured at symmetric locations 7.62 cm from the midpoint of the rod using three 2.54-cm-long strain gages at each location. A single complete fracture across the rod occurred at 0.1 cm from the midpoint of the rod, but no other macroscopic tensile damage was visible.

These experimental results do not give directly the strength of the concrete or the strength reduction as a function of accumulating tensile damage. Thus, the objective of the calculations described in this paper is to estimate for these experiments the tensile strength and the strength reduction as a function of accumulating damage exhibited by pertinent regions of the concrete specimens. The analyses were performed by numerically integrating the governing equations for stress waves in the rod, using an assumed strain-softening response. By comparing the computed strain histories with the measurements from the experiments, the assumed strain-softening response was adjusted to give good correlation with the observations. Although this exercise does not produce a unique constitutive model for concrete tensile failure, it does provide insight into the dynamic tensile failure of concrete by making an estimate of what must have happened in the neighborhood of the complete fracture location--a part of the response that cannot be measured directly.

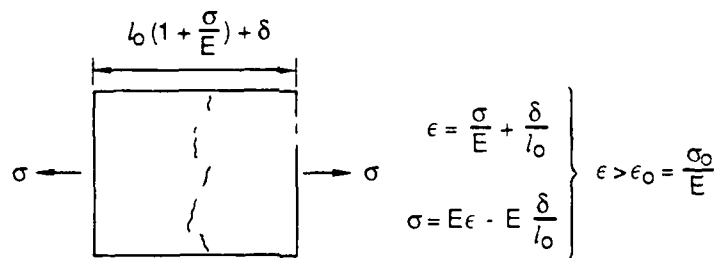
FORMULATION OF THE STRAIN-SOFTENING MODEL

Our approach is to assume that the rod comprises a single row of one-dimensional material cells, each containing a single potential fracture plane (crack). The analytical model used for tensile failure is simply a prescribed relation between the stress in a cell and the fracture volume per unit area (crack opening) created during the failure process. A pictorial representation of the assumed failure process is shown in Figure 3. The material is initially elastic with modulus E , that of intact material. Fracture volume per unit area (δ) is created only after the stress reaches the tensile strength (σ_0). Then under continued tensile strain, the fracture volume per unit area increases to a critical value (δ_c) as the strength is reduced to zero, resulting in complete fracture. Note that δ has the units of displacement and can be regarded as an effective crack opening. The relation between σ and δ (for loading and unloading) is a basic property.

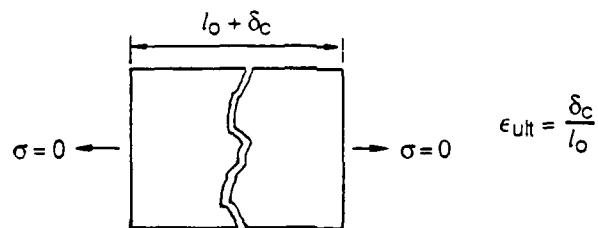
The initial length of the material cell is l_0 . This is a characteristic dimension of the material and can be regarded as an effective crack spacing in this one-dimensional



(a) Elastic straining up to critical stress σ_0 .



(b) Growth of fracture Volume per unit area (δ).



(c) Tensile failure at $\delta = \delta_c$.

JA-4451-68B

Figure 3. Concept of the one-dimensional tensile failure model.

formulation. The source of the effective crack spacing may be the distribution of aggregate grains as crack nucleation sites. Another source of effective crack spacing could be stress-wave interactions that permit the growth of only those cracks that are sufficiently separated, as suggested by the work of Kipp and Grady (1985).

An example of a relation between σ and δ is shown in Figure 4(a) as $\sigma(\delta)$. In this example, the strength shows no increase beyond the initial strength and decays to zero linearly. Unloading and reloading follow a straight line leading to and from the origin, implying that some of the work expended in creating the fracture is recoverable. As shown in Figure 4(b), the strain value corresponding to complete separation depends on the original dimensions of the fracturing cell. That is, for a given relation between stress and fracture volume per unit area, the relation between stress and strain depends on the crack spacing (cell size) assumed in the numerical discretization.

As mentioned above, when implemented as a stress-strain relation, this model is essentially the same as those described by Hillerborg, et al (1976), Bazant (1976), and Willem, et al (1984). In the softening regime ($\epsilon > \sigma_0/E$), the fracture volume per unit area is $\delta = (\epsilon - \sigma_0/E)l_0$. In general, the stress reduction is given by $\sigma(\delta)$, and the stress-strain relation is obtained by inserting the expression for δ and solving for $\sigma(\epsilon)$. For the special case of linear stress reduction shown in Figure 4 the softening stress-strain relation is

$$\sigma = E \frac{\epsilon_0}{\epsilon_{ult} - \epsilon_0} (\epsilon_{ult} - \epsilon) \quad (1)$$

which depends on l_0 through the definition of $\epsilon_{ult} = \delta_c/l_0$. An explicit expression for δ in terms of ϵ is then

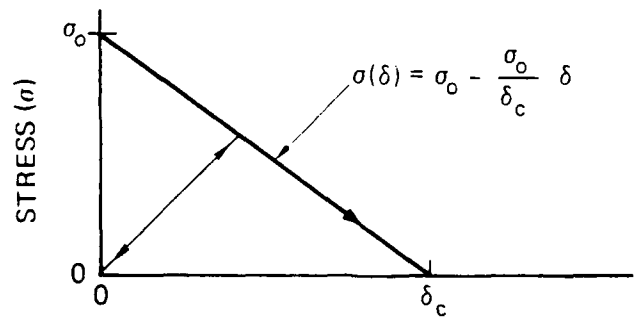
$$\delta = l_0 \frac{\epsilon_{ult}}{\epsilon_{ult} - \epsilon_0} (\epsilon - \epsilon_0) \quad (2)$$

To summarize, the tensile failure model is defined by the elastic modulus E , the strength σ_0 , the relation between stress and fracture volume per unit area $\sigma(\delta)$, and the effective crack spacing l_0 .

Even though the stress-strain relation depends on the cell size, the work done per unit area to completely fracture a cell is independent of the cell size because all the work goes into creating the fracture, and the elastic material returns to a state of zero internal energy. For linear softening the work done per unit area to completely fracture a cell is $G_c = \sigma_0 \delta_c/2$. Thus, the work done per unit area to completely fracture a cell depends only on the critical stress and the critical fracture volume per unit area, and does not depend on the cell size.

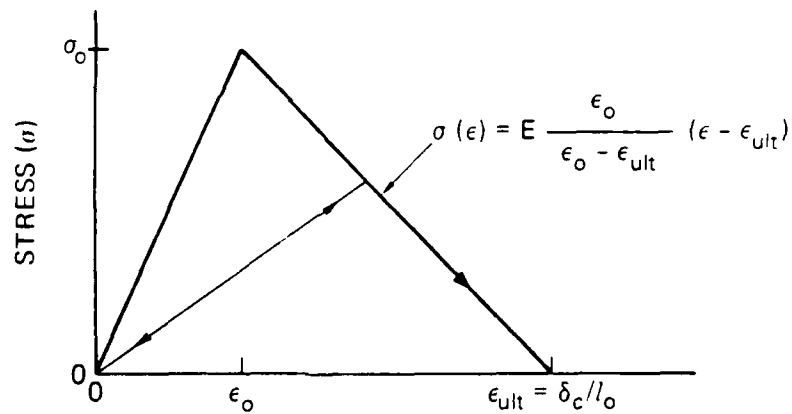
However, if a cell is only partially damaged, that is strained to ϵ_{max} , where $\epsilon_{max} < \epsilon_{ult}$, then the unrecovered work per unit area for linear unloading to the origin is

$$G' = \frac{1}{2} \sigma_0 \delta_c \frac{(\epsilon_{max} - \epsilon_0)}{(\epsilon_{ult} - \epsilon_0)} \quad (3)$$



FRACTURE VOLUME PER UNIT AREA (δ)

(a) Stress Versus Fracture Volume per Unit Area



STRAIN (ϵ)

(b) Stress Versus Strain

JA-4451-69A

Figure 4. Implementation of the tensile failure model as a strain-softening model.

which depends on l_0 through ϵ_{ult} . This dependence occurs because for a given maximum strain the maximum fracture volume per unit area (crack opening) depends on the cell size (crack spacing), as given in equation (2).

It should be expected, therefore, that strains calculated with this model in wave-propagation analyses will depend on the cell size (crack spacing) chosen for the calculation. Indeed, because the cell size represents an allowed crack spacing, it is a material parameter that must be determined. This crack spacing is similar to the crack band width w_c , considered by Bazant and Oh (1983). Consequently, as part of the parameter study with the tensile failure model, a study was made of cell size dependence. Ottosen's (1986) restriction on cell size, namely that $l_0 < 2G_c E / \sigma_0^2$, is satisfied by requiring that $\epsilon_{ult} > \epsilon_0$.

Finally, we point out that the model for the failure process used here is not rate dependent. Although we believe the true response to be rate dependent, the range of strain rates in the experiments under study is not more than a factor of 2 (10/s to 20/s). Thus, as a simplification, rate dependence has not been included explicitly, although the parameters chosen by trial and error to match the experimental results define our estimate of the material behavior at strain rates of 10/s to 20/s.

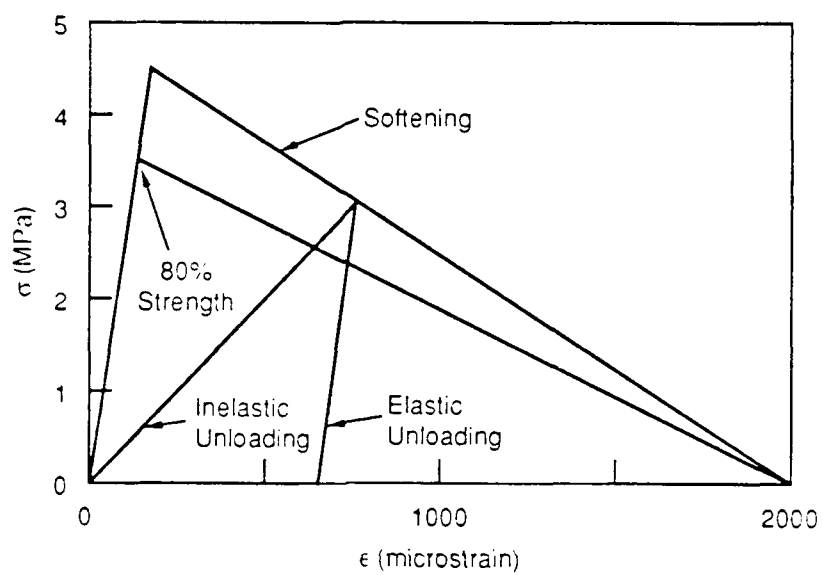
PARAMETER STUDY

Several one-dimensional stress wave-propagation calculations were performed using a finite-difference scheme (Seaman, 1978) to integrate the governing equations. These calculations illustrate the sensitivity of the numerical results to the parameters defining the assumed strain-softening properties. In one set of calculations, the properties of the material at the location of complete fracture were varied while the properties in the rest of the rod remained fixed. This set of calculations establishes requirements for controlling the location of complete fracture. In another set of calculations, the unloading modulus was varied to determine its effect on calculated strain histories. In a third set of calculations, the cell size was varied as the $\sigma(\delta)$ relation remained fixed. These sets of calculations demonstrate the qualitative nature of the model.

The correlation of the predictions with the experimental results was made by comparing the calculated axial strains with the measurements made in an experiment by Gran, et al (1987). The strain histories from the selected experiment were shown in Figure 2. The peak strain (measured 7.7 cm from the location of complete fracture) was 190 microstrain, which, if elastic, would correspond to an axial stress of about 4.7 MPa (40% greater than the static strength). In each calculation, a static preload of 10.20 MPa was applied at each end of the rod, and removed with an exponential decay with a time constant of 15 μ s.

Variation of the Properties at the Location of Complete Fracture

In Calculation A every cell in the rod was given the property shown in Figure 5(a)



RA-314522-39

Figure 5. Stress-strain relations used in the parameter study of the tensile failure model.

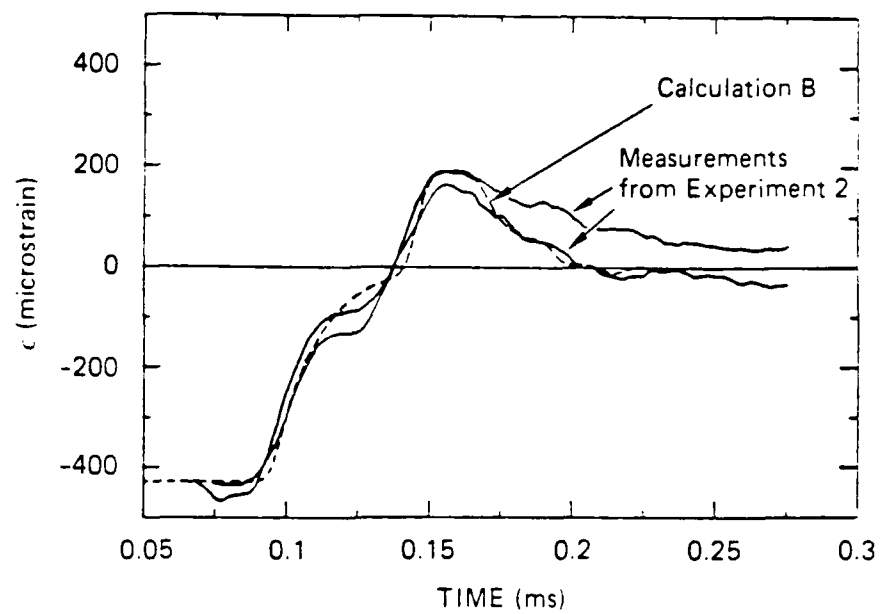
labeled "Softening". The cell width was 0.333 cm and the fracture volume per unit area at complete separation was about $7\mu\text{m}$. The predicted stress and strain histories for this calculation are not shown because a single complete fracture at the origin did not occur, making a comparison with the experimental results meaningless. Complete fracture was computed to occur at four locations, 0.66 cm and 3.33 cm from the origin in both halves of the rod. A segment of the rod about 4 cm long had a fairly uniform stress distribution at the time the assumed strength was first reached. Apparently, numerical perturbations in the unloading waveform caused the stress to first exceed the strength at a point other than the origin.

This result demonstrates that if all the cells have the same strength and the same strain-softening relation, the calculated location of complete fracture is determined by numerical perturbations in the load. It also implies that experiments in which the loading is presumably symmetric, but in which complete fracture occurs at an asymmetric location (a likely occurrence) cannot be correctly represented with uniform properties along the length of the rod. However, we know that the properties of the concrete are non-uniform. Consequently, in the experiment, the location of complete fracture is controlled by the existence of a locally weak section near the midpoint. Unloading from this fracture quenches the growth of cracks at other potential fracture locations. (This would also be true in a static experiment, that is, the weakest section in the specimen would control the location of failure. All other locations would unload at the time of failure.) Thus, we adopt the standard practice of introducing a perturbation to the specimen to induce strain localization at the desired location.

Calculation B was performed to demonstrate how the properties at the origin can be modified to ensure that complete fracture occurs only at the origin. The rod was modeled with the "Softening" relation used before, but the cell at the origin was given 80% of the strength of the cells in the rest of the rod, using the strain-softening relation labeled "80% Strength" in Figure 5(b). In this calculation complete fracture occurred only at the origin. The strain history from this calculation is plotted in Figure 6. The shape of the calculated strain history at the strain gage location is noticeably flatter than the measured strain histories. Although complete fracture occurred only at the origin, the plot of peak strains in Figure 7 shows that inelastic tensile strain (associated with the peak computed fracture volume per unit area) was distributed over several centimeters and exhibited a concentration at the 2.66-cm location.

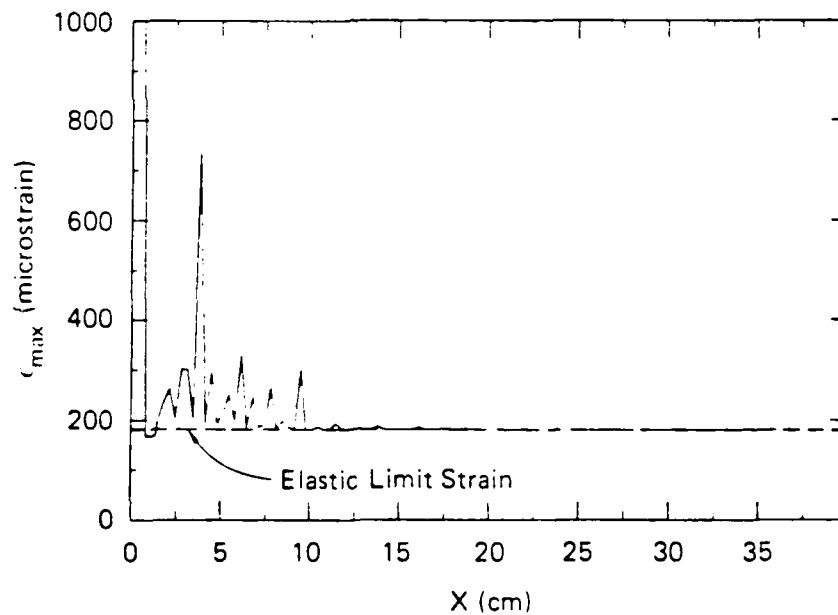
Variation of the Unloading Modulus

Calculation C was performed to investigate the effects of the unloading modulus assumed for the cells that undergo inelastic strain but do not fracture completely. In the previous two calculations, unloading followed a straight line to the origin. In Calculation C, unloading followed a straight line parallel to the elastic loading line. The relations used in Calculation C are plotted in Figure 5(c). The strain histories calculated with elastic unloading are shown in Figure 8. These should be compared with the strain histories from



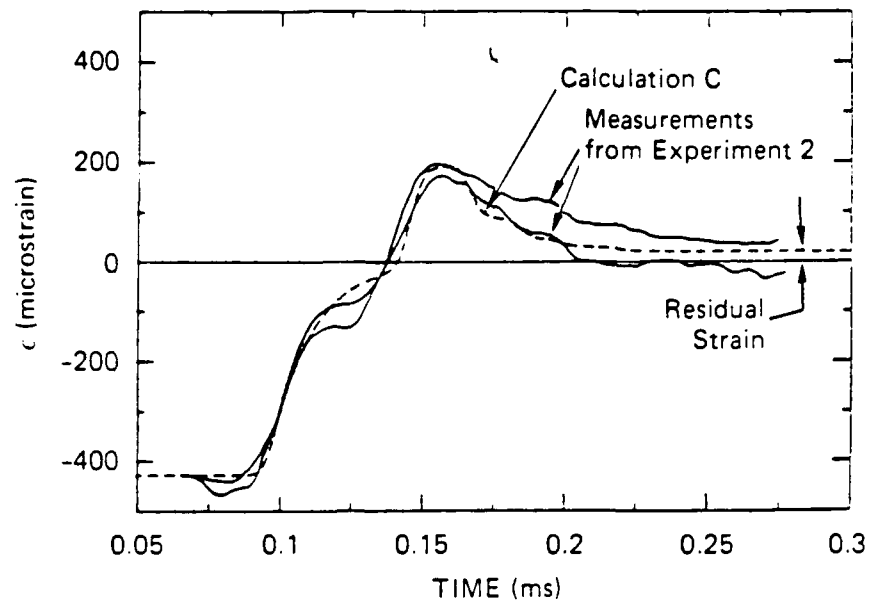
RA-314522-40

Figure 6. Strains calculated using the 80% strength relation at the origin and the softening relation in the rod (Calculation B).



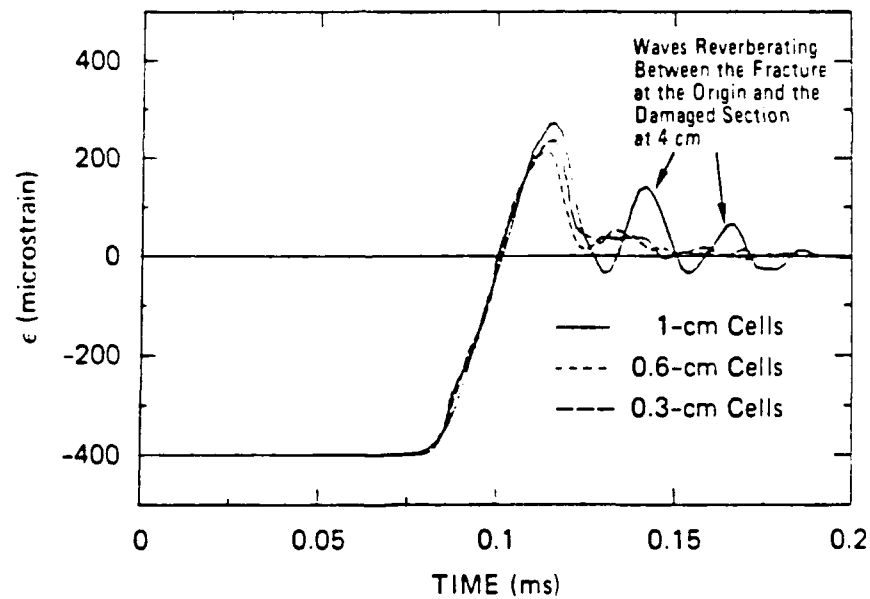
RA-314522-41

Figure 7. Peak strains calculated using the 80% strength relation at the origin and the softening relation in the rod (Calculation B).



RA-314522-42

Figure 8. Strains calculated using strain-softening relations with elastic unloading (Calculation C).



RA-314522-43

Figure 9. Cell-size dependence of strains calculated using a strain-softening model (Calculation Set D).

Calculation B (Figure 6). Primarily, the effect of elastic unloading is to produce a residual tensile strain. This puts the calculated strain at 7.62 cm in slightly better agreement with one of the measurements from the experiment. Another effect of elastic unloading is to decrease the duration of the strain pulse. This effect is caused by the greater wave speed associated with the steeper unloading slope.

Variation of the Cell Size

The cell size in these calculations has the role of a material parameter because it is equivalent to an effective crack spacing. That is, each cell represents a potential failure plane surrounded by elastic material. In the derivation of the strain-softening model, it was pointed out that the ultimate strain consistent with the critical fracture volume per unit area depends on the cell size in the calculation $\epsilon_{ult} = \delta_c / l_0$. In addition, the unrecovered work per unit area in a partially damaged cell depends on the cell size (Eq. 3).

Thus, before the simulations of the experiments were attempted, a study of cell size dependence was conducted. Calculation set D was performed with cell sizes of 0.3 cm, 0.6 cm, and 1.0 cm. The same $\sigma(\delta)$ relation used in all the calculations was linear with $\sigma_c = 5$ MPa and $\delta_c = 6 \mu\text{m}$. As suggested by the previous results of the parameter study, the cell at the origin was given 80% of the strength in the rest of the rod. As before, the rod was preloaded with 10 MPa compression, and the load was released with an exponential decay with a time constant of 15 μs . The calculated strains at 2 cm from the origin are plotted in Figure 9. The strains from the 0.3-cm, and 0.6-cm cells are in good agreement at both locations and appear to approximate the ideal plasticity solution. The strains from the 1-cm cells are qualitatively different at both locations. This calculation also predicts a very large local strain at the 4-cm location that is not predicted in the other cases. The contrast indicates how the predicted response depends on the effective crack spacing (cell size).

SIMULATIONS OF THE EXPERIMENTS

The experiments analyzed here are labeled Experiment 1 and Experiment 2. To simulate an experiment, the stress-strain relations and the cell size in the rod and at the locations of complete fracture were varied until the calculated strains matched the measured strains. Both of the experiments were simulated very well using the same failure properties. The measured elastic constants and the measured density were used in both cases. Complete fracture was forced to occur at the observed locations of failure by degrading the properties of the rod at those locations to 80% of the strength in the rest of the rod, as described below.

The simulations shown below were performed using 0.635-cm cells. This cell size was found to be the one that worked best. When 0.333-cm cells were used, the roundness of the peaks of the measured strain histories could not be matched. The calculated strain histories were too flat. When 1-cm cells were used, additional complete fractures would

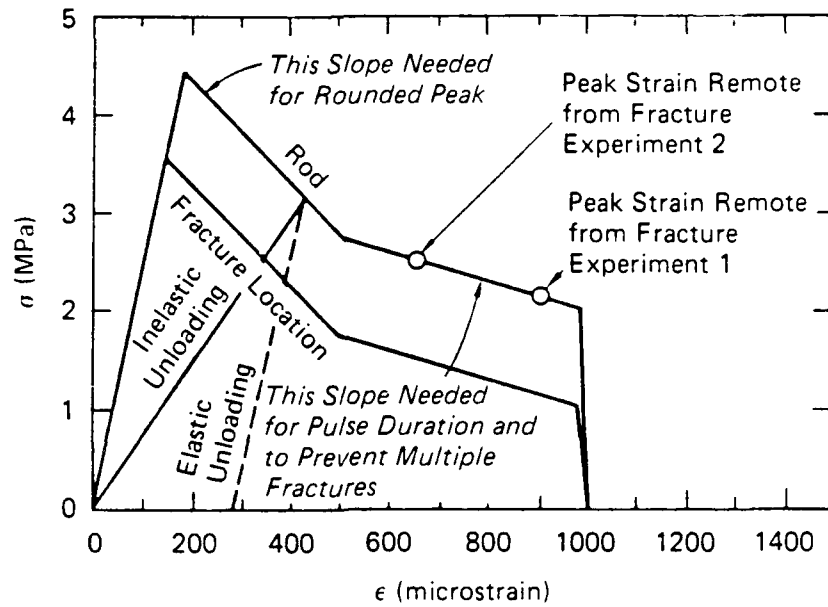
occur in the rod. The 0.635-cm dimension is the diameter of the largest aggregate particles and is roughly equal to the average axial spacing of the largest aggregate particles. This cell size is considerably smaller than was found to work best in static analyses performed by Bazant and Oh (1983). Perhaps this is because stress-wave loading excites more potential fracture sites before the unloading wave from a complete fracture quenches further damage.

The strain-softening relations used in the simulation of Experiments 1 and 2 are shown in Figure 10. (Variations were made to the $\sigma(\epsilon)$ relation directly; the $\sigma(\delta)$ relation was then derived.) The strength (peak of the stress-strain curve) assigned to the rod was 4.4 MPa, 30% higher than the measured static splitting strength. In both cases, the strength at the complete fracture location, (0.46 cm from the midpoint in Experiment 1 and 0.1 cm from the midpoint in Experiment 2) was degraded to 3.5 MPa (80% of the strength in the rest of the rod) to produce complete fracture only at the desired location. The critical fracture volume per unit area was about 6 μm . This is slightly larger than one might expect; it corresponds, for example, to the volume of a 5-cm-diameter crack under a free-field tension of about 3 MPa.

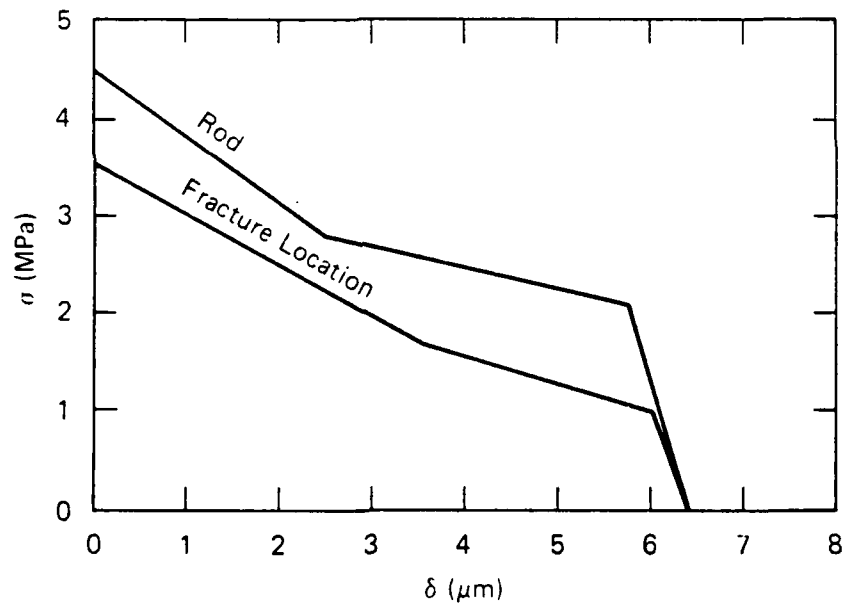
The strength levels were chosen to obtain a good prediction of the peak strains. (Higher strength gives higher peak strains.) The initial softening slope of the stress-strain relation was chosen to match the rounded peaks in the strain histories. (A steeper slope gives more pointed peaks, a less steep slope gives flatter peaks.) The critical fracture volume per unit area was chosen so that the pulse duration of the computed strains would match that of the measured strains, and to prevent multiple fractures. (A smaller critical value results in a shorter duration pulse and multiple fractures.) The 1 MPa difference between the two curves out to the ultimate strain was needed to prevent multiple fractures. (A smaller difference would result in multiple fractures.) Although the curves in Figure 10 were chosen strictly to produce a good match to the measured strain histories, it is interesting that the form of the curves is similar to the static measurements made by Willam, et al (1984) on a lower strength concrete.

Experiment 1

The comparisons of calculated and measured strains at ± 7.62 cm in Experiment 1 are shown in Figure 11. (The calculated strains for Experiments 1 and 2 are the average of the four cells spanning the strain-gage locations.) As the comparisons of strain histories show, this set of stress-strain relations produces a very good match to the experimental results. The calculated peak strains for this case are shown in Figure 12. At the locations of the strain gages, the calculated inelastic strain (averaged over the length of the gage) was only about 10 microstrain. Thus, the assumption that the measured peak strains were elastic would give a reasonable approximation to the strength. However, inelastic strain occurred nearly everywhere in the rod, so a strictly elastic analysis would not be appropriate. In particular, damage was concentrated at two locations about 3 cm from the fracture. The magnitudes of these peaks imply that less than half of the unrecovered work done was



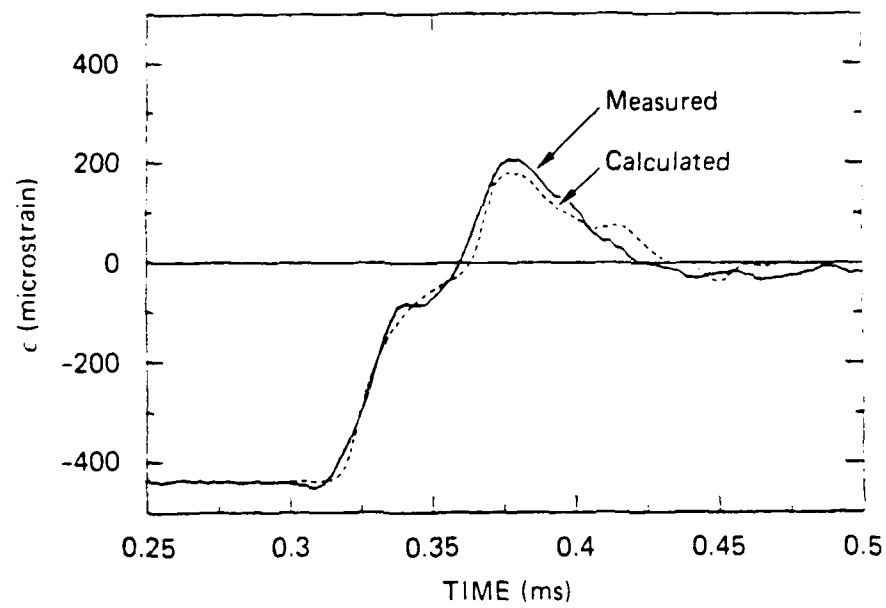
(a) Stress versus Strain



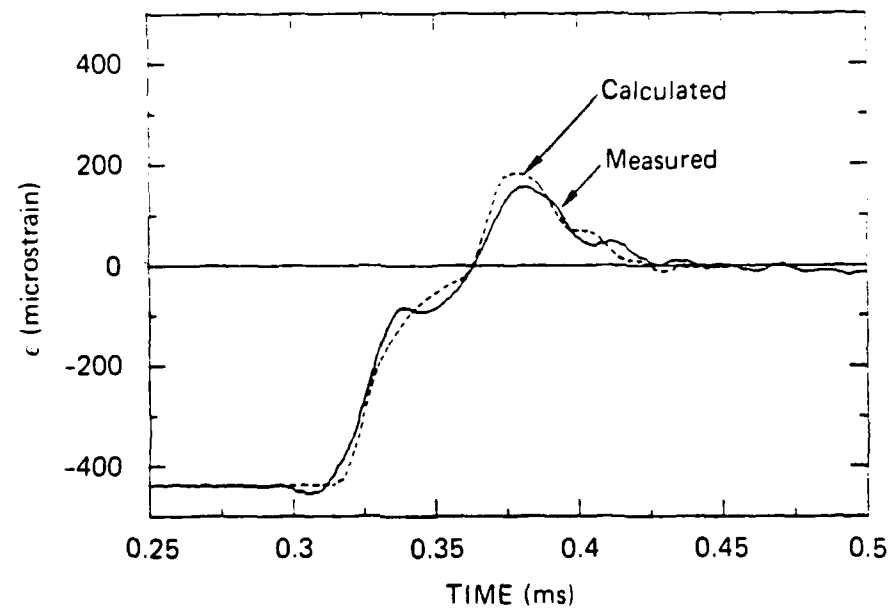
(b) Stress versus Fracture Volume per Unit Area

JA-4451-94D

Figure 10. Strain-softening relations used to simulate Experiments 1 and 2 (0.635 cm cells).



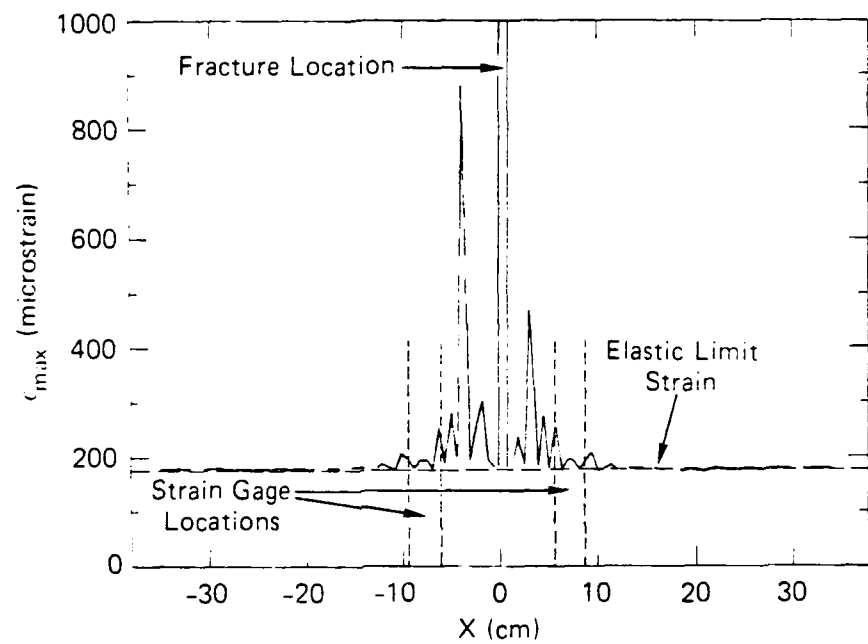
(a) $X = -7.66$ cm



(b) $X = 7.66$ cm

JA-4451-95B

Figure 11. Calculated and measured strains for Experiment 1.



JA-4451-96A

Figure 12. Peak strains calculated for Experiment 1.

energy released at the location of complete fracture.

Experiment 2

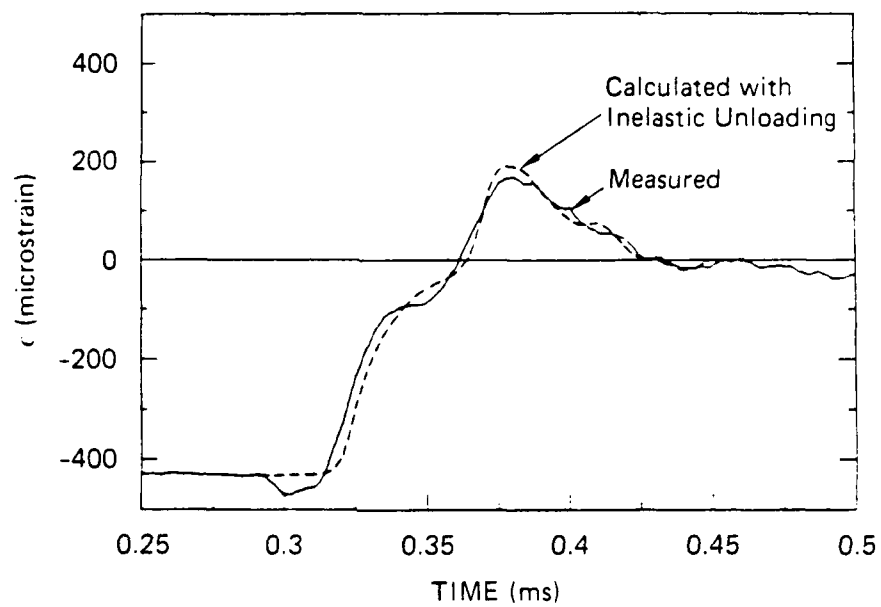
To simulate Experiment 2, the same stress-strain relations were used, but the weakened cell was centered at the midpoint of the rod. (In the experiment, the fracture location was only 0.10 cm from the midpoint of the rod.) Two simulations were performed, one with linear unloading to the origin, and one with elastic unloading, as shown in Figure 10. The results are compared with the strains measured in the experiment in Figure 13. The strain measured at +7.62 cm compares very well with the strain predicted using inelastic unloading. On the other hand, the strain measured at -7.62 cm has a residual amplitude similar to the prediction with elastic unloading. No attempt was made to improve the comparisons by changing the stress-strain relations.

Because the loading and fracture location in this experiment were essentially symmetric, the strains at ± 7.62 cm would be expected to be the same. Because the measured strains were different at the two locations, the effects of inhomogeneities not included in the simulation must have caused this asymmetric response. The two simulations with different unloading paths suggest that the asymmetry is at least partly associated with inhomogeneities in unloading characteristics.

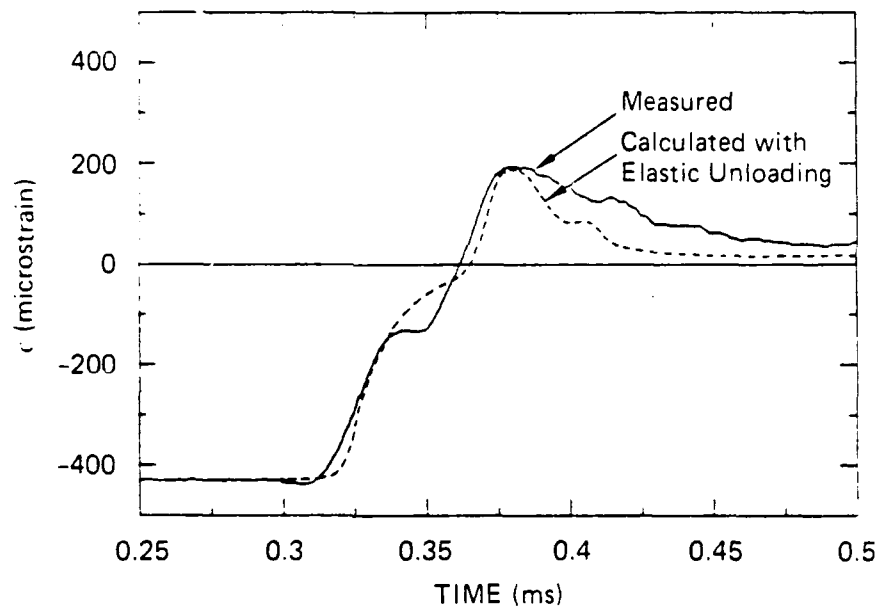
DISCUSSION

The first point of discussion is the fact that this trial-and-error exercise certainly does not produce a unique interpretation of these experiments. Within the assumptions of the model however, that the failure is associated with cracking and that the cracks are separated by finite dimension, we found that there is a very narrow range of parameter choices that produce agreement with the experimental observations. That is, seemingly small deviations from the parameters given here result in much poorer agreement with the experiments. The critical test of the parameter set lies in matching the strain histories while also preventing multiple fractures.

Secondly, whereas the dynamic experiments produced a single complete fracture with no visible secondary damage, the calculations predicted some inelastic strain to occur virtually throughout the specimen, with concentrations of inelastic strain within a few centimeters of the locations of complete fracture. Simulations in which this distributed damage did not occur showed poor agreement with the measured strains. This result suggests that extensive microcracking in the concrete may have occurred in the experiments in the region of the specimen surrounding the complete fracture location. In fact, a posttest microscopic inspection made by Gran and Seaman (1986) of the interior of a specimen from a similar experiment did show distributed microcracking that is qualitatively consistent with the strain-softening predictions of maximum strain. These microcrack observations have not yet been fully quantified, however, so a direct comparison is not shown here.



(a) $X = -7.66$ cm with Inelastic Unloading



(b) $X = 7.66$ cm with Elastic Unloading

JA-4451-97B

Figure 13. Calculated and measured strains for Experiment 2.

Finally, we noticed that the calculated stress at the complete fracture location (not shown) drops from 3.5 MPa to zero in about 10 μ s. This observation raises the question of how the strain history at the measurement locations can have a decay time of about 50 μ s. The answer is that the inelastic strain between the fracture location and the strain gage locations drastically alters the tensile stress wave as it propagates. In fact, for matching the strain measurements, the description of the material behavior in this region has a far greater effect than does that at the location of complete fracture. (A calculation in which the cell at the fracture location is given the same strength as before but with only half the ultimate strain produces a much quicker decay of stress at the fracture location but only a slightly quicker decay in strain at the strain gage locations.) That is, the calculations are not as sensitive to the details of the softening properties at the location of complete fracture, except that fracture must occur there. Thus, the properties assumed for the rest of the rod, rather than those assumed for the fracture location, are a better description of the material in general.

SUMMARY AND CONCLUSIONS

A one-dimensional strain-softening model was used in wave-propagation calculations to interpret results of dynamic tension experiments on concrete rods. The model is based on the assumption that the stress-strain relation is not a property of a material point (as in continuum theory), but is an average property of a finite volume of material containing a developing crack or failure plane. The stress-strain relation thus has associated with it a finite dimension, namely an effective crack separation distance.

Using the idealized one-dimensional strain-softening stress-strain relation, two dynamic unconfined tension experiments were simulated several times with trial sets of the material parameters until good agreement with the measured strains was obtained in both cases. The two experiments were simulated with the same set of stress-strain relations, which is consistent with the fact that the experimental results were very similar both qualitatively and quantitatively. In addition to providing an estimate of the dynamic tensile properties of the concrete, these calculations suggest that tensile damage in the concrete was distributed over several centimeters. Finally, the calculations suggest that the strain history measured a few centimeters from the location of complete fracture is primarily a function of inelastic wave propagation from this location to the strain gage (through a region of distributed tensile damage), and is less dependent on the behavior of the material at the location of complete fracture.

The stress-strain relations used to obtain the best match with the data certainly cannot be considered unique, but there is not very much latitude in the choice of the material parameters that produce a good match with the measurements. Based on these analyses, the unconfined tensile strength of the concrete at a strain rate of 10/s to 20/s is about 4.4 MPa, nearly 30% higher than the static splitting tensile strength of 3.4 MPa. The stress versus fracture volume relation is not linear, the critical fracture volume per unit area is

about 6 μm , and the effective crack spacing is about 0.635 cm. The critical fracture volume is larger and the effective crack spacing smaller than would be derived from static experiments and analyses. These parameters are apparently dependent on the dynamics of fracture.

ACKNOWLEDGMENT

This work was sponsored by the U. S. Air Force Office of Scientific Research on Contract F49620-82-K-0021, and was submitted by the first author as partial fulfillment of the requirements for the degree of Doctor of Philosophy. Mr. J. Kempf assisted with the computations, Mr. L. Gerrans prepared the illustrations, and Ms. B. Eckardt prepared the manuscript.

APPENDIX I. - REFERENCES

- Bazant, Z. P. (1976), "Instability, Ductility, and Size Effect in Strain-Softening Concrete," ASCE Journal of Engineering Mechanics, Vol.102, No. EM2, pp. 331-344.
- Bazant, Z. P. and B. H. Oh (1983), "Crack Band Theory for Fracture of Concrete," *Materiaux et Constructions*, Vol. 16, No. 93, pp. 155-177.
- Belytschko, T. and Z. P. Bazant (1984), "Strain-Softening Materials and Finite Element Solutions," Proceedings of the ASME Winter Annual Meeting, New Orleans, LA.
- Gran, J. K., Y. M. Gupta and A. L. Florence (1987), "An Experimental Method to Study the Dynamic Tensile Failure of Brittle Geologic Materials," *Mechanics of Materials*, Vol 6, No. 2, pp. 113-125.
- Gran, J. K. and L. Seaman (1986), "Observations and Analyses of Microcracks Produced in Dynamic Tension Tests of Concrete," SRI International, Final Report to AFOSR, Contract No. F49620-82-K-0021.
- Hillerborg, A., M. Modeer, and P-E Petersson (1976), "Analysis of Crack Formation and Growth in Concrete by Means of Fracture Mechanics and Finite Elements," *Cement and Concrete Research*, Vol. 6, pp. 773-782.
- Kipp, M. E. and D. E. Grady (1985), "Dynamic Fracture Growth and Interaction in One Dimension," *Journal of the Mechanics and Physics of Solids*, Vol. 33, No. 4, pp. 399-415.
- Ottosen, N. S. (1986), "Thermodynamic Consequences of Strain Softening in Tension," ASCE Journal of Engineering Mechanics, Vol. 112, No. 11, pp. 1152-1164.

Sandler, I. S. and J. P. Wright (1984), "Strain Softening," in Theoretical Foundation for Large-Scale Computations of Nonlinear Material Behavior, S. Nemat-Nasser ed., Martinus Nijhoff.

Seaman, L. (1978), "SRI PUFF 8 Computer Program for One-Dimensional Stress Wave Propagation," SRI International Final Report to U. S. Army Ballistics Research Laboratory, Contract No. DAAK11-77-C-0083, Vol. II.

Willam (1984), K. J., S. Sture, N. Bicanic, J. Christensen, and J. Hurlbut, "Strain-Softening Properties and Computational Predictions of Localized Fracture," University of Colorado, Boulder, CO, Technical Report No. AFOSR-TR-84-0423.

APPENDIX II. - NOTATION

The following symbols are used in this paper:

- E = elastic modulus
- σ = stress
- σ_0 = tensile strength
- ϵ = strain
- ϵ_0 = strain at peak stress
- ϵ_{ult} = ultimate strain
- l_0 = initial cell dimension
- δ = fracture volume per unit area
- δ_c = critical fracture volume per unit area
- G_c = fracture energy per unit area
- G' = work done to partially fracture a cell

APPENDIX C
A SUBROUTINE FOR DETERMINING STRESS INTENSITY VALUES,
CRACK OPENINGS, AND EFFECTIVE MODULI FOR
MULTIPLE CRACKS IN AN ELASTIC MATERIAL

1. INTRODUCTION

Kachanov¹ has constructed an approximate analysis for computing stress intensity values for arrays of cracks of arbitrary locations, lengths, and orientations in an elastic solid. This report outlines an implementation of Kachanov's procedure into a computer program for routine evaluation of these stress fields.

The method is based on classical solutions for the stress states around a two-dimensional flat crack in an infinite elastic body under external tractions. The procedure provides for a simultaneous solution for the stress intensity values (K_I and K_{II}) at each end of each crack in the array. With these K values, the crack opening shape is determined. From the crack shape, the average crack opening strain in the body can be found.

This Appendix outlines the basic analytical procedure developed by Kachanov and then describes the techniques used in our program. Some comparisons with exact solutions are given.

2. OUTLINE OF KACHANOV'S METHOD

Kachanov considers an array of two-dimensional cracks embedded in an elastic material under a remote loading (σ^∞). We assume that the cracks are of arbitrary length, location, and orientation. The length of the r^{th} crack is given by L_r and the orientation by the unit normal \vec{n}_r .

To quantify these cracks, Kachanov² forms a crack density tensor **A** with the following definition:

$$\mathbf{A} = \sum_{r=1}^R L_r^2 \vec{n}_r \vec{n}_r \quad (1)$$

and represents the normals in the \vec{i}, \vec{j} coordinate system thus:

$$\vec{n}_r = n_r^{(i)} \vec{i} + n_r^{(j)} \vec{j} \quad (2)$$

or

$$\vec{n}_r = \cos \theta_r \vec{i} + \sin \theta_r \vec{j} = -\sin \phi_r \vec{i} + \cos \phi_r \vec{j} \quad (3)$$

where θ_r is the angle from the \vec{i} direction to the normal to the crack plane and ϕ_r is the angle from \vec{i} to the crack plane. Note that the factor $\vec{n}_r \vec{n}_r$ on the right in Equation (1) is a dyad, not a vector or dot product. Then the components of the crack density tensor are

$$A_{ij} = \sum_{r=1}^R L_r^2 n_r^{(i)} n_r^{(j)} \quad (4)$$

From its definition, we can see that \mathbf{A} is a symmetric second order tensor (as a sum of such). This tensor describes the lengths and orientations of the cracks but not their locations in the material. The principal axes of \mathbf{A} are the axes of orthotropy. In more detail, \mathbf{A} is given by the following equation:

$$\mathbf{A} = \sum_r L_r^2 \left[\sin^2 \phi_r \vec{i} \vec{i} + \cos^2 \phi_r \vec{j} \vec{j} - \sin \phi_r \cos \phi_r (\vec{i} \vec{j} + \vec{j} \vec{i}) \right] \quad (5)$$

or the matrix of components

$$\mathbf{A} = \begin{vmatrix} \sum_r L_r^2 \sin^2 \phi_r & - \sum_r L_r^2 \sin \phi_r \cos \phi_r \\ - \sum_r L_r^2 \sin \phi_r \cos \phi_r & \sum_r L_r^2 \cos^2 \phi_r \end{vmatrix} \quad (6)$$

The stress acting along each crack is a superposition of the external stress field on the stress field caused by the opening of each of the other cracks. To proceed, Kachanov considers just two cracks and their interactions. He evaluates first the interaction stresses $\sigma_{sr}^n(\xi)$ and $\sigma_{sr}^r(\xi)$: the stresses at position ξ along the s^{th} crack generated by uniform normal and shear tractions of unit intensity along the r^{th} crack. To obtain the actual stresses along the s^{th} crack, we multiply by the average of the normal or shear stresses on the r^{th} crack: $\langle P_r \rangle$ and $\langle \tau_r \rangle$. This use of the average stresses on the cracks is the essential ingredient of Kachanov's method that simplifies the solution enough to make it practical.

With the foregoing definitions, we can now write the basic equation for the normal and shear stress at any point ξ along the s^{th} crack as a function of the external normal and shear loading (P_s^∞ and τ_s^∞) and the interaction stresses from the other cracks.

$$P_s(\xi) = P_s^\infty + \bar{n}_s \left[\sum_{r \neq s} \sigma_{sr}^n(\xi) \langle P_r \rangle + \sigma_{sr}^r(\xi) \langle \tau_r \rangle \right] \bar{n}_s \quad (7)$$

$$\tau_s(\xi) = \tau_s^\infty + \bar{n}_s \left[\sum_{r \neq s} \sigma_{sr}^n(\xi) \langle P_r \rangle + \sigma_{sr}^r(\xi) \langle \tau_r \rangle \right] - \left[P_s(\xi) - P_s^\infty \right] \bar{n}_s \quad (8)$$

Here $P_s^\infty = \bar{n}_s \sigma^\infty \bar{n}_s$ and $\tau_s^\infty = \bar{n}_s \sigma^\infty - P_s^\infty \bar{n}_s$ are the normal and shear tractions induced along the s^{th} crack length by the remote loading in the absence of the cracks. The \bar{n}_s factors are normals to the plane of the s^{th} crack; hence, their presence in the equations provides for a standard angular transformation of the applied stresses onto the s^{th} crack plane. The quantities σ_{sr}^n and σ_{sr}^r are the stresses

generated along the s^{th} crack trace by uniform tractions (normal and shearing) of unit intensity acting on the r^{th} crack. These stresses are listed in Section 5 below for convenience. The $\langle P_r \rangle$ and $\langle \tau_r \rangle$ quantities are obtained by averaging the normal and shear stresses acting along the r^{th} crack.

The first step toward solution is to average the stresses in Equations (7) and (8) along the crack lengths.

$$\langle P_s \rangle = P_s^\infty + \sum_{r \neq sj} (\Lambda_{sr}^{nn} \langle P_r \rangle + \Lambda_{sr}^{\tau n} \langle \tau_r \rangle) \quad (9)$$

$$\langle \tau_s \rangle = \tau_s^\infty + \sum_{s \neq r} (\Lambda_{sr}^{n\tau} \langle P_r \rangle + \Lambda_{sr}^{\tau\tau} \langle \tau_r \rangle) \quad (10)$$

The Λ quantities in these equations combine the averaging process over the length of the s^{th} crack and the tensor transformation for orientation.

$$\Lambda_{sr}^{nk} = \vec{n}_s \langle \sigma_{sr}^k \rangle \vec{n}_s \quad (11)$$

$$\Lambda_{sr}^{\tau k} = \vec{n}_s \langle \sigma_{sr}^k \rangle - \Lambda_{sr}^{nk} \vec{n}_j \quad (12)$$

where k refers to either n or τ .

The second step in the solution is to compute the Λ quantities in Equations (9) and (10). The simultaneous equations given by Equations (9) and (10) can be written in matrix form as follows:

$$\mathbf{TP} = \mathbf{F} \quad (13)$$

where \mathbf{T} is a matrix based on the Λ values, \mathbf{P} is a vector containing the averaged quantities $\langle P_s \rangle$ and $\langle \tau_s \rangle$, and \mathbf{F} is a vector of the external tractions P_s^∞ and τ_s^∞ .

Next, the matrix \mathbf{T} is inverted to solve for \mathbf{P} . With the average values of the stresses on each crack known, we can return to Equations (7) and (8) to compute the stresses $P_s(\xi)$ and $\tau_s(\xi)$ along the crack lengths.

Stress Intensity Factors

With the stresses known along the crack lengths, the stress intensities are computed from the following formulas:

$$K_I(\pm L) = \frac{1}{\sqrt{\pi L}} \int_{-L}^L \left[\frac{L \pm \xi}{L \mp \xi} \right]^{1/2} P(\xi) d\xi \quad (14)$$

and

$$K_{II}(\pm L) = \frac{1}{\sqrt{\pi L}} \int_{-L}^L \left[\frac{L \pm \xi}{L \mp \xi} \right]^{1/2} \tau(\xi) d\xi \quad (15)$$

where L is half the crack length.

Crack Opening Displacement

The crack opening (normal displacement) is computed using the following shape function for a quadratically distorted ellipse, obtained by multiplying the expression for the coordinate of an ellipse by a quadratic. By using the quadratic, Kachanov is allowing the crack shape to distort from the ellipse that would be obtained for an isolated crack. The normal crack opening (b_n) is

$$b_n = \frac{4L}{E} S_n \left(1 + \alpha_n \frac{\xi}{L} + \beta_n \frac{\xi^2}{L^2} \right) \sqrt{1 - \xi^2/L^2} \quad (16)$$

A similar formula is written for b_r , the shearing displacement. Kachanov gives

expressions for S_n , α_n , and β_n in terms of K_I and K_{II} at both ends of the crack.

$$S_n = 2 \langle P_s \rangle - \frac{K_I(L) + K_I(-L)}{2\sqrt{\pi L}} \quad (17)$$

$$\alpha_n = \frac{K_I(L) - K_I(-L)}{4 \langle P_s \rangle \sqrt{\pi L} - [K_I(L) + K_I(-L)]} \quad (18)$$

$$\beta_n = \frac{K_I(L) + K_I(-L) - 2 \langle P_s \rangle \sqrt{\pi L}}{4 \langle P_s \rangle \sqrt{\pi L} - [K_I(L) + K_I(-L)]} \quad (19)$$

For the shearing displacement b_r , identical expressions are used for S_r , α_r , and β_r , except that K_I is replaced by K_{II} and $\langle P_s \rangle$ is replaced by $\langle \tau_s \rangle$. In all these foregoing equations for the crack opening, $\langle P_s \rangle$ and $\langle \tau_s \rangle$ are the values from Equations (9) and (10); that is, the average normal and shearing stresses on the crack face. Hence, with the K values known, the normal and shearing displacements of the crack surfaces can be found.

The average opening displacement of the cracks is given by integrating the b_n value over the area of the crack face:

$$\langle b_n \rangle = \frac{\pi L S_n}{E} (1 + \beta_n/4) \quad (20)$$

and the crack volume (B_n) is

$$B_n = \frac{4\pi L^2 S_n}{E} (1 + \beta_n/4) \quad (21)$$

Similar expressions can be formed for the average and total shearing distortions $\langle b_r \rangle$ and B_r .

Effective Elastic Moduli

The derivation of the effective moduli begins with the determination of the appropriate coordinate axes for the modulus tensor. Kachanov notes that if crack interactions are neglected, the effective properties are always orthotropic (that is, they have rectangular symmetry) for any crack configurations. Thus, in the approximation of noninteracting cracks, the axes of orthotropy provide a natural coordinate system for effective moduli when interactions are taken into account. Therefore, Kachanov outlines the following steps for determining the effective moduli:

Step 1: Find the axes of orthotropy (\bar{e}_1, \bar{e}_2) assuming the cracks do not interact.

Step 2: Find the effective properties for interacting cracks in the coordinate system \bar{e}_1, \bar{e}_2 .

In the first of these steps the axes of orthotropy are determined using the **A** matrix given in Equation (6). The angle α measured counterclockwise from the \bar{i} direction in the i, j external coordinate system is computed as follows from the components of the **A** matrix:

$$\tan 2\alpha = -2 \frac{A_{12}}{A_{11} - A_{22}} \quad (22)$$

We begin step 2 by looking for matrix C_{ijkl} of effective compliances:

$$\langle \epsilon_{ij} \rangle = C_{ijkl} \sigma_{kl}^{\infty} \quad (23)$$

where $\langle \rangle$ indicates a volume average and the stresses are the remotely applied ones. Hereafter, i, j, k , and l refer to the orthotropic axes \bar{e}_1 and \bar{e}_2 .

The general formula for the derivation of the elastic coefficient matrix C_{ijkl} is

$$\langle \underline{\epsilon} \rangle = \mathbf{C}^o : \underline{\sigma}^\infty + \frac{1}{2S} \sum_r (\vec{n}_r \vec{b}_r + \vec{b}_r \vec{n}_r) L_r \quad (24)$$

where S is the area of the elementary cell containing the cracks, \mathbf{C}^o is the elastic compliance, and $\underline{\sigma}^\infty$ is the externally applied stress. The \vec{n} vectors are normal unit vectors. \vec{b}_r is the average displacement discontinuity across the r^{th} crack. Referring to Equation (20), \vec{b}_r has the definition

$$\vec{b}_r = \langle b_n \rangle \vec{m}_n + \langle b_r \rangle \vec{m}_r \quad (25)$$

and \vec{m}_n and \vec{m}_r are unit vectors in the direction normal and along the r^{th} crack.

For \vec{b}_r Kachanov makes the following approximation to Equation (20):

$$\vec{b}_r \doteq \frac{\gamma \pi}{E_o} L_r \vec{t}_r \quad (26)$$

where \vec{t}_r is the average traction provided by Kachanov's method and

$$\gamma = \frac{S_n}{t_r} \left(1 + \frac{\beta_n}{4} \right) \quad (27)$$

and γ is assumed to be 1. Here Kachanov is neglecting the fact that crack opening depends on the orientation of the applied stress. Now Equation (24) can be written

$$\langle \underline{\epsilon} \rangle = \mathbf{C}^o : \underline{\sigma}^\infty + \frac{\pi}{2E_o S} \sum_r (\vec{n}_r \vec{t}_r + \vec{t}_r \vec{n}_r) L_r^2 \quad (28)$$

To construct the $\vec{n} \vec{t}$ quantities in the preceding equation, we let

$$\vec{t}_r = t_{r1}\vec{e}_1 + t_{r2}\vec{e}_2 \quad (29)$$

Now we rewrite Equation (2) as

$$\vec{n}_r = n_r^{(1)}\vec{e}_1 + n_r^{(2)}\vec{e}_2 \quad (30)$$

Then we combine this definition of \vec{n}_r with that for \vec{t}_r and form the products in Equation (28).

$$\vec{n}\vec{t}_r = \vec{t}_{r1}(n_r^{(1)}\vec{e}_i\vec{e}_i + n_r^{(2)}\vec{e}_j\vec{e}_i) + \vec{t}_{r2}(n_r^{(1)}\vec{e}_i\vec{e}_j + n_r^{(2)}\vec{e}_j\vec{e}_j) \quad (31)$$

With reversed symbols, the equation is

$$\vec{t}_r\vec{n} = \vec{t}_{r1}(n_r^{(1)}\vec{e}_i\vec{e}_i + n_r^{(2)}\vec{e}_i\vec{e}_j) + \vec{t}_{r2}(n_r^{(1)}\vec{e}_j\vec{e}_i + n_r^{(2)}\vec{e}_j\vec{e}_j) \quad (32)$$

The only difference between Equations (31) and (32) is the reversal of the vector pairs $\vec{e}_i\vec{e}_j$ in the central two terms. With Equations (31) and (32) in Equation (28), we can see the form the compliance equation must take. The stress quantities σ_{kl} in Equation (23) are applied one at a time, so the \vec{t}_r quantities always represent just one applied stress component. The vectors \vec{e}_i and \vec{e}_j then correspond to the directions of the strain \vec{e}_{ij} .

Let us now examine the $\vec{n}\vec{t}$ expressions in preparation for programming them into the code. First examine the \vec{n}_r terms in Equation (30).

$$\vec{n}_r = \cos(\theta_r - \alpha)\vec{e}_1 + \sin(\theta_r - \alpha)\vec{e}_2 \quad (33)$$

The t_{r1} and t_{k2} terms are derived in a three-step procedure:

1. Apply a unit external stress in the \vec{e}_1 - \vec{e}_2 orthotropic plane, and transform this stress to the fixed \vec{i} - \vec{j} plane to obtain the components σ_{xx} , σ_{yy} , and σ_{xy} .
2. Determine the normal and shear stresses on each plane from this external loading.
3. From the P_s^∞ and τ_s^∞ arrays and the \mathbf{T} matrix, derive the modified normal and shear stresses ($\langle P_s \rangle$ and $\langle \tau_s \rangle$) on each crack, accounting for the presence of the other cracks.

Now the argument in the sum in Equation (28) can be written out. The expression is

$$\begin{aligned} \vec{n}_r \vec{t}_r + \vec{t}_r \vec{n}_r = & 2t_{r1} \cos(\theta_r - \alpha) \vec{e}_1 \vec{e}_1 + (t_{r1} \sin(\theta_r - \alpha) + t_{r2} \cos(\theta_r - \alpha)) \vec{e}_2 \vec{e}_1 \\ & + (t_{r1} \sin(\theta_r - \alpha) + t_{r2} \cos(\theta_r - \alpha)) \vec{e}_1 \vec{e}_2 + 2t_{r2} \sin(\theta_r - \alpha) \vec{e}_2 \vec{e}_2 \end{aligned} \quad (34)$$

Hence, with each loading σ_{kl}^∞ , we can derive 4 ϵ terms (ϵ_{11} , ϵ_{22} , and $\epsilon_{12} = \epsilon_{21}$). The applied external stresses are σ_{11} , σ_{22} , and $\sigma_{12} (= \sigma_{21})$. Note that in our transformations we recognize that σ_{12} and σ_{21} are always applied together.

Kachanov begins the computation of the compliances C_{ijkl} with the application of a 'trial' stress (σ_{11}^∞). He states that the $\langle \epsilon_{11} \rangle$ response to this stress provides the effective Young's modulus (E_1) in the \vec{e}_1 directions, or C_{1111} .

$$\underline{\sigma}^\infty = \sigma_{11}^\infty \vec{e}_1 \vec{e}_1 \quad (35)$$

and we can take σ_{11}^∞ as unity. Then

$$\langle \epsilon_{11} \rangle = \frac{1}{E_0} + \frac{\pi}{2E_0 S} \sum_r 2L_r^2 t_{r1} n_r^{(1)} \equiv \frac{1}{E_1} \equiv C_{1111} \quad (36)$$

Here t_{r1} is the component of \vec{t}_r along \vec{e}_1 calculated under conditions of our loading σ_{11}^∞ . Thus

$$\frac{E_1}{E_o} = \frac{1}{1 + \frac{\pi}{S} \sum_r L_r^2 < t_{r1} > n_r^{(1)}} \quad (37)$$

Similar computations will yield C_{2222} .

The computation for C_{2211} proceeds as follows. Let the applied stress be the same as in Equation (35) and take σ_{11}^∞ as unity. Then

$$< \epsilon_{22} > = -\frac{\nu_o}{E_o} + \frac{\pi}{2E_o S} \sum_r 2L_r^2 t_{r2} n_r^{(2)} \equiv C_{2211} \equiv -\frac{\nu_{12}}{E_1} \quad (38)$$

where t_{r2} is the e_2 component of \vec{t}_r calculated under conditions of our loading σ_{11}^∞ .

Next we compute C_{1212} , the $< \epsilon_{12} >$ response to σ_{12}^∞ .

$$< \epsilon_{12} > = \frac{1}{2G_o} + \frac{\pi}{2E_o S} \sum_r L_r^2 \left(n_r^{(1)} t_{r2} + t_{r1} n_r^{(2)} \right) \equiv \frac{1}{2G_{12}} \quad (39)$$

The t_{r1} and t_{r2} values are components of \vec{t}_r as calculated under loading $\sigma_{12}^\infty = 1$.

The constants written above are the only non-zero ones in orthotropic material. The rest of the constants developed below characterize deviation from orthotropy. For these constants, let us start with C_{1211} , the $< \epsilon_{12} >$ response to $\sigma_{11}^\infty = 1$.

$$< \epsilon_{12} > = \frac{\pi}{2E_o S} \sum_r L_r^2 \left(n_r^{(1)} t_{r2} + t_{r1} n_r^{(2)} \right) = C_{1211} \quad (40)$$

The \vec{t}_r components are calculated under the loading of $\sigma_{11}^\infty = 1$. We can compute C_{1222} similarly.

Moduli for Noninteracting Cracks.

These moduli are for comparison, to estimate the effect of crack interactions on the overall moduli. They are given by the same formulas as the corresponding moduli for the interacting cracks, the only difference being that the tractions on cracks (\vec{t}_r) are taken as directly induced by the remote loading $\underline{\sigma}^\infty$; that is,

$$\vec{t}_r = \vec{n}_r \underline{\sigma}^\infty \quad (41)$$

The factor on the right is a dot product between the vector \vec{n}_r and the stress tensor. Thus, in the formula for C_{1111} , for example,

$$\vec{t}_r = \vec{n}_r (\sigma_{11}^\infty \vec{e}_1 \vec{e}_1) = n_r^{(1)} \vec{e}_1 \quad (42)$$

and therefore,

$$t_{r1} = n_r^{(1)} \quad \text{and} \quad t_{r2} = 0 \quad (43)$$

and hence the normalized modulus E_1/E_o is

$$\frac{E_1}{E_o} = \frac{1}{1 + \frac{\pi}{S} \sum_r L_r^2 (n_r^{(1)})^2} \quad (44)$$

and similarly for C_{2222} .

Other compliances, such as C_{2211} , are unaffected because t_{r2} is zero under σ_{11}^∞ loading. That is,

$$C_{2211} = -\frac{\nu_o}{E_o} \quad (45)$$

For C_{1212} the expression is

$$\begin{aligned} \vec{t}_r &= \bar{n}_r \sigma_{12}^\infty (\vec{e}_1 \vec{e}_2 + \vec{e}_2 \vec{e}_1) \\ &= n_r^{(1)} \vec{e}_2 + n_r^{(2)} \vec{e}_1 \\ &= t_{r2} \vec{e}_2 + t_{r1} \vec{e}_1 \end{aligned} \quad (46)$$

Then C_{1212} is computed from

$$\begin{aligned} C_{1212} &= \frac{1}{2G_o} + \frac{\pi}{2E_o S} \sum_r [(n_r^{(1)})^2 + (n_r^{(2)})^2] L_r^2 \\ &= \frac{1}{2G_o} + \frac{\pi}{2E_o S} \sum_r L_r^2 \end{aligned} \quad (47)$$

The foregoing procedure is implemented in the computer program to be described next.

3. DESCRIPTION OF THE KCRACK PROGRAM

The calculations in the program begin with the insertion of input quantities to describe the problem. The material constants E (Young's modulus) and ν (Poisson's ratio) are inserted first. Then for each crack the crack length (L), crack center (X_o, Y_o), and angle (θ) of the normal to the crack are inserted. The external field is described by S_{xx} , S_{yy} , and S_{xy} .

The normal and shear stresses on the cracks caused by the external loadings are determined by a standard tensor rotation in the subroutine CRFORC:

$$P_s^\infty = S_{xx} \cos^2 \theta_s + S_{yy} \sin^2 \theta_s + 2S_{xy} \sin \theta_s \cos \theta_s \quad (48)$$

$$\tau_s^\infty = -(S_{xx} - S_{yy}) \sin \theta_s \cos \theta_s + S_{xy} [\cos^2 \theta_s - \sin^2 \theta_s] \quad (49)$$

These quantities — P_s^∞ and τ_s^∞ — are contained in the FORCE array. A similar tensor transformation provides for evaluating the Λ quantities:

$$\Lambda_{sr}^{nn} = \frac{1}{2L_s} \left[\cos^2(\theta_j - \theta_r) \int_{L_s} \sigma_{xxsr}^n(\xi) d\xi \right. \quad (50)$$

$$\left. + 2 \sin(\theta_s - \theta_r) \cos(\theta_s - \theta_r) \int_{L_s} \sigma_{xy sr}^n(\xi) d\xi + \sin^2(\theta_s - \theta_r) \int_{L_s} \sigma_{yy sr}^n(\xi) d\xi \right]$$

The σ_{xxsr}^n quantity is the stress in the X direction (of the r^{th} crack) from the standard stress fields for normal stress on the r^{th} crack acting at the location ξ on the s^{th} crack. In constructing this stress, we use the standard fields given by Kachanov and listed in Section 5, the distance between the center of the r^{th} crack and the point ξ along the s^{th} crack, and the relative orientations (θ_r and θ_s) of the two cracks. The same expression is used for Λ_{sr}^{nr} by replacing the σ^n quantities with σ^r .

The corresponding expression for Λ_{sr}^{rn} is

$$\Lambda_{sr}^{rn} = \frac{1}{2L_s} \left[\sin(\theta_s - \theta_r) \cos(\theta_s - \theta_r) \left(\int_{L_s} \sigma_{xxsr}^n(\xi) d\xi + \int_{L_s} \sigma_{yy sr}^n(\xi) d\xi \right) \right. \quad (51)$$

$$\left. - \left(\cos^2(\theta_s - \theta_r) - \sin^2(\theta_s - \theta_r) \right) \int_{L_s} \sigma_{xy sr}^n(\xi) d\xi \right]$$

A similar expression is used for Λ_{sr}^{rr} , with σ^n replaced by σ^r .

The integrals in the foregoing expressions are evaluated by Simpson's rule in the program in the CRSTRS subroutine. The integration was tested using 10, 20,

NO 4296-896

FURTHER STUDY OF THE DYNAMIC TENSILE FAILURE OF
CONCRETE(U) SRI INTERNATIONAL MENLO PARK CA
J K GRAN ET AL APR 88 AFOSR-TR-88-8642 F49628-87-K-0010

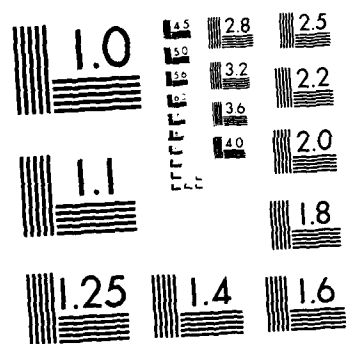
272

UNCLASSIFIED

F/G 11/2

NL





40, and 100 intervals for the case of two parallel end-to-end cracks with a spacing of $0.01 L$, where L is half the crack length. For 40 intervals or more, the results were accurate to four significant figures.

With the Λ values known, we construct the \mathbf{T} matrix with the following definitions for the components:

$$\begin{aligned}
 T_{km} &= 1 \text{ for } k = m \\
 &= 0 \text{ for } k = m + 1 \text{ or } m - 1 \\
 &= -\Lambda_{sr}^{nn} \text{ for } r = k/2 - 1/2 \text{ for } k \text{ odd, and } s = m/2 - 1/2 \text{ for } m \text{ odd} \\
 &= -\Lambda_{sr}^{rn} \text{ for } r = k/2 - 1/2 \text{ for } k \text{ odd, and } s = m/2 \text{ for } m \text{ even} \\
 &= -\Lambda_{sr}^{nr} \text{ for } r = k/2 \text{ for } k \text{ even, and } s = m/2 - 1/2 \text{ for } m \text{ odd} \\
 &= -\Lambda_{sr}^{rr} \text{ for } r = k/2 \text{ for } k \text{ even, and } s = m/2 \text{ for } m \text{ even}
 \end{aligned} \tag{52}$$

This \mathbf{T} matrix (called AMAT in the program) is inverted in CRSTRS to obtain the \mathbf{P} force vector. The \mathbf{P} vector contains the average stress (normal and shear) on each crack (Equations (9) and (10)).

With the \mathbf{P} force vector known, we can return to Equations (7) and (8) to compute the local stresses and then evaluate the stress intensities from Equations (14) and (15). These local stresses, $P_r(\xi)$ and $\tau_r(\xi)$, are computed in the subroutine CRK1 with the help of TRACTN. Because the integrals in Equations (14) and (15) are singular at both ends of their range of integration, we used Chebyshev-Gauss quadrature to evaluate them. Equation (14) was rewritten as follows for the numerical integration:

$$\begin{aligned}
 K_I(L) &= \frac{1}{\sqrt{\pi L}} \int_{-L}^L \left[\frac{L + \xi}{L - \xi} \right]^{1/2} P(\xi) d\xi \\
 &= \frac{L}{\sqrt{\pi L}} \int_{-1}^1 \frac{(1 + \xi/L) P(\xi)}{\sqrt{1 - \xi^2/L^2}} d(\xi/L)
 \end{aligned} \tag{53}$$

Then the numerical expression is

$$K_I(L) \approx \frac{\sqrt{\pi L}}{m} \sum_{i=1}^m (1 + x_i) P(x_i) \quad (54)$$

where $x_i = \cos[(2i - 1)\pi/(2m)]$, and m is the number of intervals used in the integration. The integration for K was tried with various values of m . Results that were accurate to four figures were obtained with $m = 40$.

4. EXACT SOLUTIONS FOR STRESS INTENSITY FACTORS

To evaluate the accuracy of the preceding method, it is useful to have exact solutions for some special cases. Such solutions are available for the case of two colinear cracks. In addition, Kachanov was able to obtain an analytical solution based on his approximate method. These two types of analytical solutions are presented, and some representative values of K_I are given.

In all cases, the analysis is for a pair of cracks extending along the x axis from -1 to $-k$ and from k to 1 . The elastic body is loaded by a uniform tension in the Y direction. The resulting K_I and K_{II} values are given in Table C-I. The K values listed in the columns labeled "Procedure" were obtained by the numerical method discussed in this report; those in the column labeled "Approx." by an analytical solution to the method reported here, and given by Kachanov in his paper; and those in the column labeled "Exact" by the exact analytical solution. The results in the table show that the numerical procedure gives an acceptable approximation to the exact results throughout the range of interest. Also, the numerical method is able to reproduce the values of the analytical solution to this procedure within 0.1% for crack separations down to 1% of the crack length. The surprising result of Kachanov's procedure is that it is so accurate for very close spacings of the cracks.

Exact Solution of the Approximation

For two cracks along a line, an analytical solution was obtained by Kachanov

TABLE C-I
COMPARISON OF STRESS INTENSITY VALUES

k	$K_I(k)$			Errors, %	
	Procedure	Approx.	Exact	Proc.	Approx.
0.200	1.112018	1.112018	1.112470	0.040	0.040
0.100	1.250944	1.250944	1.255122	0.333	0.333
0.070	1.346863	1.346862	1.356894	0.739	0.739
0.050	1.452423	1.452421	1.472882	1.389	1.389
0.020	1.808529	1.808426	1.904569	5.04	5.05
0.010	2.134548	2.133550	2.371571	9.99	10.04
0.007	2.317831	2.315134	2.671641	13.24	13.34
0.005	2.499528	2.493311	2.999207	16.67	16.87
0.002	3.041578	3.002006	4.164502	26.96	27.91
0.001	3.517141	3.399714	5.394657	34.80	36.98
k	$K_I(1)$			Errors, %	
	Procedure	Approx.	Exact	Proc.	Approx.
0.200	1.051580	1.051580	1.051682	0.00965	0.00963
0.100	1.085775	1.085775	1.086335	0.0516	0.0516
0.070	1.102807	1.102807	1.103874	0.0963	0.0967
0.050	1.118012	1.118011	1.119791	0.1588	0.1590
0.020	1.153792	1.153772	1.158939	0.444	0.446
0.010	1.174985	1.174831	1.184110	0.778	0.784
0.007	1.184115	1.183738	1.195629	0.963	0.995
0.005	1.191838	1.191042	1.205669	1.147	1.213
0.002	1.210363	1.206282	1.229385	1.547	1.879
0.001	1.224751	1.214200	1.244326	1.573	2.421

Note: The "Procedure" values were generated using 40 intervals.

for the K_I values. The cracks extend from -1 to $-k$ and from k to 1 . So the K values have the following expressions:

$$K_I(1)/K_{Io} = 1 + \frac{1}{(1-\Lambda)\pi(1-k)} \left[2E(m) - k(k+1)K(m) - \frac{\pi}{2}(1-k) \right] \quad (55)$$

$$K_I(k)/K_{Io} = 1 + \frac{1}{(1-\Lambda)\pi(1-k)} \left[-2E(m) + (k+1)K(m) - \frac{\pi}{2}(1-k) \right] \quad (56)$$

where $K_{Io} = \sigma\sqrt{\pi(1-k)/2}$ is the stress intensity factor for an isolated crack,
 $\Lambda = \sqrt{2(1+k)/(1+\sqrt{k})} - 1$ is the transmission factor,
 $m = \sqrt{1-k^2}$ is the argument of the elliptic integrals,
and K and E are complete elliptic integrals of the first and second kind.

These expressions for K_I were evaluated for a range of k values and the results are listed in Table C-I.

Analytical Solution

Page 46 of Sneddon and Lowengrub⁴ gives formulas for K_I and K_{II} values for a pair of adjacent horizontal cracks under either normal (σ) or shear (τ) stress applied remotely. The cracks extend from $x = -b$ to $-k$ and from k to b . The expressions for the K values at the near ends are

$$K_I(k) = \sigma(\pi/k)^{1/2} \frac{b^2 E(k)/K(k) - k^2}{(b^2 - k^2)^{1/2}} \quad (57)$$

$$K_{II}(k) = \tau(\pi/k)^{1/2} \frac{b^2 E(k)/K(k) - k^2}{(b^2 - k^2)^{1/2}} \quad (58)$$

and the K values at the remote ends are

$$K_I(b) = \sigma(\pi b)^{1/2} \frac{1 - E(k)/K(k)}{k} \quad (59)$$

$$K_{II}(b) = \tau(\pi b)^{1/2} \frac{1 - E(k)/K(k)}{k} \quad (60)$$

In these expressions, $K(m)$ and $E(m)$ are complete elliptic integrals of the first and second kind, and m is the modulus:

$$m = \sqrt{1 - k^2/b^2} \quad (61)$$

For comparisons with the other computations, it is useful to display these stress intensity factors as ratios of the present values divided by the K values for isolated cracks. These isolated K values are

$$K_{Io} = \sigma \sqrt{\pi(b - k)/2} \quad (62)$$

and a similar one for K_{IIo} .

These expressions for K_I were evaluated at several k values and the results are listed in Table C-I.

5. STANDARD STRESS FIELDS

Kachanov³ has provided the standard stress fields (in an elastic body) resulting from uniform tractions applied along the face of a crack. For these equations, the crack lies along the X-axis, with its center at the origin of coordinates. The uniform tractions are p and τ . The stresses at any point in the X-Y plane are:

$$\begin{aligned} \sigma_{xx} &= p(I_2 - 8Y^2 I_4 + 8Y^4 I_6) \\ \sigma_{yy} &= p(I_2 + 4Y^2 I_4 - 8Y^4 I_6) \end{aligned} \quad (63)$$

$$\sigma_{zy} = 2p(-YI_3 + XYI_4 + 4Y^3I_5 - 4XY^3I_6)$$

Similarly, for the shearing stress:

$$\begin{aligned}\sigma_{zz} &= 2\tau(3YI_3 - 3XYI_4 - 4Y^3I_5 + 4XY^3I_6) \\ \sigma_{yy} &= 2\tau(-YI_3 + XYI_4 + 4Y^3I_5 - 4XY^3I_6) \\ \sigma_{zy} &= \tau(I_2 - 8Y^2I_4 + 8Y^4I_6)\end{aligned}\tag{64}$$

The I factors in these equations are defined in terms of the locations of the point of interest and the crack length as follows:

$$\begin{aligned}I_1 &= 4L^3 \frac{\sqrt{\gamma} - \sqrt{\alpha}}{\sqrt{\delta}(\sqrt{\alpha} + \sqrt{\gamma} + \sqrt{\delta})^2} \\ I_2 &= 4L^2 \frac{1}{\sqrt{\delta}(\sqrt{\alpha} + \sqrt{\gamma} + \sqrt{\delta})} \\ I_3 &= 2L^3 \frac{\sqrt{\gamma} - \sqrt{\alpha}}{\sqrt{\alpha\gamma}\delta^{3/2}} \\ I_4 &= 2L^3 \frac{\sqrt{\alpha} + \sqrt{\gamma}}{\sqrt{\alpha\gamma}\delta^{3/2}} \\ I_5 &= \frac{L^3}{2} \frac{3\sqrt{\alpha\gamma}(\sqrt{\alpha} + \sqrt{\gamma})^2(\sqrt{\gamma} - \sqrt{\alpha}) + \delta(\gamma^{3/2} - \alpha^{3/2})}{(\alpha\gamma)^{3/2}\delta^{5/2}} \\ I_6 &= \frac{L^2}{2} \frac{(\alpha^{3/2} + \gamma^{3/2})\delta + 3\sqrt{\alpha\gamma}(\sqrt{\alpha} + \sqrt{\gamma})^3}{(\alpha\gamma)^{3/2}\delta^{5/2}}\end{aligned}\tag{65}$$

The Greek letters are defined for these equations as follows:

$$\begin{aligned}\alpha &= (X - L)^2 + Y^2 \\ \beta &= 2(X^2 + Y^2 - L^2) \\ \gamma &= (X + L)^2 + Y^2 \\ \delta &= \beta + 2\sqrt{\alpha\gamma}\end{aligned}\tag{66}$$

These are the standard stress fields used earlier in this appendix.

6. LISTING OF THE KCRACK COMPUTER PROGRAM

The KCRACK program consists of a main program plus several subroutines. The following listing starts with KCRACK. Next is the COMMON, a listing of the shared variables for use in the main program and all the subroutines except MINV, SIMQ, and TRACTN. Following the COMMON are the subroutines: CRALF, CRCOMP, CRFORC, CRK1, CRK2, CRNINT, CRSRAP, CRSTIF, CRSTRS, MINV, SIMQ, and TRACTN. The purpose for each subroutine is described briefly in the subroutine listing.

```

PROGRAM KCRACK
C   VERSION OF JANUARY 1988
C   CHANGED TO HAVE MANY SUBROUTINES.
C PROGRAM TO COMPUTE ELASTIC CRACK INTERACTION, WRITTEN BY
C   LYNN SEAMAN, SRI, JULY 1987 BASED ON DERIVATIONS
C   FROM MARK KACHANOV, TUFTS.
C X AND Y ARE COORDINATES OF CENTROID OF CRACK,
C THCR IS THE CCW ANGLE TO THE CRACK NORMAL IN DEGREES.
C STRESSES ARE POSITIVE IN TENSION.
C
C   INCLUDE '$DISK3:[SEAMAN.CRACK]KCKCOM.FOR'
C
C   CHARACTER*10 A1,A2,A3,A4,TITLE(8)
C   DIMENSION JBUG(10)
C   1- KCRACK      3- CRCOMP      5- CRK1      7- CRNINT      9- CRSTIF
C   2- CRALF       4- CRFORC      6- CRK2      8- CRSHAP     10- CRSTRS
C   VALUES OF JBUG(5) AND JBUG(10) OVER 2 GIVE PRINTS FROM -TRACTN-
C-----
C INPUT
C-----
C INPUT ELASTIC PROPERTIES
C   EMOD IS YOUNG'S MODULUS, POISSON IS POISSON'S RATIO
C   ANINT IS THE NUMBER OF INTEGRATION INTERVALS USED.
C   PI = 3.14159265358979323846
C   WRITE (6,1000)
1000 FORMAT (30X,'S R I   K C R A C K'/'          CRACK STRESS INTENSITY ',
1 'FACTORS, CRACK SHAPES, AND EFFECTIVE STIFFNESSES'/)
C   READ (5,1006) TITLE
C   WRITE (6,1006) TITLE
1006 FORMAT (8A10)
C   READ (5,1001) A1,EMOD,A2,POISSON,A3,ANINT,A4,JBUG
C   WRITE (6,1002) A1,EMOD,A2,POISSON,A3,ANINT,A4,JBUG
C   IBUG = JBUG(1)
C   NINTRV = 2*INT(0.5*ANINT + 0.5)
C   IF (NINTRV .GT. 100) NINTRV = 100
C   IF (NINTRV .LT. 2) NINTRV = 2
C   WRITE (6,1010) NINTRV
1010 FORMAT (' *** KCRACK 10, POSSIBLE RESETTNG: NINTRV = ',I5)
1001 FORMAT (3(A10,E10.3),A10,10I1)
1002 FORMAT (3(A10,1PE10.3),A10,10I1)
C INPUT EXTERNAL STRESS FIELD
C   READ (5,1003) A1,NTYPE,A2,SXX,A3,SYY,A4,SXY
C   WRITE (6,1004) A1,NTYPE,A2,SXX,A3,SYY,A4,SXY
1003 FORMAT (A10,I10,3(A10,E10.3))
1004 FORMAT (A10,I10,3(A10,1PE10.3))
C INPUT MICROCRACK LENGTHS, POSITIONS, AND ORIENTATIONS
C   NCRACK IS THE NUMBER OF CRACKS
C   READ (5,1003) A1,NCRACK,A2,SAREA
C   WRITE (6,1003) A1,NCRACK,A2,SAREA
C   DO 100 NC=1,NCRACK
C   XCR AND YCR ARE CENTROID OF CRACK, THCR IS ANGLE TO NORMAL
C   READ (5,1005) A1,ELCRACK(NC),A2,XCR(NC),A3,YCR(NC),A4,THCR(NC)
C   WRITE (6,1007) A1,ELCRACK(NC),A2,XCR(NC),A3,YCR(NC),A4,THCR(NC)
1005 FORMAT (4(A10,E10.3))
1007 FORMAT (4(A10,1PE10.3))
C-----
C INITIALIZATION OF XCRACK AND THETA
C-----
C   THETA(NC) = PI/180.*THCR(NC)

```

```

SINTH(NC) = SIN(THETA(NC))
COSTH(NC) = COS(THETA(NC))
EL SIN = ELCRAK(NC)*SINTH(NC)
EL COS = ELCRAK(NC)*COSTH(NC)
XCRACK(NC,1) = XCR(NC) - EL SIN
XCRACK(NC,2) = XCR(NC)
XCRACK(NC,3) = XCR(NC) + EL SIN
YCRACK(NC,1) = YCR(NC) + EL COS
YCRACK(NC,2) = YCR(NC)
YCRACK(NC,3) = YCR(NC) - EL COS
IF (IBUG.GT. 0) WRITE (6,1098) (XCRACK(NC,I),I=1,3),XCR(NC),
1 (YCRACK(NC,I),I=1,3),YCR(NC)
1098 FORMAT (' KCRACK 98 X=',1P3E15.8,' XCR=',E15.8/10X,' Y=',3E15.8,
1 ' YCR=',E15.8)
100 CONTINUE
C *** COMPUTE THE STRESSES DUE TO THE EXTERNAL LOADING
CALL CRFORC(JBUG(4))
C-----
C PART 1: COMPUTATION OF THE AVERAGE STRESSES ON EACH MICROCRACK
C-----
CALL CRSTRS(JBUG(10))
C-----
C PART 2: DETERMINATION OF THE -K- STRESS INTENSITY FACTORS
C-----
C *** DETERMINE THE TRACTIONS ON THE CRACK FACES
CALL CRK1(JBUG(5))
C *** COMPUTE THE K VALUES
DO 700 NC = 1,NCRACK
CALL CRK2(NC,JBUG(6))
C-----
C PART 3: COMPUTATION OF THE CRACK SHAPES
C-----
CALL CRSHAP(NC,JBUG(8))
700 CONTINUE
C-----
C PART 4: COMPUTATION OF THE COMPLIANCE AND STIFFNESS MATRICES
C-----
C *** ALPHA MATRIX FOR THE ORTHOTROPIC DIRECTIONS FOR NON-INTERACTING
CRACKS.
CALL CRALF(JBUG(2),SINALF,COSALF)
C *** CONSTRUCT SUM (NT + TN)L^2 FOR S11, S22, OR S12
CALL CRSTIF(JBUG(9),SINALF,COSALF)
C *** CONSTRUCT THE COMPLIANCE MATRIX
CALL CRCOMP(JBUG(3))
C *** CONSTRUCT THE STIFFNESS MATRIX FOR INTERACTING CRACKS
CALL MINV(AMAT,6,DETERM,LLL,MMM)
WRITE (6,1908) (AMAT(I),I=1,36)
1908 FORMAT (' STIFFNESS MATRIX = ',1P6E12.5,' FROM KCRACK 908'
1 /20X,6E12.5/20X,6E12.5/20X,6E12.5/20X,6E12.5/20X,6E12.5)
C-----
C PART 5: COMPUTE COMPLIANCE MATRIX FOR NON-INTERACTING CRACKS
C-----
CALL CRNINT(JBUG(7),SINALF,COSALF)
C *** CONSTRUCT THE STIFFNESS MATRIX FOR NON-INTERACTING CRACKS
CALL MINV(AMAT,6,DETERM,LLL,MMM)
WRITE (6,1928) (AMAT(I),I=1,36)
1928 FORMAT (' STIFFNESS MATRIX = ',1P6E12.5,' FROM KCRACK 928'
1 /20X,6E12.5/20X,6E12.5/20X,6E12.5/20X,6E12.5/20X,6E12.5)
STOP ' NORMAL END OF KCRACK'
END

```

```

      IMPLICIT REAL*8 (A-H,O-Z)
C      COMMONS FOR THE -KCRACK- CODE
COMMON KROW, NCRACK, NINTRV, SXX, SYY, SXY, EMOD, POISSON, SAREA
COMMON AK1 (10,2), AK2 (10,2)
COMMON ELCRAK (10), XCR (10), YCR (10), XCRACK (10,3), YCRACK (10,3)
COMMON COSTH (10), SINTH (10), THCR (10), THETA (10)
COMMON SP (10,101), ST (10,101), SUMN (101), SUMT (101), XID (101)
COMMON SNN (10,10,101), STN (10,10,101), SNT (10,10,101),
1  STT (10,10,101)
COMMON ALPHA (2,2)
COMMON AMAT (400), BMAT (400), FORCE (20), PL (20), TL (20,20)
COMMON SUM (3,3), COMPL (6,6), COMPL0 (6,6)
COMMON SHAPES (10,2), SHAPEA (10,2), SHAPEB (10,2)
COMMON LLL (6), MMM (6), PI

```

```

SUBROUTINE CRALF (IBUG,SINALF,COSALF)
C      COMPUTATION OF THE ALPHA MATRIX TO DETERMINE THE ORTHOTROPIC
C      DIRECTIONS FOR NON-INTERACTING CRACKS.
C
INCLUDE ' $DISK3:[SEAMAN.CRACK]KCKCOM.FOR'
C
CRSUM = 0.
DO 750 NC=1,NCRACK
EL2 = ELCRAK(NC)**2
CRSUM = CRSUM+EL2
ALPHA(1,1) = ALPHA(1,1) + EL2*SINTH(NC)**2
ALPHA(1,2) = ALPHA(1,2) + EL2*SINTH(NC)*COSTH(NC)
ALPHA(2,2) = ALPHA(2,2) + EL2*COSTH(NC)**2
750 CONTINUE
ALPHA(2,1) = ALPHA(1,2)
IF (IBUG .GT. 0) WRITE (6,1754) ALPHA(1,1),ALPHA(1,2),ALPHA(2,1),
1 ALPHA(2,2)
1754 FORMAT (/ ' ALF-754 ALPHA =',1P2E12.5/12X,2E12.5)
DALPHA = ALPHA(1,1)-ALPHA(2,2)
IF (ABS(DALPHA) .LT. CRSUM*1.E-30) DALPHA = CRSUM*1.E-30
TAN2ALF = -2.*ALPHA(1,2)/DALPHA
ALF = 0.5*ATAN(TAN2ALF)
ALFDEG = 0.5*ATAN(TAN2ALF)*180/PI
C      COS2ALF = 0.5*(ALPHA(1,1)-ALPHA(2,2))/SQRT(ALPHA(1,2)**2+
C      1 0.25*(ALPHA(2,2)-ALPHA(1,1))**2)
SINALF = SIN(ALF)
COSALF = COS(ALF)
C      -ALF- IS THE ANGLE OF THE ORTHOTROPIC AXES FROM X,Y, (+ CCW)
IF (IBUG .GT. 0) WRITE (6,1759) ALFDEG,TAN2ALF,SINALF,COSALF
1759 FORMAT (/ ' ALF-759 ALF(DEG)=' ,1PE12.5, ' TAN2ALF=' ,E12.5,
1 ' SINALF,COSALF=' ,2E12.5)
END

```

```

SUBROUTINE CRAMAT(AMAT,COMPL,POISSON)
  C   CONSTRUCT THE 6 X 6 COMPLIANCE MATRIX
  C
  C   DIMENSION AMAT(400),COMPL(6,6)
  C
  DO 908 I=1,36
908  AMAT(I) = 0.
      AMAT(1) = COMPL(1,1)
      AMAT(2) = COMPL(1,2)
      AMAT(3) = -POISSON
      AMAT(4) = 2.*COMPL(1,3)
      AMAT(7) = COMPL(2,1)
      AMAT(8) = COMPL(2,2)
      AMAT(9) = -POISSON
      AMAT(10) = 2.*COMPL(2,3)
      AMAT(13) = -POISSON
      AMAT(14) = -POISSON
      AMAT(15) = 1.
      AMAT(19) = COMPL(3,1)
      AMAT(20) = COMPL(3,2)
      AMAT(22) = 2.*COMPL(3,3)
      AMAT(29) = 2.*(1.+POISSON)
      AMAT(36) = 2.*(1.+POISSON)
      WRITE (6,1909) (AMAT(I),I=1,36)
1909  FORMAT (' COMPLIANCE MATRIX =',1P6E12.5/20X,6E12.5/20X,6E12.5/
1    20X,6E12.5/20X,6E12.5/20X,6E12.5)
      END

```

```

      SUBROUTINE CRCOMP (IBUG)
C      CONSTRUCT THE COMPLIANCE MATRIX
C      1,1 = 1111; 1,2 = 1122; 1,3 = 1112; . . . 3,3 = 1212
C
      INCLUDE '$DISK3:[SEAMAN.CRACK]KCKCOM.FOR'
C
      DO 908 I=1,36
1908 AMAT(I) = 0.
      AMAT(1) = 1.+PI/SAREA*SUM(1,1)
      AMAT(2) = -POISSON+PI/SAREA*SUM(1,2)
      AMAT(3) = -POISSON
      AMAT(4) = PI/SAREA*SUM(1,3)
      AMAT(7) = -POISSON+PI/SAREA*SUM(2,1)
      AMAT(8) = 1.+PI/SAREA*SUM(2,2)
      AMAT(9) = -POISSON
      AMAT(10) = PI/SAREA*SUM(2,3)
      AMAT(13) = -POISSON
      AMAT(14) = -POISSON
      AMAT(15) = 1.
      AMAT(19) = PI/SAREA*SUM(3,1)
      AMAT(20) = PI/SAREA*SUM(3,2)
      AMAT(22) = 2.*(1.+POISSON)+PI/SAREA*SUM(3,3)
      AMAT(29) = 2.*(1.+POISSON)
      AMAT(36) = 2.*(1.+POISSON)
      WRITE (6,1908)
1908 FORMAT (' ***** COMPLIANCE AND STIFFNESS MATRICES FOR',
1 ' INTERACTING CRACKS, ACCORDING TO KACHANOVs METHOD *****')
      WRITE (6,1909) (AMAT(I),I=1,36)
1909 FORMAT (' COMPLIANCE MATRIX =',1P6E12.5,' FROM CRCOMP 909'
1 /20X,6E12.5/20X,6E12.5/20X,6E12.5/20X,6E12.5/20X,6E12.5)
      END

```

```

      SUBROUTINE CRFORC(IBUG)
C  COMPUTE THE STRESSES DUE TO THE EXTERNAL LOADING
C
      INCLUDE '$DISK3:[SEAMAN.CRACK]KCKCOM.FOR'
C
C  FILL THE FORCE ARRAY WITH STRESSES ON EACH CRACK
C  FORCE( +1) IS THE NORMAL COMPONENT, FORCE( +2) THE SHEAR COMP.
      DO 200 NC = 1, NCRACK
        FORCE(2*NC-2+1) = SXX*COSTH(NC)**2 + 2.*SXY*COSTH(NC)*SINTH(NC) +
1      SYY*SINTH(NC)**2
        FORCE(2*NC-2+2) = -(SXX-SYY)*SINTH(NC)*COSTH(NC) +
1      SXY*(COSTH(NC)**2-SINTH(NC)**2)
200  CONTINUE
      KROW = 2*NCRACK
      IF (IBUG .EQ. 0) GO TO 210
      WRITE (6,1504) SXX,SYY,SXY
      WRITE (6,1507) (FORCE(I),I=1,KROW)
1504  FORMAT (' FORC-205 FORCE VECTOR: NORMAL AND SHEAR STRESS ACTING ',
1      'ON EACH CRACK FOR INPUT SXX, SYY, SXY=',1P3E10.3/10X,5X,
2      'NORMAL',10X,'SHEAR')
1507  FORMAT (10X,1P2E15.7)
210  CONTINUE
      END

```

```

SUBROUTINE CRK1 (IBUG)
C DETERMINATION OF TRACTIONS ON THE CRACK FACES IN PREPARATION FOR
C   COMPUTING THE K1C VALUES.
C
C   INCLUDE '$DISK3:[SEAMAN.CRACK]KCKCOM.FOR'
C
C CONSTRUCT THE ARRAYS (SP AND ST) OF STRESSES AT POINTS ALONG
C THE NC CRACK.
DO 600 NC = 1, NCRACK
  II = 2*(NC-1)
  DXEL = (XCRACK(NC,3)-XCRACK(NC,1))/2.
  DYEL = (YCRACK(NC,3)-YCRACK(NC,1))/2.
  DO 520 N = 1, NINTRV
    SUMN(N) = 0.
    SUMT(N) = 0.
520 CONTINUE
  DO 580 J = 1, NCRACK
    JJ = 2*(J-1)
    IF (NC .EQ. J) GO TO 580
    SINA = SINTH(NC)*COSTH(J)-SINTH(J)*COSTH(NC)
    COSA = COSTH(NC)*COSTH(J)+SINTH(NC)*SINTH(J)
    SINA2 = SINA**2
    COSA2 = COSA**2
    SINCOSA = SINA*COSA
    IF (IBUG .GT. 2) WRITE (6,1510) NC,J,SINA,COSA
1510 FORMAT (' K1-510 NC=',I4,' J=',I4,' SINA,COSA=',1P2E12.5)
    DO 570 N = 1, NINTRV
      XI = COS((2*(NINTRV+1-N)-1)*PI/(2.*NINTRV))
      XID(N) = XI
      XL = XCR(NC) + XI*DXEL
      YL = YCR(NC) + XI*DYEL
C
C   CALL -TRACTN- TO DETERMINE THE TRACTIONS ON THE CRACK FACES
CALL TRACTN (LS,NC,J,XL,YL,XCR(J),YCR(J),SINTH,COSTH,ELCRACK(J),
1 SXXN,SYYN, SXYN, SXXT, SYYT, SXYT, IBUG)
C
  IF (IBUG .GT. 2) WRITE (6,1568) NC,J,N,SXXN,SYYN,SXYN,SXXT,SYYT,
1 SXYT
1568 FORMAT (' K1-568 NC,J,N=',3I4,' SXXN,Y,XY=',1P3E12.5,
1 ' SXXT,Y,XY=',3E12.5)
  SNN(NC,J,N) = SXXN*COSA2 + SYYN*SINA2 + 2.*SXYN*SINCOSA
  STN(NC,J,N) = -(SXXN-SYYN)*SINCOSA + SXYN*(COSA2-SINA2)
  SNT(NC,J,N) = SXXT*COSA2 + SYYT*SINA2 + 2.*SXYT*SINCOSA
  STT(NC,J,N) = -(SXXT-SYYT)*SINCOSA + SXYT*(COSA2-SINA2)
  IF (IBUG .GT. 2) WRITE (6,1540) SNN(NC,J,N),STN(NC,J,N),
1 SNT(NC,J,N),STT(NC,J,N)
1540 FORMAT (' K1-540 SNN,STN=',1P2E12.5,' SNT,STT=',2E12.5)
  SUMN(N) = SUMN(N) + SNN(NC,J,N)*PL(2*J-1) + SNT(NC,J,N)*PL(2*J)
  SUMT(N) = SUMT(N) + STN(NC,J,N)*PL(2*J-1) + STT(NC,J,N)*PL(2*J)
570 CONTINUE
580 CONTINUE
DO 585 N = 1, NINTRV
  SP(NC,N) = FORCE(2*NC-1) + SUMN(N)
  ST(NC,N) = FORCE(2*NC) + SUMT(N)
585 CONTINUE
590 CONTINUE
600 CONTINUE
END

```

```

SUBROUTINE CRK2 (NC, IBUG)
C      COMPUTE THE CRACK TIP STRESS INTENSITY FACTORS
C
C      INCLUDE '$DISK3:[SEAMAN.CRACK]KCKCOM.FOR'
C
      WRITE (6,1605) NC
1605  FORMAT (' *****',40X,' *****' /
1      ' CRACK TIP STRESS INTENSITIES AND CRACK SHAPES FOR ',
2      ' CRACK NO.',I2,' WRITTEN BY CRK2' /)
      AK1 (NC,1) = 0.
      AK1 (NC,2) = 0.
      AK2 (NC,1) = 0.
      AK2 (NC,2) = 0.
      DO 660 N = 1,NINTRV
      AK1 (NC,1) = AK1 (NC,1) + (1.+XID (N)) * SP (NC,N)
      AK1 (NC,2) = AK1 (NC,2) + (1.-XID (N)) * SP (NC,N)
      AK2 (NC,1) = AK2 (NC,1) + (1.+XID (N)) * ST (NC,N)
      AK2 (NC,2) = AK2 (NC,2) + (1.-XID (N)) * ST (NC,N)
      IF (IBUG .GE. 2) WRITE (6,1567) NC,N,AK1 (NC,1),AK1 (NC,2),
1      AK2 (NC,1),AK2 (NC,2),XID (N),SP (NC,N),ST (NC,N)
1567  FORMAT (' K2-567 NC,N=',2I4,' K1=',1P2E10.3,' K2=',2E10.3,
1      '/ XID=',E10.3,' SP,ST=',2E10.3)
      660 CONTINUE
      SQPIL = SQRT (PI*ELCRAK (NC))
      AK1 (NC,1) = AK1 (NC,1) / NINTRV * SQPIL
      AK1 (NC,2) = AK1 (NC,2) / NINTRV * SQPIL
      AK2 (NC,1) = AK2 (NC,1) / NINTRV * SQPIL
      AK2 (NC,2) = AK2 (NC,2) / NINTRV * SQPIL
      PAVG = SXX * COSTH (NC) ** 2 + SYY * SINTH (NC) ** 2
1      + 2. * SXY * SINTH (NC) * COSTH (NC)
      AK10 = SQPIL * PAVG
      WRITE (6,1702) AK1 (NC,1),AK1 (NC,2),AK10,AK2 (NC,1),AK2 (NC,2)
1702  FORMAT (' K FACTORS',3X,' RIGHT TIP',3X,' LEFT TIP',4X,' ISOLATED',
1      ' WRITTEN BY CRK2' /
2      ' K1 =',1P3E12.5 /
3      ' K2 =',2E12.5)
      IF (ABS (AK10) .LT. 1.E-10) RETURN
      AK11 = AK1 (NC,1) / AK10
      AK12 = AK1 (NC,2) / AK10
      WRITE (6,1704) AK11,AK12
1704  FORMAT (' K1/K10',3H'S=',1P2E12.5)
      END

```

```

SUBROUTINE CRNINT (IBUG,SINALF,COSALF)
  COMPUTE COMPLIANCE MATRIX FOR NON-INTERACTING CRACKS

  INCLUDE '$DISK3:[SEAMAN.CRACK]KCKCOM.FOR'

  SUM(1,1) = 0.
  SUM(2,1) = 0.
  SUM(3,1) = 0.
  DO 10 NC = 1,NCRACK
    SUM(1,1) = SUM(1,1)+ELCRAK(NC)**2*(COSTH(NC)*COSALF +
1  SINTH(NC)*SINALF)**2
    SUM(2,1) = SUM(2,1)+ELCRAK(NC)**2*(SINTH(NC)*COSALF -
1  COSTH(NC)*SINALF)**2
    SUM(3,1) = SUM(3,1)+ELCRAK(NC)**2
10 CONTINUE
  DO 50 I=1,36
50 AMAT(I) = 0.
    AMAT(1) = 1.+PI/SAREA*SUM(1,1)
    AMAT(2) = -POISSON
    AMAT(3) = -POISSON
    AMAT(4) = 0.
    AMAT(7) = -POISSON
    AMAT(8) = 1.+PI/SAREA*SUM(2,1)
    AMAT(9) = -POISSON
    AMAT(10) = 0.
    AMAT(13) = -POISSON
    AMAT(14) = -POISSON
    AMAT(15) = 1.
    AMAT(19) = 0.
    AMAT(20) = 0.
    AMAT(22) = 2.*(1.+POISSON)+PI/SAREA*SUM(3,1)
    AMAT(29) = 2.*(1.+POISSON)
    AMAT(36) = 2.*(1.+POISSON)
    WRITE (6,1908)
1908 FORMAT (' ***** COMPLIANCE AND STIFFNESS MATRICES FOR NONINTERA',
1  'CTING CRACKS *****')
    WRITE (6,1909) (AMAT(I),I=1,36)
1909 FORMAT (' COMPLIANCE MATRIX =',1P6E12.5,' FROM CRNINT 909'
1  '/20X,6E12.5/20X,6E12.5/20X,6E12.5/20X,6E12.5/20X,6E12.5)
  END

```

```

SUBROUTINE CRSHP (NC, IBUG)
C      COMPUTATION OF THE CRACK SHAPES
C
      INCLUDE ' $DISK3:[SEAMAN.CRACK]KCKCOM.FOR'
C
      COMPUTATION OF THE ELLIPTIC SHAPE COEFFICIENTS
      SQPIL = SQRT(PI*ELCRAK(NC))
      SHAPEA(NC,1) = 0.
      SHAPEB(NC,1) = 0.
      SHAPEA(NC,2) = 0.
      SHAPEB(NC,2) = 0.
      SHAPES(NC,1) = 2.*PL(2*NC-1) - 0.5*(AK1(NC,1)+AK1(NC,2))/SQPIL
      IF (ABS(AK1(NC,1)+AK1(NC,2)) .LT. 1.) GO TO 665
      SHAPEA(NC,1) = (AK1(NC,1) - AK1(NC,2))/(4.*PL(2*NC-1)*SQPIL
1      - AK1(NC,1) - AK1(NC,2))
      SHAPEB(NC,1) = 2.*(AK1(NC,1) + AK1(NC,2) - 2.*PL(2*NC-1)*SQPIL)/
1      (4.*PL(2*NC-1)*SQPIL - AK1(NC,1) - AK1(NC,2))
665 SHAPES(NC,2) = 2.*PL(2*NC) - 0.5*(AK2(NC,1)+AK2(NC,2))/SQPIL
      IF (ABS(AK2(NC,1)+AK2(NC,2)) .LT. 1.) GO TO 670
      SHAPEA(NC,2) = (AK2(NC,1) - AK2(NC,2))/(4.*PL(2*NC)*SQPIL
1      - AK2(NC,1) - AK2(NC,2))
      SHAPEB(NC,2) = 2.*(AK2(NC,1) + AK2(NC,2) - 2.*PL(2*NC)*SQPIL)/
1      (4.*PL(2*NC)*SQPIL - AK2(NC,1) - AK2(NC,2))
C-----
C NORMAL AND SHEAR OPENING AREA
C-----
670 CONTINUE
      WRITE (6,1670) (SHAPES(NC,I), SHAPEA(NC,I), SHAPEB(NC,I), I=1,2)
1670 FORMAT (' SHAP 670 SHAPE FUNCTIONS IN THE FORM 4L/E*S(1+Ax+Bx2',
1      ' )Ellipse'/' FACTORS FOR OPENING ARE S, A, B =',1P3E11.3/
2      ' FACTORS FOR SHEARING ARE S, A, B =',3E11.3)
C      ***** RETURN IN CASE PRINTING IS NOT REQUESTED. *****
      IF (IBUG .LE. 0) RETURN
      AREA = 2.*PI*ELCRAK(NC)*SHAPES(NC,1)/EMOD*(1.+0.25*SHAPEB(NC,1))
      AREAT = 2.*PI*ELCRAK(NC)*SHAPES(NC,2)/EMOD*(1.+0.25*SHAPEB(NC,2))
C DISPLACEMENTS OF CRACKS
      DXX = 0.5*(AREA*COSTH(NC)**2 + AREAT*SINTH(NC)*COSTH(NC))
      DYY = 0.5*(AREA*SINTH(NC)**2 - AREAT*SINTH(NC)*COSTH(NC))
      DXY = 0.5*AREA*SINTH(NC)*COSTH(NC) - 0.25*AREAT*(COSTH(NC)**2
1      -SINTH(NC)**2)
      WRITE (6,1677) NC, AREA, AREAT, DXX, DYY, DXY
1677 FORMAT (' SHAP 677 OPENINGS FOR CRACK ',I3,' AREA,AREAT=',
1      1P2E11.3,' DXX, DYY, DXY=',3E11.3)
C-----
C COMPUTATION OF CRACK SHAPES
C-----
      NPLOT = 20
      OPISO = 4.*ELCRAK(NC)/EMOD*PAVG
      VSHEAR = 0.
      XOL = -1.
      VNORM = 0.
      WRITE (6,1688) NC
1688 FORMAT (' SHAP 688 CRACK SHAPE FOR CRACK NO ',I3/4X,'N',8X,'X/L',
1      9X,'BN',9X,'BT',6X,'BNISO',5X,'VSHEAR',6X,'VNORM',4X,'ELLIPSE')
      N = 1
      BNISO = 0.
      WRITE (7,1703) N,XOL,VSHEAR,VNORM,BNISO
      WRITE (6,1703) N,XOL,VSHEAR,VNORM,BNISO,VSHEAR,
1      VNORM,BNISO

```

```

DO 680 N = 2,NPLOT
RATIO = FLOAT(N-1)/FLOAT(NPLOT)
XOL = COS((1.-RATIO)*PI)
ELLIP = SQRT(1.-XOL**2)
VNORM = (1.+ SHAPEA(NC,1)*XOL + SHAPEB(NC,1)*XOL**2)*ELLIP
VSHEAR = (1.+ SHAPEA(NC,2)*XOL + SHAPEB(NC,2)*XOL**2)*ELLIP
BN = 4.*ELCRAK(NC)/EMOD*SHAPES(NC,1)*VNORM
BT = 4.*ELCRAK(NC)/EMOD*SHAPES(NC,2)*VSHEAR
BNISO = OPISO*ELLIP
WRITE (6,1703) N,XOL,BN,BT,BNISO,VSHEAR,VNORM,
1 ELLIP
1703 FORMAT (I5,1P10E11.3)
WRITE (7,1703) N,XOL,VSHEAR,VNORM,ELLIP
680 CONTINUE
N = NPLOT+1
XOL = 1.
VSHEAR = 0.
VNORM = 0.
WRITE (6,1703) N,XOL,VSHEAR,VNORM,VNORM,VSHEAR,
1 VNORM,VNORM
WRITE (7,1703) N,XOL,VSHEAR,VNORM,VNORM
WRITE (6,1684)
1684 FORMAT (' DEFINITIONS: BN and BT are normal (+ in opening) and
1 shear (+ CCW) displacement for the cracks (cm), (FROM SHAP 684)'
2 /14X,'BNISO is the normal opening for ',
3 'an isolated crack (cm)'/14X,'VNORM and VSHEAR are normalized',
4 ' opening and shearing distortion'/14X,'ELLIPSE is the '
5 'normalized elliptic distortion')
END

```

```

      SUBROUTINE CRSTIF (IBUG,SINALF,COSALF)
C      Computation of SUM Lk^2 (NkTk + TkNk) for each unit stress loading.
C
      INCLUDE '$DISK3:[SEAMAN.CRACK]KCKCOM.FOR'
C
      Construct STRESS TENSORS in X-Y plane corresponding to Unit
      Stresses S11, S22, and S12 in the orthotropic axes.
C      CCW Rotation of the STRESS back to X-Y axes by an angle -ALF.
      DO 900 ILOAD = 1,3
      IF (ILOAD .GT. 1) GO TO 800
C      TENSOR FOR THE S11 LOADING
      SXX = COSALF**2
      SYY = SINALF**2
      SXY = SINALF*COSALF
      GO TO 820
800 IF (ILOAD .GT. 2) GO TO 810
C      TENSOR FOR THE S22 LOADING
      SXX = SINALF**2
      SYY = COSALF**2
      SXY = -SINALF*COSALF
      GO TO 820
C      TENSOR FOR THE S12 LOADING
810 CONTINUE
      SXX = -2.*SINALF*COSALF
      SYY = 2.*SINALF*COSALF
      SXY = COSALF**2-SINALF**2
820 CONTINUE
C-----
C      FILL THE FORCE ARRAY WITH STRESSES ON EACH CRACK
C      FORCE( +1) IS THE NORMAL COMPONENT, FORCE( +2) THE SHEAR COMP.
C-----
      CALL CRFORC (IBUG)
C
      DO 840 I = 1,KROW
840 PL(I) = FORCE(I)
      KEND = 4*NCRACK**2
      DO 845 K = 1,KEND
845 BMAT(K) = AMAT(K)
C-----
C      COMPUTE THE STRESSES ON EACH MICROCRACK, ACCOUNTING FOR BOTH THE
C      APPLIED LOAD AND ALL OTHER CRACKS. -FORCE- IS APPLIED, -PL- IS
C      THE STRESS (NORMAL, SHEAR) ON EACH CRACK.
C-----
      CALL SIMQ(BMAT,PL,2*NCRACK,KSTOP)
      IF (IBUG .GT. 0) THEN
        WRITE (6,1841) ILOAD, SXX, SYY, SXY
1841 FORMAT (/' STIF 841 ILOAD =',I3,' SXX,SYY,SXY=',1P3E15.8)
        WRITE (6,1845) (FORCE(I),I=1,KROW)
1845 FORMAT ( ' STIF 845 FORCE (N, TAU) = ',1P7E15.8)
        WRITE (6,1843) (PL(I),I=1,KROW)
1843 FORMAT ( ' STIF 843 P (N, TAU) = ',1P7E15.8)
        WRITE (6,1848)
1848 FORMAT ( ' (STIF) AMAT MATRIX' )
        DO 850 I = 1,KROW
          KK = (I-1)*KROW
          WRITE (6,1850) (AMAT(KK+L),L=1,KROW)
850 CONTINUE
1850 FORMAT (1P7E15.8/(5X,7E15.8))
      ENDIF

```

```

C      T1 IS STRESS IN THE 1 DIRECTION, T2 IN THE 2 DIRECTION
C      IN THE ORTHOTROPIC COORDINATES
      SUM(1,ILOAD) = 0.
      SUM(2,ILOAD) = 0.
      SUM(3,ILOAD) = 0.
      DO 860 NC = 1, NCRACK
      COSTHA = COSTH(NC)*COSALF + SINTH(NC)*SINALF
      SINTHA = SINTH(NC)*COSALF - COSTH(NC)*SINALF
      T1 = PL(2*NC-2+1)*COSTHA - PL(2*NC-2+2)*SINTHA
      T2 = PL(2*NC-2+1)*SINTHA + PL(2*NC-2+2)*COSTHA
      EL2 = ELCRAK(NC)**2
      IF (IBUG .GT. 0) WRITE (6,1852) NC, T1,T2
1852 FORMAT (' STIF 852 CRACK NO',I2,' STRESSES IN 1 AND 2 DIRECTIONS,'
1      ' T1 AND T2 =',1P2E12.5)
C-----
C      SUM THE STRESS QUANTITIES FOR ALL CRACKS TO CONSTRUCT THE
C      SUM L^2 (NkTk + TkNk) terms
C-----
      DSUM1 = EL2*T1*COSTHA
      SUM(1,ILOAD) = SUM(1,ILOAD) + DSUM1
      DSUM2 = EL2*T2*SINTHA
      SUM(2,ILOAD) = SUM(2,ILOAD) + DSUM2
      DSUM3 = EL2*(T2*COSTHA + T1*SINTHA)
      SUM(3,ILOAD) = SUM(3,ILOAD) + DSUM3
      IF (IBUG .GT. 1) WRITE (6,1858) ILOAD,DSUM1,DSUM2,DSUM3,
1      (SUM(I,ILOAD),I=1,3)
1858 FORMAT (' STIF 858 ILOAD=',I3,' DSUMs =',1P3E12.5,' SUM=',
1      1P3E12.5)
      860 CONTINUE
      900 CONTINUE
      END

```

```

SUBROUTINE CRSTRS (IBUG)
C      COMPUTATION OF THE STRESSES ON EACH MICROCRACK
C
C      INCLUDE '$DISK3:[SEAMAN.CRACK]KCKCOM.FOR'
C
C-----
C BEGIN LOOP TO COMPUTE THE L(I,J) MATRIX
C-----
C I IS THE INDICATOR FOR THE MICROCRACK OF INTEREST
C J IS ANOTHER MICROCRACK
      NCR2 = 2*NCRACK
      ANINTR3 = 3*NINTRV
      DO 500 NC = 1,NCRACK
        IN = 2*NC-1
        IT = 2*NC
        DX = (XCRACK(NC,3)-XCRACK(NC,1))/NINTRV
        DY = (YCRACK(NC,3)-YCRACK(NC,1))/NINTRV
        DO 450 J = 1,NCRACK
          JN = 2*J-1
          JT = 2*J
          IF (NC.NE.J) GO TO 220
          AMAT((JN-1)*NCR2+IN) = 1.
          AMAT((JT-1)*NCR2+IN) = 0.
          AMAT((JN-1)*NCR2+IT) = 0.
          AMAT((JT-1)*NCR2+IT) = 1.
          GO TO 450
220 CONTINUE
          SINA = SINTH(NC)*COSTH(J)-SINTH(J)*COSTH(NC)
          COSA = COSTH(NC)*COSTH(J)+SINTH(NC)*SINTH(J)
          SINA2 = SINA**2
          COSA2 = COSA**2
          SINCOSA = SINA*COSA
          SUMXXN = 0.
          SUMYYN = 0.
          SUMXXY = 0.
          SUMXXT = 0.
          SUMYYT = 0.
          SUMXYT = 0.
          NINTRV1 = NINTRV+1
          DO 300 N = 1,NINTRV1
            XL = XCRACK(NC,1)+(N-1)*DX
            YL = YCRACK(NC,1)+(N-1)*DY
C
C      CALL -TRACTN- TO DETERMINE THE TRACTIONS ON THE CRACK FACES
C      CALL TRACTN (LS,NC,J,XL,YL,XCR(J),YCR(J),SINTH,COSTH,ELCRACK(J),
1      SXXN,SYYN,SXYN,SXXT,SYYT,SXYT,IBUG)
C
      IF (IBUG.GT.2) WRITE (6,1297) NC,J,N,SXXN,SYYN,SXYN,SXXT,SYYT,
1      SXYT
1297 FORMAT (' STRS 297 NC,J,N=',3I4,' SXXN,Y,XY=',1P3E12.5,
1      ' SXXT,Y,XY=',3E12.5)
      COEF = 1.
      IF (N.GT.1.AND.N.LT.NINTRV1) COEF = 2.+2.*MOD(N-1,2)
      SUMXXN = SUMXXN + COEF*SXXN
      SUMYYN = SUMYYN + COEF*SYYN
      SUMXYN = SUMXYN + COEF*SXYN
      SUMXXT = SUMXXT + COEF*SXXT
      SUMYYT = SUMYYT + COEF*SYYT
      SUMXYT = SUMXYT + COEF*SXYT

```

```

300 CONTINUE
C CONSTRUCT THE STRESSES ON THE NC CRACK IN THE ORIENTATION OF THE
C NC CRACK: STRNN AND STRNT - NORMAL STRESS ON NC FROM NORMAL AND
C SHEAR ON J, AND STRTN AND STRTT - SHEAR ON NC FROM NORMAL AND
C SHEAR ON J.
STRNN = (SUMXXN*COSA2 + SUMYYN*SINA2 + 2.*SUMXYN*SINCOSA)/ANINTR3
STRTN = (-(SUMXXN-SUMYYN)*SINCOSA + SUMXYN*(COSA2-SINA2))/ANINTR3
STRNT = (SUMXXT*COSA2 + SUMYYT*SINA2 + 2.*SUMXYT*SINCOSA)/ANINTR3
STRTT = (-(SUMXXT-SUMYYT)*SINCOSA + SUMXYT*(COSA2-SINA2))/ANINTR3
C CONSTRUCT THE -A- MATRIX: A(EFFECT,CAUSE)
AMAT((JN-1)*NCR2+IN) = -STRNN
AMAT((JT-1)*NCR2+IN) = -STRTN
AMAT((JN-1)*NCR2+IT) = -STRNT
AMAT((JT-1)*NCR2+IT) = -STRTT
450 CONTINUE
500 CONTINUE
KROW = 2*NCRACK
KEND = 4*NCRACK**2
IF (IBUG .EQ. 0) GO TO 508
WRITE (6,1502)
DO 505 I = 1,KROW
KK = (I-1)*KROW
WRITE (6,1503) (AMAT(KK+L),L=1,KROW)
505 CONTINUE
WRITE (6,1500)
DO 506 I = 1,KROW
WRITE (6,1503) (TL(I,J),J=1,KROW)
506 CONTINUE
508 CONTINUE
DO 509 K = 1,KEND
509 BMAT(K) = AMAT(K)
1500 FORMAT (/ ' STRS 500, -TL- MATRIX' )
1502 FORMAT (/ ' STRS 502, -AMAT- MATRIX' )
1503 FORMAT (1P7E15.8/(5X,7E15.8))
C-----
C SOLUTION FOR STRESSES ON EACH MICROCRACK, CONSIDERING BOTH
C THE APPLIED STRESS FIELD AND ALL OTHER CRACKS
C PL(1) = NORMAL STRESS AND PL(2) = SHEAR STRESS
C-----
DO 510 I = 1,KROW
510 PL(I) = FORCE(I)
CALL SIMQ(BMAT,PL,2*NCRACK,KSTOP)
IF (IBUG .GT. 0) WRITE (6,1550) (PL(I),I=1,KROW)
1550 FORMAT ( ' STRS 550, AVERAGE FORCE ACTING ON EACH CRACK: ',
1 ' P (N, TAU)'/19X,'NORMAL',10X,'SHEAR'/(10X,1P2E15.8) )
END

```

```

SUBROUTINE MINV(A,N,D,L,M)
IMPLICIT REAL*8 (A-H,O-Z)
DIMENSION A(1),L(1),M(1)
C      SEARCH FOR LARGEST ELEMENT
D=1.
NK=-N
DO 80 K=1,N
NK=NK+N
L(K)=K
M(K)=K
KK=NK+K
BIGA=A(KK)
DO 20 J=K,N
IZ=N*(J-1)
DO 20 I=K,N
IJ=IZ+I
10  IF (ABS(BIGA)-ABS(A(IJ))) 15,20,20
15  BIGA=A(IJ)
L(K)=I
M(K)=J
20  CONTINUE
C      INTERCHANGE ROWS
J=L(K)
IF (J-K) 35,35,25
25  KI=K-N
DO 30 I=1,N
KI=KI+N
HOLD=-A(KI)
JI=KI-K+J
A(KI)=A(JI)
30  A(JI)=HOLD
C      INTERCHANGE COLUMNS
35  I=M(K)
IF (I-K) 45,45,38
38  JP=N*(I-1)
DO 40 J=1,N
JK=NK+J
JI=JP+J
HOLD=-A(JK)
A(JK)=A(JI)
40  A(JI)=HOLD
C      DIVIDE COLUMN BY MINUS PIVOT (VALUE OF PIVOT ELEMENT IS
C      CONTAINED IN BIGA)
45  IF (ABS(BIGA)-1.E-20) 46,46,48
46  D=0.
WRITE (6,446) BIGA
RETURN
48  DO 55 I=1,N
IF (I-K) 50,55,50
50  IK=NK+I
A(IK)=A(IK)/(-BIGA)
55  CONTINUE
C      REDUCE MATRIX
DO 65 I=1,N
IK=NK+I
HOLD=A(IK)
IJ=I-N
DO 65 J=1,N
IJ=IJ+N

```

```

        IF (I-K) 60,65,60
60      IF (J-K) 62,65,62
62      KJ=IJ-I+K
        A(IJ)=HOLD*A(KJ)+A(IJ)
65      CONTINUE
C        DIVIDE ROW BY PIVOT
        KJ=K-N
        DO 75 J=1,N
        KJ=KJ+N
        IF (J-K) 70,75,70
70      A(KJ)=A(KJ)/BIGA
75      CONTINUE
C        PRODUCT OF PIVOTS AND REPLACE PIVOT BY RECIPROCAL
        D=D*BIGA
        A(KK)=1./BIGA
80      CONTINUE
C        FINAL ROW AND COLUMN INTERCHANGE
        K=N
100     K=K-1
        IF (K) 150,150,105
105     I=L(K)
        IF (I-K) 120,120,108
108     JQ=N*(K-1)
        JR=N*(I-1)
        DO 110 J=1,N
        JK=JQ+J
        HOLD=A(JK)
        JI=JR+J
        A(JK)=-A(JI)
110     A(JI)=HOLD
120     J=M(K)
        IF (J-K) 100,100,125
125     KI=K-N
        DO 130 I=1,N
        KI=KI+N
        HOLD=A(KI)
        JI=KI-K+J
        A(KI)=-A(JI)
130     A(JI)=HOLD
        GO TO 100
150     RETURN
446    FORMAT(/' MINV - MATRIX IS SINGULAR, BIGA = ',1PE12.4/)
        END

```

```

SUBROUTINE SIMQ(A,B,N,KS)
IMPLICIT REAL*8 (A-H,O-Z)
DIMENSION A(1),B(1)
C      FORWARD SOLUTION
TOL=0.0
KS=0
JJ=-N
DO 65 J=1,N
JY=J+1
JJ=JJ+N+1
BIGA=0.
IT=JJ-J
DO 30 I=J,N
C      SEARCH FOR MAXIMUM COEFFICIENT IN COLUMN
IJ=IT+I
IF (ABS(BIGA)-ABS(A(IJ))) 20,30,30
20 BIGA=A(IJ)
IMAX=I
30 CONTINUE
C      TEST FOR PIVOT LESS THAN TOLERANCE (SINGULAR MATRIX)
IF (ABS(BIGA)-TOL) 35,35,40
35 KS=1
RETURN
C      INTERCHANGE ROWS IF NECESSARY
40 I1=J+N*(J-2)
IT=IMAX-J
DO 50 K=J,N
I1=I1+N
I2=I1+IT
SAVE=A(I1)
A(I1)=A(I2)
A(I2)=SAVE
C      DIVIDE EQUATION BY LEADING COEFFICIENT
50 A(I1)=A(I1)/BIGA
SAVE=B(IMAX)
B(IMAX)=B(J)
B(J)=SAVE/BIGA
C      ELIMINATE NEXT VARIABLE
IF (J-N) 55,70,55
55 IQS=N*(J-1)
DO 65 IX=JY,N
IXJ=IQS+IX
IT=J-IX
DO 60 JX=JY,N
IXJX=N*(JX-1)+IX
JJX=IXJX+IT
60 A(IXJX)=A(IXJX)-(A(IXJ)*A(JJX))
65 B(IX)=B(IX)-(B(J)*A(IXJ))
C      BACK SOLUTION
70 NY=N-1
IT=N*N
DO 80 J=1,NY
IA=IT-J
IB=N-J
IC=N
DO 80 K=1,J
B(IB)=B(IB)-A(IA)*B(IC)
IA=IA-N
80 IC=IC-1

```

RETURN
END

```

SUBROUTINE TRACTN (LS,NC,J,XL,YL,XCR,YCR,SINTH,COSTH,EL,
1  SXXN,SYYN,SXYN,SXXT,SYYT,SXYT,IBUG)
C      ROUTINE TO COMPUTE THE TRACTIONS ALONG THE LENGTH OF THE
C      -NC- CRACK IN RESPONSE TO THE STRESSES FROM THE -J- CRACKS.
C      CALLED BY KCRACK, WRITTEN BY L. SEAMAN ON JULY 29, 1987.
      IMPLICIT REAL*8 (A-H,O-Z)
      DIMENSION SINTH(10),COSTH(10)
      X = (XL-XCR)*SINTH(J)-(YL-YCR)*COSTH(J)
      Y = (XL-XCR)*COSTH(J)+(YL-YCR)*SINTH(J)
      AL = SQRT((X-EL)**2+Y**2)
      GL = SQRT((X+EL)**2+Y**2)
      DL = SQRT(2.*(X**2+Y**2-EL**2 +
1  SQRT((X**2+Y**2+EL**2)**2 - 4.*(X*EL)**2)))
      IF (IBUG.GT. 2) WRITE (6,1010) LS,NC,J,XL,YL,XCR,YCR,X,Y,
1  SINTH(J),COSTH(J),SINTH(NC),COSTH(NC), SINA, COSA, EL,
2  AL,DL,GL
1010 FORMAT (' TRACTN LS,NC,J=',3I3,' XL,YL=',1P2E12.5,' XCR,YCR=',
1  2E12.5,' X,Y=',2E12.5/' SINJ,COSJ=',2E10.3,' SINNC,COSNC=',
2  2E10.3,' SINA,COSA=',2E10.3,' EL=',E10.3/' AL,DL,GL=',3E10.3)
C COMPUTE Gi = Ii, FACTORS IN THE "STANDARD" STRESS FIELDS
      G1 = 4.*EL**3*(GL-AL)/(DL*(AL+GL+DL)**2)
      G2 = 4.*EL**2/(DL*(AL+GL+DL))
      G3 = 2.*EL**3*(GL-AL)/(AL*GL*DL**3)
      G4 = 2.*EL**2*(AL+GL)/(AL*GL*DL**3)
      G5 = 0.5*EL**3*(3.*AL*GL*(AL+GL)**2*(GL-AL)+DL**2*(GL**3-AL**3))/
1  ((AL*GL)**3*DL**5)
      G6 = 0.5*EL**2*((AL**3+GL**3)*DL**2 + 3.*AL*GL*(AL+GL)**3)/
1  ((AL*GL)**3*DL**5)
      IF (IBUG.GT. 2) WRITE (6,1020) G1,G2,G3,G4,G5,G6
1020 FORMAT (' TRACTN 20 G1,2,3=',1P3E12.5,' G4,5,6=',3E12.5)
C COMPUTE SXX, SY, SXY, THE STRESSES AT THE POINTS X,Y ON THE NC
C CRACK CAUSED BY CONSTANT NORMAL AND SHEARING STRESSES OF UNIT
C INTENSITY ON THE J CRACK. ORIENTATION IS WITH RESPECT TO THE
C J CRACK.
      SXXN = G2 - 8.*Y**2*G4 + 8.*Y**4*G6
      SYYN = G2 + 4.*Y**2*G4 - 8.*Y**4*G6
      SXYN = 2.*(-Y*G3 + X*Y*G4 + 4.*Y**3*G5 - 4.*X*Y**3*G6)
      SXXT = 2.*(3.*Y*G3 - 3.*X*Y*G4 - 4.*Y**3*G5 + 4.*X*Y**3*G6)
      SYYT = 2.*(-Y*G3 + X*Y*G4 + 4.*Y**3*G5 - 4.*X*Y**3*G6)
      SXYT = G2 - 8.*Y**2*G4 + 8.*Y**4*G6
      IF (IBUG.GT. 2) WRITE (6,1030) SXXN,SYYN,SXYN,SXXT,SYYT,SXYT
1030 FORMAT (' TRACTN 30 SXXN,Y,XY=',1P3E12.5,' SXXT,Y,XY=',3E12.5)
      RETURN
      END

```

REFERENCES

1. M. Kachanov, "A Simple Technique of Stress Analysis in Elastic Solids with Many Cracks," *Int. J. Fracture*, 28, R11-R19, 1985.
2. M. Kachanov, "Continuum Model of Medium with Cracks," *ASCE Eng. Mech. Div.*, 106, (5), p1039-1051, October 1980.
3. M. Kachanov, "Elastic Solids with Many Cracks: A Simple Method of Analysis," May 1984, (unpublished).
4. I. N. Sneddon and M. Lowengrub, Crack Problems in the Classical Theory of Elasticity, John Wiley & Sons, Inc., New York, 1969.

END

DATED

FILM

8-88
STIC